UNIVERSITY OF PISA

Engineering PhD School "Leonardo da Vinci"

PhD Course in
"Applied Electromagnetism in Electrical and Biomedical Engineering, Electronics, Smart Sensors, Nano-Technologies"

PhD Thesis

Near Field Coupling in Wireless Systems for Identification, Sensing and Communication

ING/INF-02

Advisors:

Prof. Paolo NEPA

_____

Prof. Giuliano MANARA

_____

Author:

Andrea MICHEL

_____

2015

2015

*Whatever you think you can do
or believe you can do,
begin it.
Action has magic, grace and power in it*
J.W. Goethe

2015

Contents

List of Figures

Publications

International Journals

1.   Caso, R.; D'Alessandro, A.; **Michel, A**.; Nepa, P.; "*Integration of Slot Antennas in Commercial Photovoltaic Panels for Stand-Alone Communication Systems,*" *IEEE Transactions on Antennas and Propagation,* , vol.61, no.1, pp. 62-69, January 2013.

2.   **Michel, A**.; Caso, R.; Buffi, A.; Nepa, P., and Isola G., "*Meandered TWAs array for Near-Field UHF RFID Applications*", *IET Electronic Letters*, 02 January 2014

3.   Caso, R.; **Michel, A**.; Nepa, P., and Pino, M. R.; , "*Dual-Band UHF-RFID/WLAN Circularly Polarized Antenna for Portable RFID Readers,*" *IEEE Trans. on Antennas and Propagation*, Vol. 62, n. 5, 2014

International Conferences

4.   Caso, R.; **Michel, A**.; Nepa, P.; Manara, G.; Massini, R.; , "*Design and performance of an integrated antenna for a 433MHz car park monitoring system,*" *Antennas and Propagation Society International Symposium (APSURSI), 2012 IEEE* , vol., no., pp.1-2, 8-14 July 2012

5.   **Michel, A**.; Caso, R.; Tavanti, L.; Gazzarrini, L.; Garroppo, R.; Nepa, P.; , "*Design and performance analysis of a slot antenna integrated in a photovoltaic panel*," *Antennas and Propagation Society International Symposium (APSURSI), 2012 IEEE* , pp.1-2, 8-14 July 2012

6.   **Michel, A**.; Caso, R.; Buffi, A.; Nepa, P.; Isola, G.; Chou, H. T.; "*Design and Performance Analysis of a Planar Antenna for Near-Field UHF-RFID Desktop Readers*" *Proceedings of Asia-Pacific Microwave Conference (APMC),* Kaohsiung, Taiwan, 4-7 December, 2012

7.   **Michel, A**.; Caso, R.; Buffi, A.; Nepa, P., and Isola, G; , "*An Array of Meander Travelling Wave Antennas for Near-Field UHF-RFID Readers*," Antennas and Propagation Society International Symposium (APSURSI), 2013 IEEE , 6-12 Jul 2013

8.   Buffi, A.; **Michel, A**.; Caso, R.; Nepa, P., "*Near-field coupling in UHF-RFID systems*," Electromagnetic Theory (EMTS), Proceedings of 2013 URSI International Symposium on , pp.408,411, 20-24 May 2013

9.   **Michel, A**.; Caso, R.; Buffi, A.; Nepa, P., and Isola, G; , " *Modular antenna for reactive and radiative near-field regions of UHF-RFID desktop readers*," XXXIth URSI General Assembly and Scientific Symposium (URSI GASS), 2014

10.   Caso, R.; **Michel, A**.; Nepa, P., and Pino, M. R.; , " *Performance comparison between an UHF RFID antenna for portable reader and its UHF RFID/WLAN dual-band version* ," XXXIth URSI General Assembly and Scientific Symposium (URSI GASS), 2014

11.   Caso, R.; **Michel, A**.; Buffi, A., and Nepa, P., " *A modular antenna for UHF RFID near-field desktop reader*," IEEE RFID Technology and Applications Conference (RFID-TA), Tampere, Finland, 11-13 September 2014

12.   Baroni, A..; **Michel, A**.; Pannozzo, M.; Zamberlan, D.; Andrenacci, M., and Silvestri,. F, " *Performance Assessment of the Smart mAritime saTellite terminal for mUltimedia seRvices and conteNts (SATURN) system* ", 7th Advanced Satellite

Multimedia System Conference – 13th Signal processing for Space Communications Workshop*, Livorno, Italy, September, 2014

National Conferences

13.   **Michel, A**.; Caso, R.; Buffi, A.; Nepa, P.; Isola, G.; "*Near-Field UHF RFID Antenna for Desktop Reader,*" *Proceedings of XIX RiNEm*, Roma, Italy, September, 2012

14.   Serra A. A.; Caso, R.; Buffi, A.; Guraliuc A.; D'Alessandro A.; **Michel, A**.; Nepa, P.; "*Research Activities on Antenna Design for Wireless Communication Networks at the University of Pisa,*" *Proceedings of XIX RiNEm*, Roma, Italy, September, 2012

15.   Caso, R.; Buffi, A.; and **Michel, A**., "*Near-field Modular Antenna For UHF RFID Desktop Reader Applications,*" *Proceedings of XX RiNEm*, Padova, Italy, September 2014

16.   Buffi, A.; **Michel, A**.; Caso, R.; D'Alessandro, A.; Baroni, A., and Nepa, P. "*Research Activities On UHF RFID Systems At The University Of Pisa - Research Unit,*" *Proceedings of XX RiNEm*, Padova, Italy, September 2014

Introduction

Antennas for radio communication systems (e.g. radio links, cellular networks, WLAN, remote sensing) are designed giving a lot of attention to antenna gain, polarization, radiation pattern characteristics (e.g. half power beam width, front to back ratio, etc.). All above parameters are defined in the antenna far-field (FF) region, so they are suitable to characterize a communication system in which the transmitter and the receiver antennas are far enough (i.e. distance bigger than $2D^2/\lambda$, where D is the maximum antenna size and λ is the free-space wavelength).

On the other hand, some applications exist that exploit antenna features in its near-field (NF) region (i.e. distance smaller than $2D^2/\lambda$). In this context, NF coupling between antennas has been studied since a long time and most researches have been focused on coupling effects in antenna arrays, field sensing for near-field antenna scanning systems, magnetic coupling between loops operating at LF-HF frequency bands.

Recently the near-field coupling analysis has been applied to specific short-range radio systems, as for example NFCs (Near Field Communications), microwave wireless power transfer, as well as RFID (Radio Frequency IDentification) systems. In low-frequency (LF, 125-134 KHz) and high-frequency (HF, 13.56 MHz) RFID systems the reader-tag communication occurs through a near-field inductive coupling, and antennas are usually made of single/multi turn coils (at both reader and tag side). The inductive coupling is robust with respect to environmental effects (metallic or liquid objects in the tag proximity). On the other hand, UHF (860-960 MHz) and microwave (2.4 GHz and 5.8 GHz) RFID systems are characterized by increased reading range, reading rate and data rate with respect to LF and HF RFID systems. Tag and reader are usually in the far-field region of each other and system performance can be evaluated by simple formulas derived from the free-space Friis equation. However, UHF and microwave RFID systems are sensitive to environmental effects such us line-of-sight obstruction, multipath propagation, presence of near objects exhibiting high dielectric permittivity and loss.To exploit the potentials of both HF and UHF RFID systems, the Near-Field (NF) UHF RFID systems have been investigated. They are expected to combine typical

advantages of UHF systems (high reading rate and data rate) with those of HF systems (robustness to the environment and multipath). Communication occurs in the antennas near-field zone, like in the HF systems, but through an electromagnetic coupling. In several UHF RFID applications the NF coupling between reader and tag antennas can occur: item-level tagging (ILT) in pharmaceutical and retailing industry, tracking of objects moving along conveyor belts, RFID printers/encoders, desktop readers, RFID portals of supply-chain or warehouse management.

In this context, the author designed and tested several antennas for Near-Field UHF-RFID Desktop Readers, and they are presented and analyzed in Chapter I and Chapter II. These antenna solutions are capable to generate a strong and uniform electromagnetic field in a confined volume, making the tag detection possible only up to few tens of centimeters (near-field region), even in presence of items with different material. Such activities have been developed in collaboration with the Yuan-Ze University of Taiwan and the C.A.E.N. RFID s.r.l. company.

Moreover, in the last decade the near-field coupling has been employed in many biomedical field, for example to monitor the breathing, heart rate, temperature or blood pressure. Wearable sensors have been also designed to sense the dielectric properties of the human internal tissues and then to estimate the patient health status (e.g. localize the presence of tumors). A specific sensor and an innovative dielectric permittivity estimation method have been proposed by the research group at the ElectroScience Laboratory, Ohio State University (Columbus, OH, USA), where the author spent six months as a Visiting Scholar. During this period, he developed numerical codes aimed at estimating the accuracy achievable with the novel estimating method. It is worth noting that the operating frequency of such a wearable system was 40MHz, so the theoretical analysis had to take into account the sensor performance in the near-field region. The main research results are presented in Chapter III.

The near-field coupling is also an important phenomenon to take into account when one or more antennas are integrated in the same communication system. In this case, the near-field coupling between antennas has to be limited to avoid interferences and overall performance degradation. For example, the author designed antennas for GSM/UMTS, WiFi and WiMAX applications systems to be integrated in a photovoltaic panel, exploiting the available room between solar cells. The presence of solar cells and glass close to the radiating elements has an important effect on the antenna performance, and a proper optimization is needed. More details on the design process is presented in Chapter IV, together with simulated and measured performance results.

Finally, the mutual coupling effect is significant in all those communication systems in which antennas for different wireless applications are integrated into a single compact device. In particular, the author designed antennas to be integrated in a compact handheld RFID reader. The two antennas were designed for two separate applications (i.e. UHF RFID and WiFi). Since the overall available volume in a handheld reader is small, the two radiating elements are very close to each other, and the mutual coupling effect can be significant. In Chapter V a detailed analysis of this problem is presented.

1 Near-field Antennas for UHF RFID desktop readers

1.1 Introduction

An accurate analysis of near-field (NF) coupling between antennas is essential to improve the performance of a number of short-range wireless applications, such as Near-Field Communication (NFC) [1], microwave wireless power transfer [2]-[3], as well as Radio Frequency Identification (RFID) [4]. Specifically, tag and reader antenna designs are strictly related to each other, in near-field passive RFID systems. There are two main near-field RFID classes, which correspond to different operating frequency bands: HF (13.56 MHz) and UHF (865-928 MHz). HF RFID systems are short-range communication systems based on inductive coupling between the reader antenna and the antenna of the data-provider device. The tag is powered up through the interrogation magnetic field, so that these systems are not susceptible to the presence of liquids or other dielectric and conductive objects in the tag proximity. Since the magnetic field amplitude decreases rapidly after a short distance, HF RFID systems can find application in Item Level Tagging (ILT) in pharmaceutical and retailing industries. On the other hand, UHF RFID systems are often preferred because they are able to transmit a larger amount of data in a shorter time, and small and low-cost tags can be used. Thus, for those applications where reader antenna and tags are in the near-field region of each other, NF UHF RFID systems have been developed; they have the above advantages typical of UHF RFID systems [5]-[7], and an improved robustness with respect to the effects of metals and liquids nearby the tag.

A number of solutions for NF UHF RFID reader antennas have been proposed, exploiting both the inductive and the capacitive coupling in the near-field region. Segmented loop antennas have been proposed to get an almost constant current distribution in a physically large loop, where contiguous loop segments are connected by lumped [8] or distributed [9]-[12] capacitive elements. However, getting a 50 Ω impedance matching in the whole UHF RFID band is quite awkward, due to both the

low radiation resistance and the high reactance typical of loop antennas, and a proper matching network is needed [8]-[10]. Array of patches [12]-[13] or slots [14] have also been designed for UHF and microwaves (e.g. 2.4 GHz) frequency bands. Above mentioned solutions consist of resonating antennas whose size is specified by the operating frequency, and consequently they are not easily scalable solutions that can fit predetermined detection areas with an arbitrary size. More recently, travelling wave antennas (TWAs) have been proposed for NF-UHF RFID systems [15]-[20]. Since their length and shape are not strictly related to the operating frequency (non-resonating structures), they are able to be changed in size quite easily. Then, a printed TWA can represent a low-cost, scalable, wideband, and low-profile solution, which allows for an undemanding shaping of the electromagnetic field in a confined volume nearby the antenna surface. Specifically, since the tag may be located at an arbitrary location over the antenna surface, with any orientation too, an as homogeneous as possible amplitude distribution for all filed components is required to avoid tag reading failures (low detection rate over the antenna surface). In this context, microstrip line technology has been often applied [15]-[19]. Parallel straight microstrip lines have been proposed for smart-shelf applications [15], while trying to improve the distribution of a specific *H*-field component parallel to the antenna surface. In [16]-[17], a single straight microstrip line has been presented for a NF UHF RFID reader (865-928 MHz), and a modified version with slight meanders has also been proposed for conveyor belt applications. Coupled meander microstrip lines and two spiral-shape parallel transmission lines have been presented in [18] and [19], respectively. A straight coplanar stripline (CPS) is proposed in [20]-[21], where the antenna is composed by several elements (a grounded CPW input line, a coplanar stripline, a lumped balun, multiple resistors and a finite-size ground plane). Such an antenna has been optimized to maximize the magnetic field component perpendicular to the antenna surface, in order to detect loop-like tags placed right on it.

In this Chapter, a new reader antenna suitable for NF-UHF RFID applications is proposed, with reference to a desktop reader application. In particular, a TWA realized with CPW technology has been designed [22]. With respect to microstrip technology, the CPW technology allows to generate field force-lines concentrated above the antenna surface rather than inside the dielectric substrate. In order to obtain a homogeneous field distribution above the antenna surface, a meander geometry has been adopted, also for making the reader performance more independent on tag orientation. Furthermore, an array of meandered TWAs has been also designed, getting a confined and uniform field distribution close to the antenna (up to few centimeters), where tagged items are supposed to lie on. In particular, the presence of 2×2 radiating elements allows maximizing both electric and magnetic fields within a confined volume above the reader antenna surface (10 cm), reducing the false positives issue in the item level tagging applications (e.g. smart point readers).

1.2 Antenna Design and Performance

An NF UHF-RFID reader antenna operating in the 865-928 MHz frequency band has been designed. Such an antenna has been thought to be able to confine the

electromagnetic field in the antenna near-field region with low far-field radiation, in order to detect tags at a range up to around 10 cm from the antenna surface, with no-coupling with other tags external to the detection volume (cross readings). A printed TWA has been adopted, since it also represents a low-cost, wideband, and scalable solution. After a preliminary qualitative comparison analysis, a CPW technology has been preferred to microstrip TWAs [15]-[19]. Indeed, in a microstrip line the field-force lines are such that the region with the strongest electromagnetic field intensity is concentrated inside the dielectric substrate, between the printed line and the ground plane (Fig. 1.1a). Conversely, using a CPW it is possible to increase field intensity outside the dielectric, because a strong electromagnetic field is generated into the two slots between the internal conductor and the lateral ground planes (Fig. 1.1b). Thus, the electromagnetic field above a CPW line is expected to be stronger than the field above a microstrip line, at the same operative feeding conditions, and this can improve the antenna performance in near-field applications.

(a) (b)
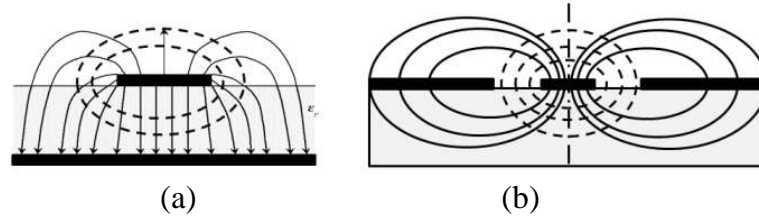
Fig. 1.1 - Electric field force-lines of (a) a microstrip line and (b) a CPW.

In a printed transmission line, the power concentration ratio is defined as the ratio between the power flowing through the dielectric laminate and that one travelling through the whole transmission line section. In [23], it is shown that such ratio is lower for CPWs with higher characteristic impedance (Z_0). Then, instead of using a conventional 50Ω CPW can be convenient using such a degree of freedom to increase field amplitude above the antenna surface. On the other hand, the CPW characteristic impedance is strictly related to the distance between the internal conductor and the ground planes. Specifically, for a given internal conductor width, the greater the slot width, the higher is Z_0. Then a CPW characteristic impedance higher than 50Ω also allows to fill with a strong field a larger physical area (Fig. 1.2b).

The antenna size has been set to 275×135 mm^2, in order to test it inside an existing RFID reader case. Nevertheless, the proposed layout is easily scalable to almost any arbitrary size, since TWAs length and shape are not strictly related to the operating frequency. In Fig. 1.2, the antenna layout is depicted and its main geometrical parameters are listed in Table I. The antenna is made of a meander CPW divided into a forward branch and a backward branch (it is named as *Snake Antenna* in the following). The meander layout has been adopted to get an electromagnetic field distribution as uniform as possible above the antenna surface. The CPW line has been realized on a 0.73mm-thick FR4 substrate and ends on a matched load, to avoid a standing wave (non-uniform) field pattern on the antenna surface. A metallic reflector has also been added (Fig. 1.2b) in order to make the reader performance quite independent from the material properties of the desk supporting the antenna. Antenna design has been performed by using the commercial tool CST Microwave Studio®.
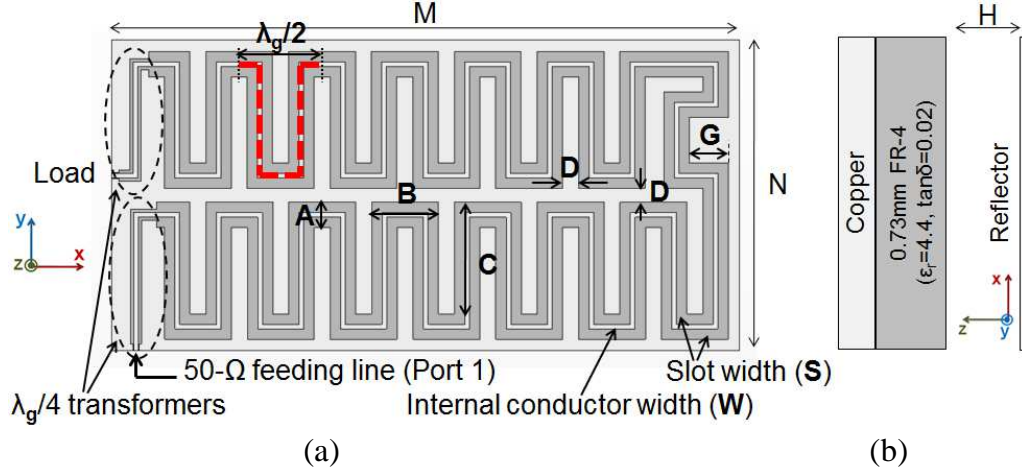
Fig. 1.2- Snake Antenna layout and its main geometrical parameters: (a) top view and (b) stackup.

TABLE I
ANTENNA SIZE (mm)

SNAKE ANTENNA									
A	*B*	*C*	*D*	*G*	*M*	*N*	*H*	*S*	*W*
11	29	49	7	17	275	135	10	4.6	2

In the *Snake Antenna* design, a 150Ω CPW line (*S*=4.6 mm, *W*=2 mm) has been chosen. This characteristic impedance value comes out from a trade-off between the electromagnetic field intensity required near the antenna surface and the maximum width allowed for the meander line (*A*) by the space constraints. A quarter-wavelength impedance transformer is needed to match the CPW line to the required 50 Ω input impedance (actually, two quarter-wavelength impedance transformers have been used, as during the measurement phase the matched load has been replaced by an SMA connector in order to measure the power absorbed by the matched load, namely to allow for S12 measurements). Moreover, a minimum distance between two adjacent meanders (*D*) was guaranteed in order to limit mutual coupling effects that complicate achieving a wideband impedance matching. It is worth noting that the need for a matched load is twofold: it allows to realize a TWA (with no stationary wave field distribution on the antenna surface) and also reduces the antenna efficiency (namely, it reduces far-field antenna gain, which is mandatory to avoid tag cross readings outside the reader detection volume). The simulated antenna gain is less than -13 dBi in the whole UHF RFID band.

The meanders number has been set in order to fully cover the tag detection area, keeping constant the distance (*D*) among them, along both the *x*-axis and the *y*-axis. The overall CPW line length results longer than 10 λ_g (λ_g being the CPW guided wavelength). The length of a couple of meanders corresponds to around one CPW guided wavelength (as apparent in Fig. 1.3 where simulated results for the surface current are shown for a particular phase value, at 900MHz).
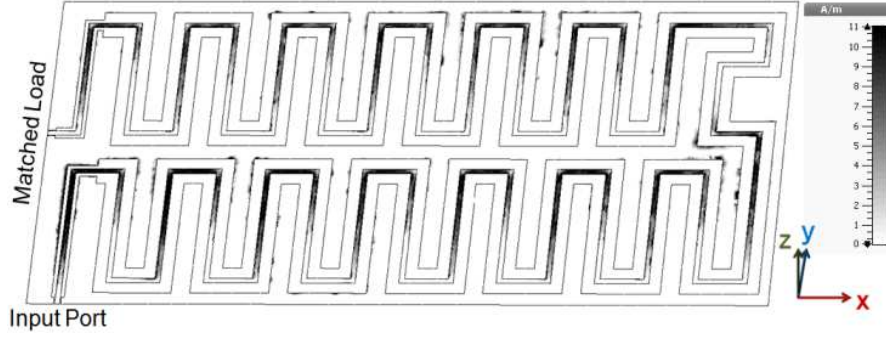
Fig. 1.3. - Simulated surface current intensity on the CPW line, at a particular phase value, at 900MHz.

Fig. 1.4. - Simulated surface current verse in the CPW internal conductor, at a particular phase value, at 900MHz. It should be noted that along the y-axis the currents verse in the forward and backward branch are in-phase, so improving the generated electromagnetic field above the antenna surface.

Above design criteria combined with a proper optimization of the parameter G (Fig. 1.2a), allowed us to obtain in-phase currents in the forward and backward branches of the antenna (Fig. 1.4), so avoiding deep minima in the field distribution on the antenna surface. It is also worth noting that the discontinuities introduced by the meanders also contribute to increase near-field radiation [23].

To limit the antenna thickness, in agreement with typical aesthetic specifications for desktop readers, the metallic reflector is placed at a distance of only 10 mm from the FR4 laminate (Fig. 1.2b). It has been verified that the presence of such a metallic reflector does not complicate impedance matching, even if it is very close to the CPW line (less than around $\lambda_0/30$, λ_0 being the free-space wavelength). Since the proposed antenna is a non-resonating structure, it is robust to the presence of the reflector plane as well as to the dielectric and mechanical tolerances, which are attractive features for a simple and cheap production process.

In the HF band, most of the tags are loop-like tags that require a magnetic coupling mechanism. On the other hand, in the NF UHF-RFID systems both electric and magnetic coupling are important, since both dipole-like and loop-like tags may be used. Since at UHF band it is expected that the homogeneity of the electric field also implies the homogeneity of the magnetic field, simulation results only for the magnetic field behavior are considered in the following. The simulated magnetic field normalized distributions on transverse planes are shown in Fig. 1.5.

17
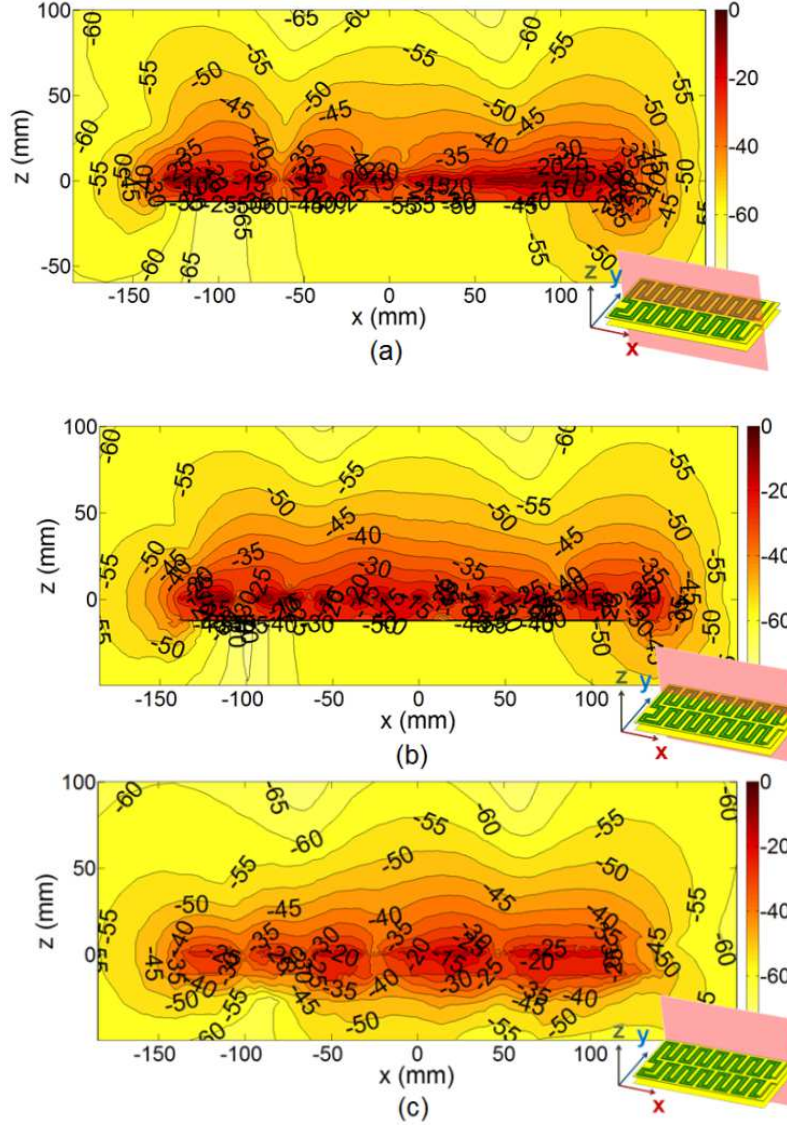
Fig. 1.5. - Simulated normalized H-field intensity (dB) on three planes perpendicular to the Snake Antenna surface and parallel to the xz-plane: (a) y=0, in the middle of the antenna, (b) y=34 mm, in the middle of the meander forward branch, and (c) y=68 mm, at the antenna border (all plots are normalized to the maximum value among them).

In particular, three different planes have been considered: y=0 mm (in the middle of the antenna), y=34 mm (in the middle of the meander forward branch) and y=68 mm (at the antenna border). It is apparent that the *H*-field is concentrated in the region above the antenna.

In order to evaluate the magnetic field homogeneity, each single *H*-field component has been calculated on a 275×135 mm^2 plane, at a distance of 1 cm from the reader antenna surface (Fig. 1.6), at 900MHz. All plots are normalized to the maximum of the *H*-field total amplitude. The H_z intensity, which is stronger close to the meanders, is the dominant magnetic field component, and this allows for reliable loop-like tag detection, when the tag is parallel to the reader antenna surface. Furthermore, thanks to meandered design, both H_x and H_y are excited. Since the meander segments along the *y*-axis are longer than those along the *x*-axis, the H_x intensity is stronger than the H_y intensity, on average.

(a)

(b)

(c)
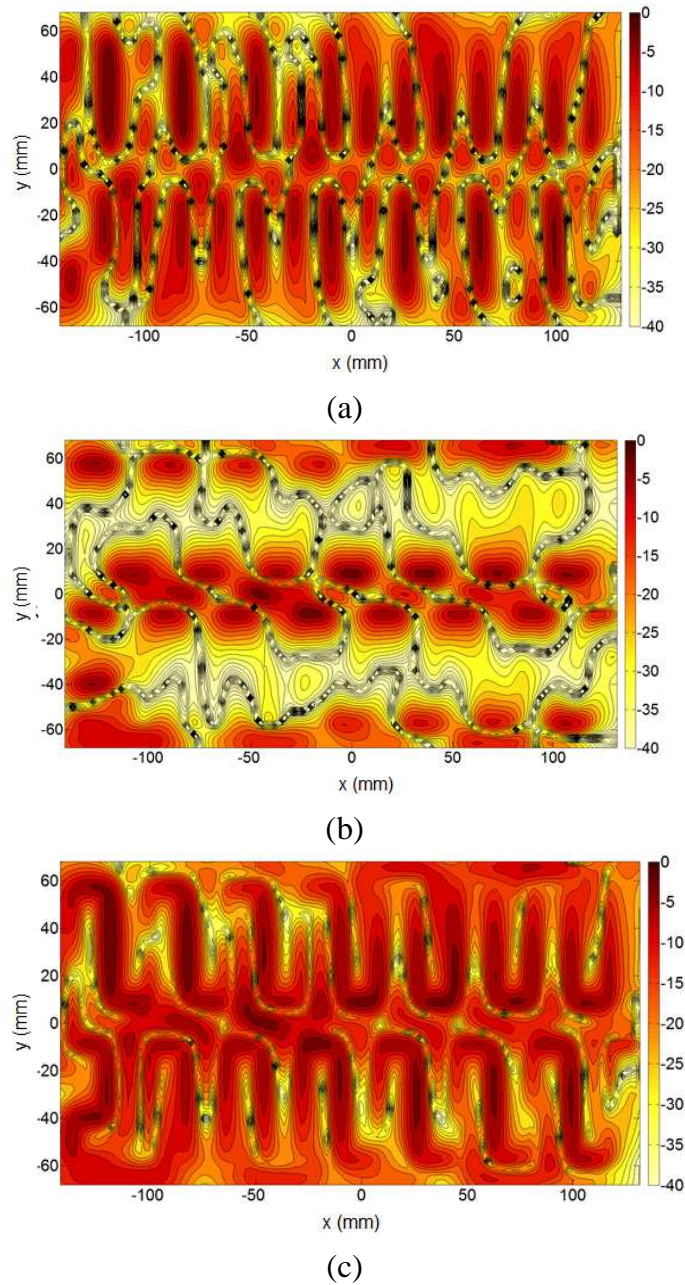
Fig. 1.6. - Simulated normalized H-field components (dB) on a xy-plane (275 × 135 mm2) at a distance of 1 cm from the Snake Antenna surface: (a) Hx, (b) Hy and (c) Hz. Magnetic field data have been obtained at 900MHz.

1.3   Measurements

A prototype of the proposed *Snake Antenna* has been realized (Fig. 1.7) and characterized. The meandered CPW line has been etched on a 0.73mm-thick FR4 substrate.
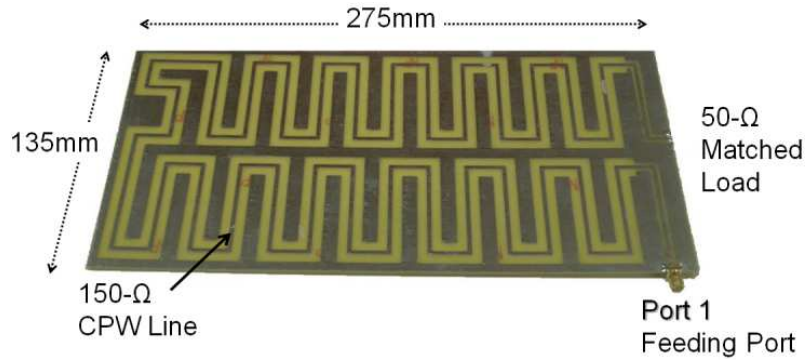
Fig. 1.7. - *Snake Antenna* prototype.

The *Snake Antenna* reflection coefficient has been measured and it is shown in Fig.1.8. In the European (865-868 MHz) and American (902-928 MHz) UHF RFID bands the reflection coefficient is lower than -15dB. Measurement results in the 700MHz-1GHz frequency band illustrate that the considered antenna typology (travelling wave antenna) allows for a quite good impedance matching, as expected. Wideband performance are only mainly limited by the presence of the quarter-wavelength impedance transformer, and the coupling effects between adjacent CPW lines (the latter can be controlled through the geometrical parameter *D*). The measured S12 parameter is around -6dB in the operating frequency band.
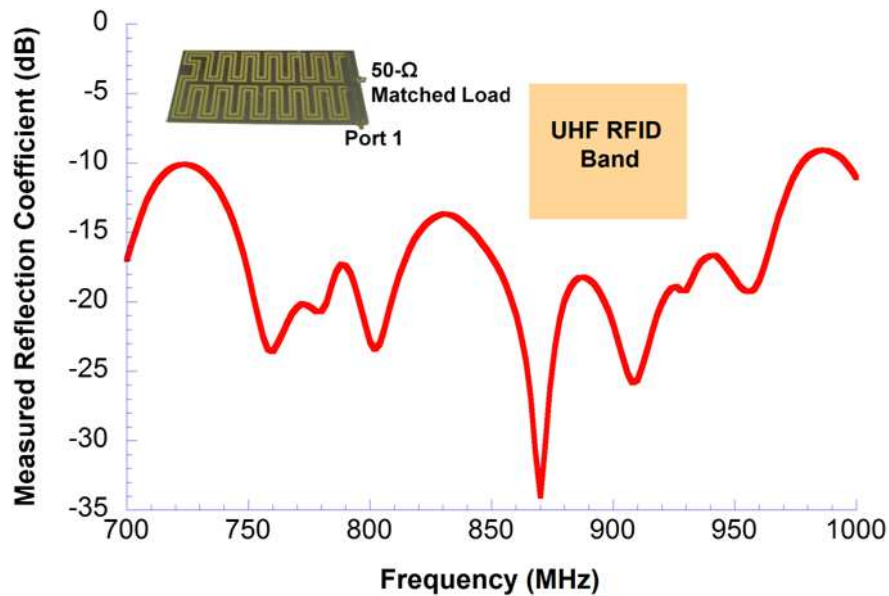
Fig.1.8. - Measured reflection coefficient of the Snake Antenna (CPW meander line ending on a soldered 50-Ω load), with a (275 × 135 mm2) reflector plane at a distance of 10 mm from the FR4 substrate.

The performance of the proposed *Snake Antenna* has been tested with a commercial compact UHF RFID reader (CAEN R1260I Slate) designed for slim desktop readers. Measurements of tag detection range have been carried out, by varying tag orientation, position and distance with respect to the antenna surface. The measurement setup is shown in Fig. 1.9. Two different tags have been used: the Inlay UH113, LAB ID (18×32 mm^2, oriented to near-field applications) [24], and the ALN 9640 Squiggle Inlay, Alien Technology (94.8×8.15 mm^2, optimized for far-field applications) [25].

The US RFID band (902-928 MHz) has been considered, and the reader output power has been set to 23 dBm. The antenna surface (275×135 mm^2) has been subdivided into 4×9 square cells (30×30 mm^2). The detection test has been repeated in each cell, for both tags, by varying the distance of the tag from the *Snake Antenna* surface. As an example, the results of the detection tests are shown in Fig. 1.10 and Fig. 1.11, for the short-range and the long-range tag, respectively, for two different tag orientations.
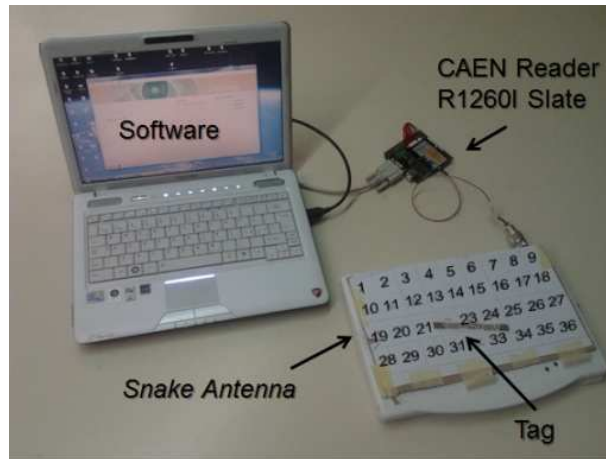
Fig. 1.9. - Measurement setup for the tag detection tests.

It results that the short-range tag can be detected beyond 12 cm for one specific orientation (Fig. 1.10). The long-range tag is gradually undetected above the antenna edge close to the feeding port, and it is undetected beyond a distance of 70 cm (Fig. 1.11).

(a)   (b)
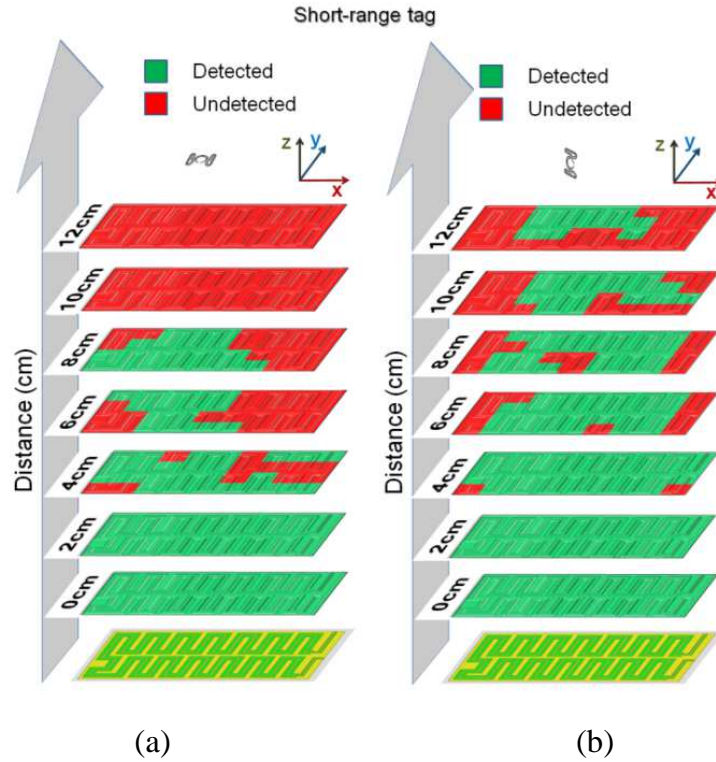
Fig. 1.10. - Detection tests by varying the distance of the tag from the antenna surface, when the short-range tag (Inlay UH113, Lab-ID) is aligned to the (a) x-axis and the (b) z-axis. Tests have been carried out by setting the reader input power equal to 23 dBm. The tag drawing scale is the same as for the reader antenna.

(a)   (b)
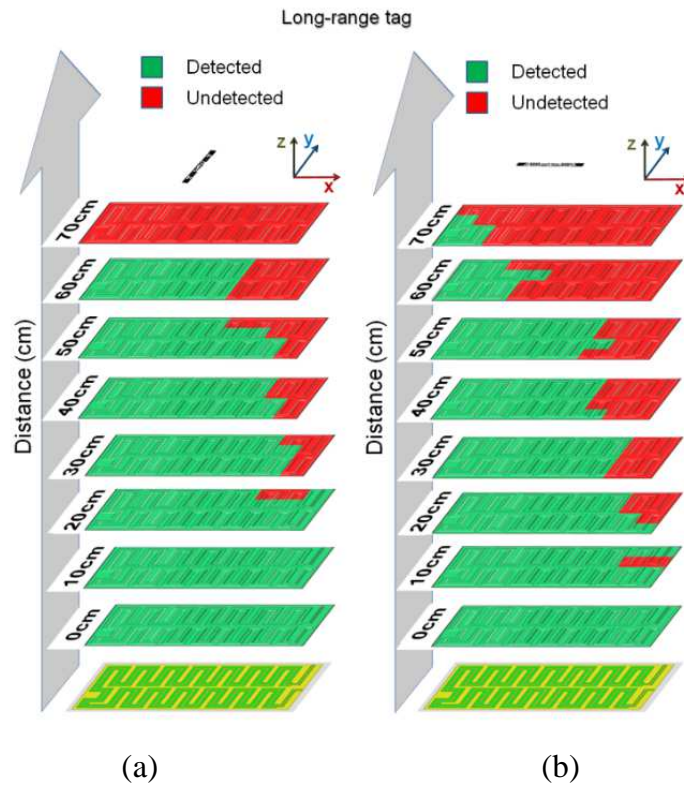
Fig. 1.11. - Detection tests by varying the distance of the tag from the antenna surface, when the long-range tag (ALN 9640 Squiggle Inlay, Alien Technology) is aligned to the (a) y-axis and the (b) x-axis. Tests have been carried out by setting the reader input power equal to 23 dBm. The tag drawing scale is the same as for the reader antenna.

By varying the distance from the antenna surface and the tag orientation, a large number of tests have been carried out to get an estimation of the percentage of the whole antenna surface where the tags can be successfully detected. Results are summarized in Fig. 1.12.
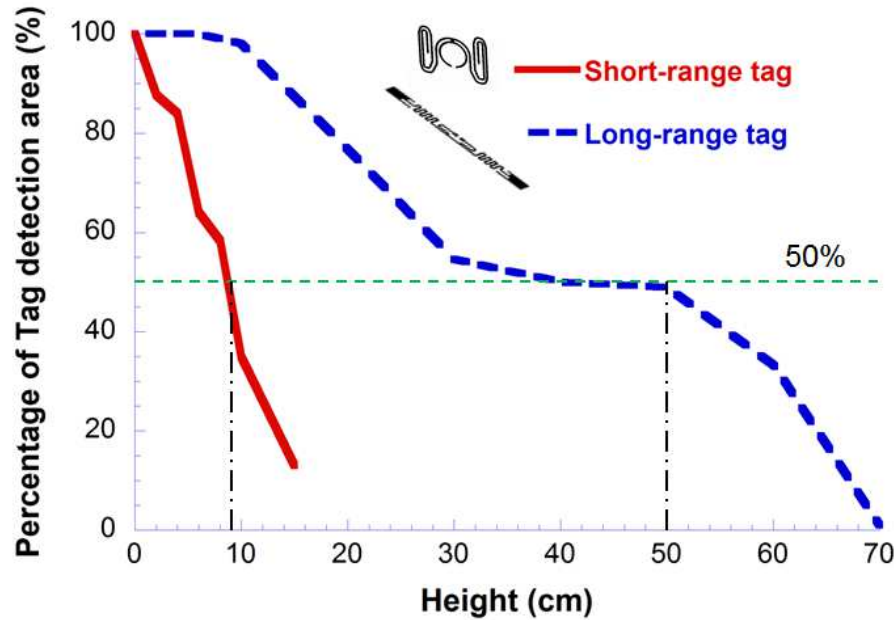
Fig. 1.12. - Percentage of the whole antenna area (275×135 mm2) where the tags can be successfully detected; repeated tests have been performed by varying tag position and orientation.

When fed with a reader output power of 23dBm, the proposed *Snake Antenna* is able to detect the short-range and the long-range tag up to 10 cm and 50 cm away from the antenna surface, respectively, in more than 50% of the whole antenna surface.

It is apparent that the quite large extension of the reading range for the ALN 9640 Squiggle Inlay is mainly due to its long-range feature; on the other hand, this reading range is expected to reduce in real scenarios where a number of tagged items are usually stacked up and all processed at once. Indeed, tag detection rate is affected by the material properties of the items the tags are attached to, as well as by tag mutual coupling. Thus, a further detection test has been carried out to validate the antenna performance in presence of a number of stacked tags. In particular, 16 long-range tags (Inlay UH414, LAB ID) [24] have been placed one above the other and separated through blocks of Styrofoam, with the same relative orientation with respect to the antenna borders (Fig. 1.13).
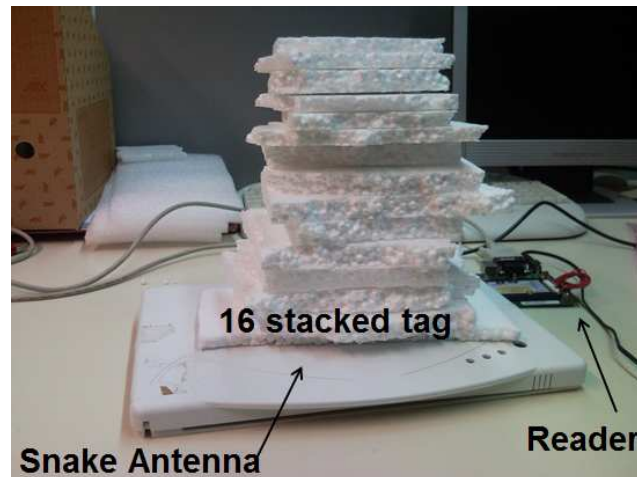
Fig. 1.13. - Measurement setup for the detection test of 16 stacked tags up to 20 cm. The reader input power has been set to 23 dBm (200 mW). The tags are separated through blocks of Styrofoam.

The first tag was placed directly on the antenna case. The second tag was placed at a distance of 10 mm from the first one. From the 2nd to the 11th tag, the spacing between each couple was equal to 15 mm, meanwhile from the 11th to the 16th the distance was equal to 10 mm, for an overall height of 20 cm. Such a non-uniform distance distribution between the tags has been chosen to increase the tests number beyond 10 cm, where the tag readability was supposed to be very low. The reader input power was set to 23 dBm. Two different stack orientations have been considered (Fig. 1.14).

Fig. 1.14. - Two considered orientations of the 16 stacked tags with respect to the antenna surface.

Moreover, the 16-tags stack has been continuously and randomly moved above the whole antenna surface, for both orientations, to obtain an average detection performance. Thus, the readings number for each tag has been recorded, by considering a reading time interval of 30 sec, and it is shown in Fig. 1.15, for both the European (865-868 MHz) and American (902-928 MHz) frequency bands. As expected, the read range is affected by the presence of multiple tags, and the considered long-range tag detection is substantially confined up to about 11 cm.
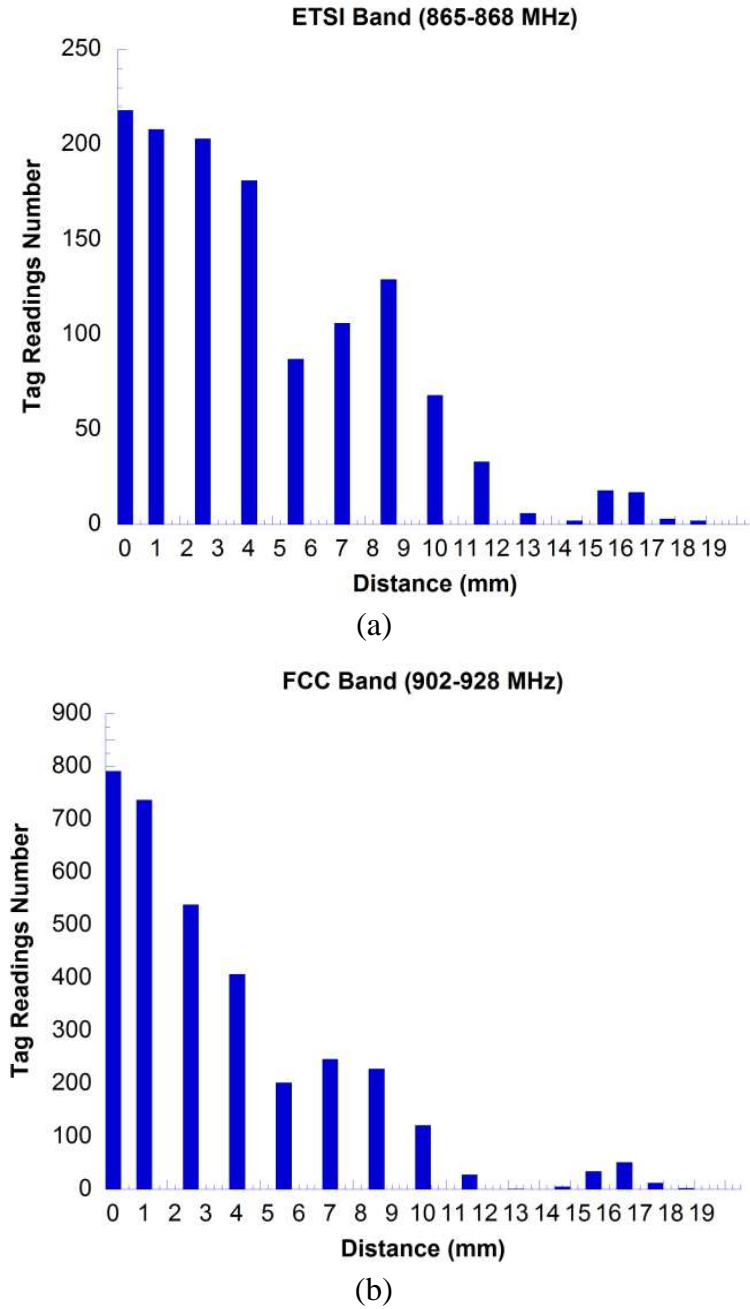
Fig. 1.15. - Detection tests for a stack of 16 tags (Inlay UH414, LAB ID) while the stack is continuously moved on the antenna surface, for a reading interval of 30sec. The test has been carried out by setting the reader input power equal to 23 dBm. The lower tag is right on the antenna cover (distance equal to 0mm), while the most far tag is at an height of around 19 mm from the antenna surface.

1.4   Meandered TWAs array

As an extension of the single line meandered line, an array has been designed and fabricated. Specifically, it is composed of 2×2 meandered CPW lines, printed on a 1.53 mm-thick FR-4 substrate (Fig. 1.16). Each of them ends on a matched load at the center of the antenna surface; thus, a travelling wave (not stationary) is excited. Since such loads introduce losses, a low far-field gain is reached (simulated maximum gain is about

-14 dB), so limiting far-field interferences and the problem of false positives readings. Moreover, when CPW technology is adopted, the higher the line characteristic impedance, the higher the field generated above the antenna, and the wider the CPW line. This suggests to use a relatively high characteristic impedance to maximize the antenna near-field. In the proposed antenna, the line characteristic impedance is equal to 130 Ω, whose width C represents a trade-off between the available space on the antenna surface and the TWA field intensity. Anyway, two λ/4 transformers have been properly introduced to match the input impedance (equal to 50 Ω). In order to compensate the 180°-rotation of the right branch with respect to the left one, the length difference of the two feeding lines reaching each branch has been set to $\lambda_g/4$ (with λ_g the guided wavelength within the substrate). Thus, an overall broadside far-field radiation has been obtained. As in [22], the meandered lines are such that the fields components along the three main directions are excited (*x*, *y*, and *z* in Fig. 1.16); in the proposed novel antenna solution some meanders are also oblique with respect to the antenna edges (Fig. 1.16), making the tag readability more independent to the particular tag position and orientation.
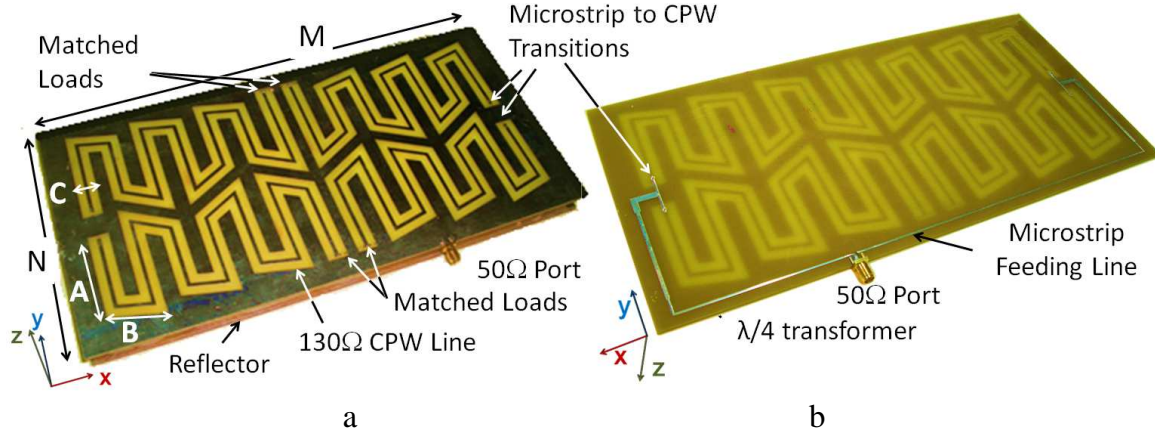
Fig. 1.16 - Antenna prototype: (a) top view and (b) bottom view. The main geometrical parameters are: A=45 mm, B=29 mm, C=10.6 mm, M=275 mm, N=136 mm.

A particular attention in the design of this kind of array is needed to maintain the two TWA ground planes at the same potential, in order to avoid the excitation of CPW modes generating unforeseen field distributions. Thus, each of the four meandered CPW lines is connected through a transition (Fig. 1.16) to a microstrip feeding line realized in the bottom FR-4 substrate. A detailed description of the microstrip to CPW transition can be found in [26]. Furthermore, since the reader antenna performance could be affected by the particular desk material, a 275 × 135 mm2 reflector plane (not electrically connected to the antenna) has been placed very close to the bottom of the antenna substrate (about 10 mm of distance). The measured antenna reflection coefficient is shown in Fig. 1.17, and it is below -14 dB in the entire UHF RFID band.
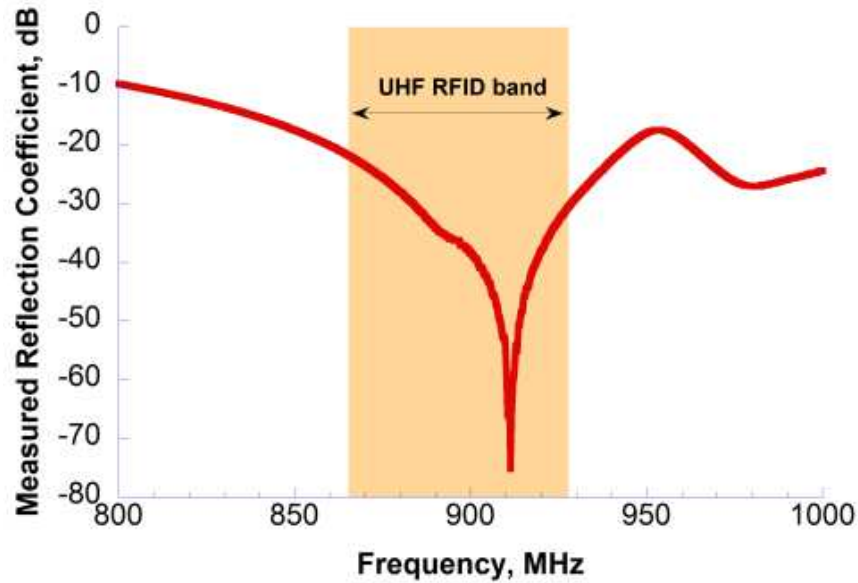
Fig. 1.17 - Measured reflection coefficient of the proposed TWAs array.

In Fig. 1.18 the simulated electric and magnetic field normalized distributions at the frequency of 900 MHz are shown, considering an XY-plane parallel to the antennas surface at a distance of 100 mm. As comparison, the simulated field distributions of the single-line Snake Antenna [22] are reported. The distributions are normalized to the electric and magnetic field maximum values between the two antennas. It is worth noting that, thanks to the TWAs array configuration, the generated fields have been shaped to obtain the field uniformity in correspondence of the central area of the antenna.

In order to evaluate the performance in a real scenario, the proposed antenna has been integrated into a commercial desktop reader and read range tests have been carried out. In this test, the UH414 (Lab-ID) tag has been chosen, and the antenna surface (275 × 135 mm^2) has been subdivided into 4×9 square cells. The detection tests have been repeated in each cell by varying the distance of the tag from the antenna surface, setting an input power to 23 dBm. In Fig. 1.19 the results are shown for two orthogonal orientations of the tag. Since the meandered lines cover almost the entire available area (275 × 135 mm^2), the tag is read in any location and orientation when it lies directly above the antenna surface. By increasing the tag distance from the antenna surface, the UH414 tag has been mainly detected in the central area of the TWAs array, as expected from the simulated field distributions. Moreover, the tag detection is only slightly dependent on the particular orientation. Finally, such tag detection tests show that the read range is limited up to 10 cm, so avoiding false positives readings in the desired detection volume.
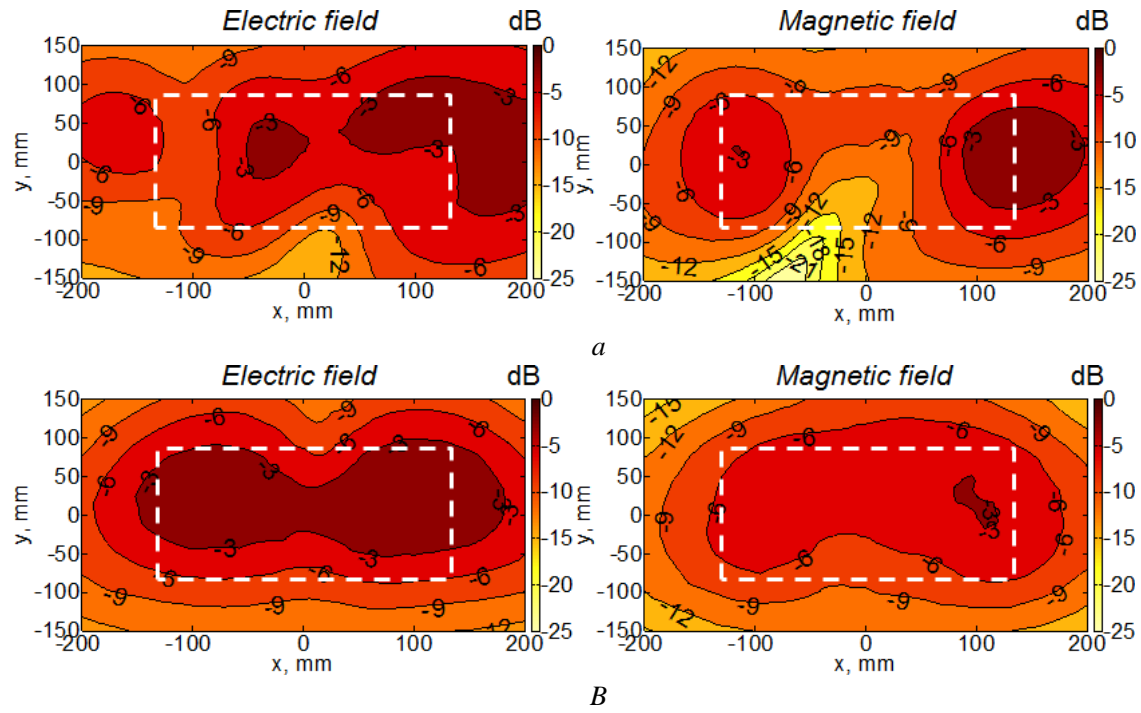
Fig. 1.18 - Normalized electric and magnetic field distributions on an XY-plane parallel to the antenna surface at a distance of 100 mm (f_0=900 MHz): (a) Snake Antenna and (b) TWAs Array. The dashed line represents the antenna boundary (275×135 mm^2).
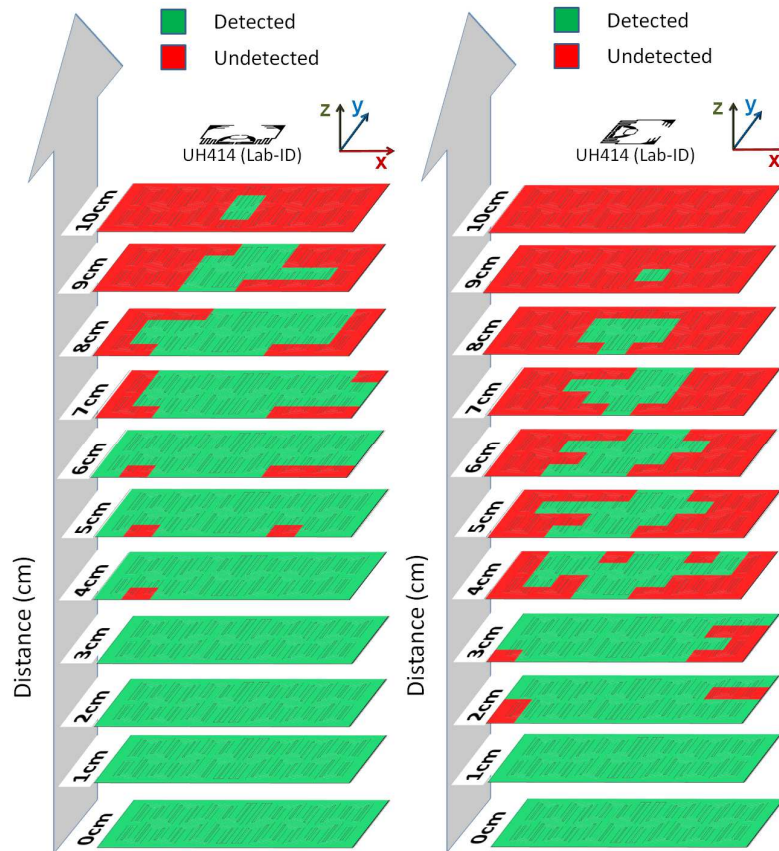
Fig. 1.19 - Tag detection test for the UH414 tag, by varying the distance, the position and the orientation with respect to the antenna surface. The input power has been set to 23 dBm.

1.5   Conclusions

A novel low-profile, low-cost, scalable, wideband travelling wave antenna based on the coplanar waveguide technology has been designed for NF UHF-RFID systems (865-928 MHz). A meander TWA layout has been adopted to obtain an almost homogeneous field distribution (no deep minima) for all field components above the antenna surface, so reducing the effect of tag position/orientation on the detection rate performance. A planar metallic reflector has been added in order to make the antenna independent to the particular supporting plane material. A low antenna gain (required to avoid cross readings outside the confined and predetermined detection volume above the antenna surface) is given by the losses in the matched load connected to one antenna end, which also avoids a standing pattern for the surface current on the antenna.

A number of antenna parameters (e.g. meanders number and size, CPW line characteristic impedance, distance between two adjacent lines, CPW line profile) are available to the antenna designer to easily control the antenna far-field gain and impedance matching, and to match detection volume to the required size specifications (design criteria have been explicitly discussed all through the paper). Above feature makes the proposed antenna suitable for several NF UHF-RFID applications, other than RFID desktop readers, as for example for access control gates, smart shelves/tables and any other UHF-RFID-based system requiring a confined and properly shaped tag detection volume.

An antenna prototype has been used with a commercial reader to test system performance in terms of reading range, by considering both short- and long-range commercial tags. When fed with a reader output power of 23 dBm, the proposed *Snake Antenna* is able to detect the short-range and the long-range tag up to 10 cm and 50 cm, respectively, in more than 50% of the whole antenna surface. Moreover, such an antenna is able to detect tags up to 11 cm when they are stacked above the antenna cover.

Moreover, an array of travelling wave antennas based on the CPW technology has been also proposed for NF-UHF RFID desktop reader applications. The presence of 2×2 radiating elements allows to obtain a field distribution uniform above the antenna and maximized in the broadside direction. Tag detection tests demonstrate that such an array configuration allows for the detection of tags placed in the antenna central area, up to 10 cm from the antenna surface, satisfying typical system requirements for NF-RFID applications (*e.g.* smart point readers, smart drawers, smart shelves).

2 A Multifunctional Modular Antenna for Near-Field UHF RFID Readers

2.1 Introduction

The antenna near-field (NF) features have been applied in different contexts: short-range radio systems (Near Field Communications [27], microwave wireless power transfer [28], Radio Frequency IDentification (RFID) systems [5],[7]. In such a framework, NF UHF RFID systems for item level tagging applications have been developed, with the advantages of higher reading and data rates, and smaller tag antennas, with respect to HF RFID systems.

Near-field antennas are employed in different UHF RFID applications such as desktop readers, smart shelves, smart drawers, smart point readers, RFID portals. The purpose of a NF UHF RFID system is to guarantee the tag detection only within a confined volume, preventing the false-positives issue [29]. Inside the specified volume, the reader antenna has to radiate an as homogeneous as possible amplitude distribution for all field components, since the tag may be located in an arbitrary location, with any orientation too. Segmented loop antennas have been proposed to get an almost constant current distribution in a physically large loop, where contiguous loop segments are connected by lumped [8] or distributed [9],[30],[31] capacitive elements. Moreover, a reader antenna based on double-sided parallel-strip line (DSPSL) is presented in [32]. However, getting a $50\,\Omega$ impedance matching in the whole UHF RFID band is quite awkward for these loop-like configurations, due to both the low radiation resistance and the high reactance typical of loop antennas. Then, a proper matching network is needed [8], [9], [30],[31]. Fractal antennas [33] and array of printed metal strips [34], patches [12],[13] or slots [14] have also been designed, for UHF and high UHF (e.g. 2.4 GHz) frequency bands.

Above mentioned solutions consist of resonating antennas whose size is specified by

the operating frequency, thus they do not represent a scalable solution for those applications requiring an antenna of specific size, as for example in desktop readers or RFID-based smart shelves. In such a framework, travelling wave antennas (TWAs) have been recently proposed for NF UHF RFID systems [15],[16],[18][19][20][21][22][36], since their length and shape are not strictly related to the operating frequency (non-resonating structures). A printed TWA can represent a low-cost, scalable, wideband, and low-profile solution, which allows for an easy shaping of the electromagnetic field in a confined volume nearby to the antenna surface. Furthermore they are able to create a strong and uniform field distribution just above the antenna surface, where the tag is supposed to lie on and the impedance matching can be easily obtained in the whole UHF RFID band. Different technologies have been employed to realize TWAs: microstrip line technology with several layouts (single straight line [15], slight meandered line [16], coupled meandered line [18] or two spiral-shape lines [19]), CoPlanar Stripline (CPS) technology [20],[21] or CoPlanar Waveguide (CPW) technology [22],[36]. In most of the afore-described TWA-based layouts, a good tag readability is obtained when the tag lies right on the antenna surface. However, the achievable read range is usually limited to a few centimeters, depending on the tag employed for the tests. For the smart shelf antenna in [15], a good tag readability is obtained on the whole antenna surface (747 mm×176 mm) up to a distance of around 3 cm, when using a NF button tag with a 30 dBm reader output power. Similar performance is obtained for the smart shelf antenna in [20] and the desktop reader antenna in [21], where the reading distance reaches 7 cm in the antenna central area. Better results are obtained with the desktop reader antenna (150 mm×150 mm) in[19], which guarantees a reading distance up to 35 cm with an input power of only 20 dBm. As described in [22], a reading distance of around 55 cm can be reached on 60% of the desktop reader surface (275 mm×135 mm) with 23 dBm input power (the long range tag Alien ALN 9640 was used). In [16], three Alien ALN 9640 tags can be simultaneously read up to 15-20 cm from the desktop reader surface (275 mm × 220 mm) for 30 dBm input power.

In real-world applications, tag detection must be effective also for tagged items stacked on the reader surface, in a pile or in bulk. Then, it is mandatory to reduce the rate of the field amplitude spatial decay along the direction perpendicular to the reader surface, as well as along directions parallel to the reader surface (when moving from the antenna center to the borders). A TWA structure is effective to get a homogeneous and strong field right on the antenna surface, but the field amplitude decays rapidly away from the antenna surface. To extend tag readability up to a few decimeters from the antenna surface, a modular antenna concept has been proposed by the authors in [37]. The modular antenna comprises a TWA and a low-gain resonating antenna, which are combined to meet specific requirements on the spatial decay rate and amplitude of the radiated field, in the reactive and radiative near-field regions [6].

In this Chapter, a specific layout implementing the modular antenna concept firstly presented in [37] is selected, and a desktop reader antenna for the FCC UHF RFID band is designed and characterized at system level. A spiral-shaped microstrip line is series-connected to a low-gain array of two miniaturized patches, to get an as homogenous as possible field distribution up to a distance of 60 cm from the antenna surface. Besides, by simply adding a switch, the spiral microstrip line can be either connected to the array

or ended on a matched load to implement a conventional TWA. The latter configuration ensures a strong and uniform field distribution in a small volume just above the antenna surface, which is high desirable for tag writing operations or single-tag readings.

The Chapter is organized as follows. The modular antenna operating principle is summarized in Paragraph 2.2. Then, the proposed antenna layout is described in Paragraph 2.3, together with some simulation results. Measured antenna performance in terms of RSSI (Receive Signal Strength Indicator) distributions on the desktop reader surface is shown in Paragraph 2.4. Reading tests for stacked tags and writing tests are also shown.

2.2   Multifunctional Modular Antenna: Operating Principle

The main operating characteristics of a NF UHF RFID antenna for desktop readers can be summarized as follows:

a) VSWR less than 1:1.5 to limit the power reflected toward the reader RF front-end;

b) low far-field gain to limit false positives (unintended detection of tags that are located outside the specified detection volume);

c) electric and magnetic fields as uniform and high as possible on the antenna surface, to allow successful reading/writing operations, independently on the tag location above the reader antenna surface;

d) low field amplitudes behind the reader antenna where tags are not supposed to be located;

e) electric and magnetic energies almost uniformly distributed among all the near-field components to allow successful reading/writing operations independently on the tag spatial orientation;

f) a thin layout, also scalable to almost any size, to meet application and market requirements.

The general scheme of a modular antenna [37] that can satisfy above requirements up to a few decimeters from the reader surface is sketched in Fig. 2.1. A TWA (ANT1) is located at the center of the desktop reader surface. One of its ends is the feeding connector, while the other end is connected to either a low-gain resonating antenna positioned at the reader borders (ANT2) or a matched load. If the TWA is ended on the matched load, the detection volume is limited to a small region right above the TWA surface (reactive near-field region). The detection volume is extended to include the radiative near-field region when the TWA end is connected to the low-gain resonating antenna.
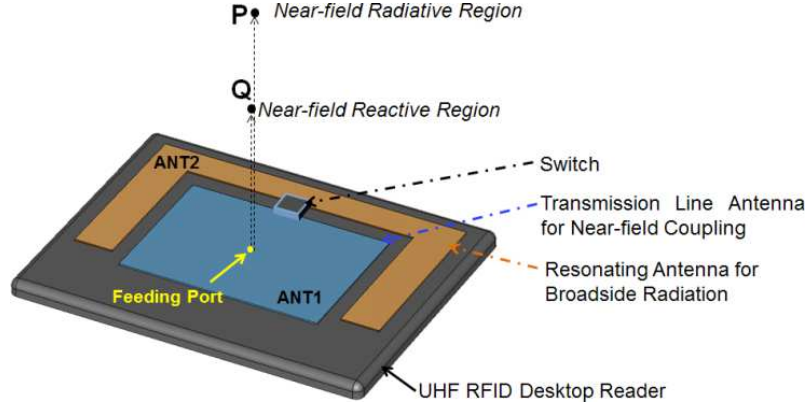
Fig. 2.1. - General scheme of a modular antenna for NF-UHF RFID desktop readers: a central near-field travelling wave antenna and a low-gain resonating antenna located at the reader border. The switch allows to connect the TWA end port to either the resonating antenna or a matched load.

The TWA has been chosen to increase the field amplitude on the antenna surface, with respect to a conventional low-radiation microstrip or CPW printed line. Spiral or meandered structures are preferred to distribute the electromagnetic (EM) energy among all the field components. The TWA is favorably located at the middle of the reader surface, where a tagged item is more likely located. The resonating antenna (ANT2 in Fig. 2.1, which is placed in the TWA surrounding region, can be optimized to cover the radiative near-field region with a circularly polarized field. Since most of the reader surface must be used to accommodate the TWA antenna, a miniaturized layout is preferred to realize the resonating antenna. It is worth noting that the miniaturization also helps to meet the low far-field gain requirement. Moreover, thanks to the series connection between the two modules (with one end of the TWA directly connected to the reader circuit output), return loss requirement can be met in a relatively large bandwidth. The matched load is needed to avoid a current standing wave when the TWA is implemented, since this can degrade field uniformity on the reader surface. The orientation and layouts of the two antenna modules have to be chosen by considering that the mutual coupling between the radiators sharing the reader surface is not negligible, since the radiating elements are very close to each other and they must operate at the same frequency.

2.3   Antenna Layout and Numerical Results

The multifunctional modular antenna for near-field UHF RFID readers here proposed represents a specific implementation of the modular antenna concept introduced in Sect. II.

The antenna layout is shown in Fig. 2.2. A 50-Ω coaxial cable, placed close to the antenna surface center, feeds a spiral-shaped microstrip TWA printed on a grounded 1.6mm-thick FR4 (ε_r=4.4, $tan\delta$=0.025) dielectric substrate. The TWA is an archimedean spiral of width W_1=3 mm, with around 7 turns that are 4.8 mm apart from each other. The TWA is series connected to either a planar array of two miniaturized circularly-polarized square patches [38],[39] (Fig. 2.2a, *Modular Antenna Configuration*) or a matched load (Fig. 2.2b, *Spiral TWA Configuration*).

(a)

(b)
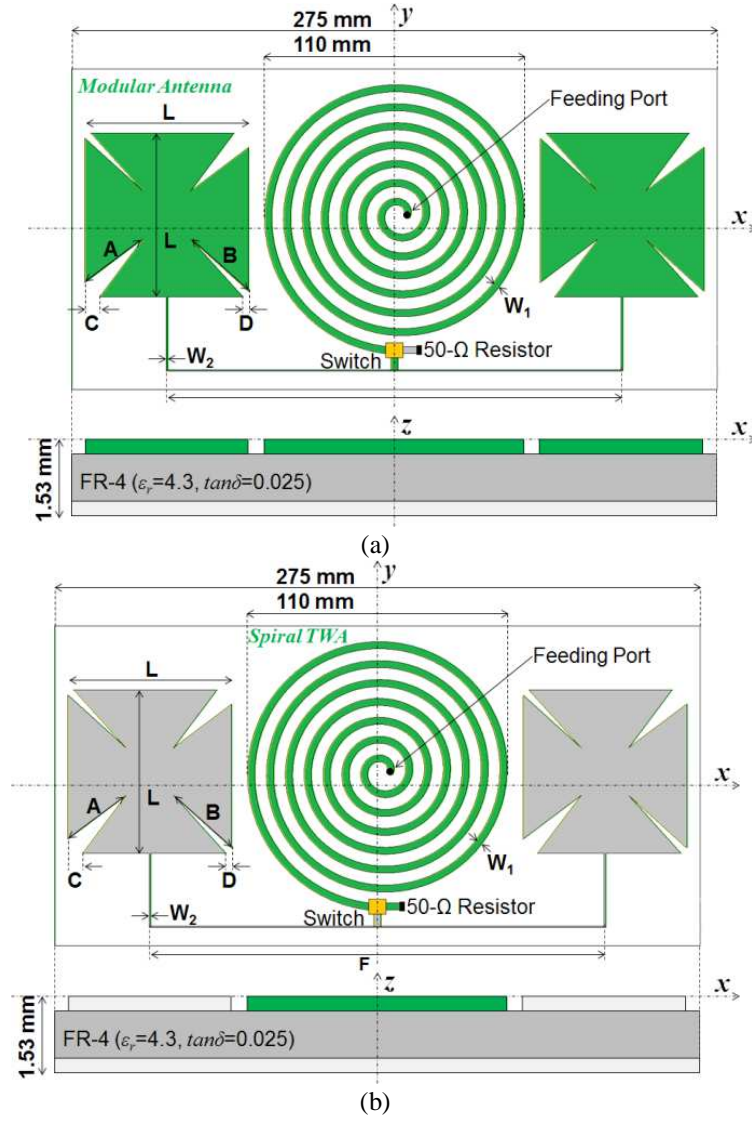
Fig. 2.2. - Top and lateral view of the proposed NF *Multifunctional Modular Antenna* for UHF RFID desktop reader applications: (a) *Modular Antenna Configuration* and (b) *Spiral TWA Configuration*. For each configuration related to the switch position, the radiating elements are denoted by a light colour. The main geometrical parameters values are listed in Table I, for an UHF RFID FCC band (902-928 MHz) reader.

The simulated reflection coefficient (Fig. 2.3) is below -14 dB in a frequency range that is much larger than the UHF RFID FCC band (902-928 MHz), for both the *Modular Antenna Configuration* (solid line) and the *Spiral TWA Configuration* (dashed line).
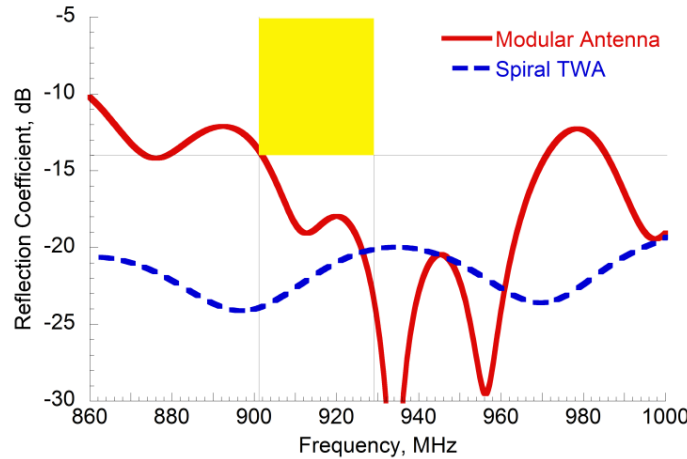
Fig. 2.3. - Simulated reflection coefficient versus frequency for the *Modular Antenna Configuration* (solid line) and the *Spiral TWA Configuration* (dashed line), in the UHF RFID FCC band.

TABLE I
MULTIFUNCTIONAL MODULAR ANTENNA DIMENSIONS
FOR UHF RFID FCC BAND READERS.

Parameter	A	B	C	D	F	L
Value (mm)	31	33.4	6.2	2.4	194	69.7

In Fig. 2.4, the broadside gain of the *Modular Antenna Configuration* (solid line) is compared with that of the *Spiral TWA Configuration* (dashed line). As expected, the far-field gain (dashed line) of the *Spiral TWA* (when the latter is closed on a matched load) is very low (about -13 dBi). This low value advises that a *TWA* ended on a matched load cannot be used alone if a reading range more than a few cm is required. The broadside gain of the *Modular Antenna* is about -5 dBi, with variations less than 2 dBi in the whole UHF RFID FCC band. Such a value accounts for both the array gain and the TWA insertion loss. It is large enough to allow tag detection in the antenna radiative near-field region, yet minimizing false-positives events outside the defined detection volume.
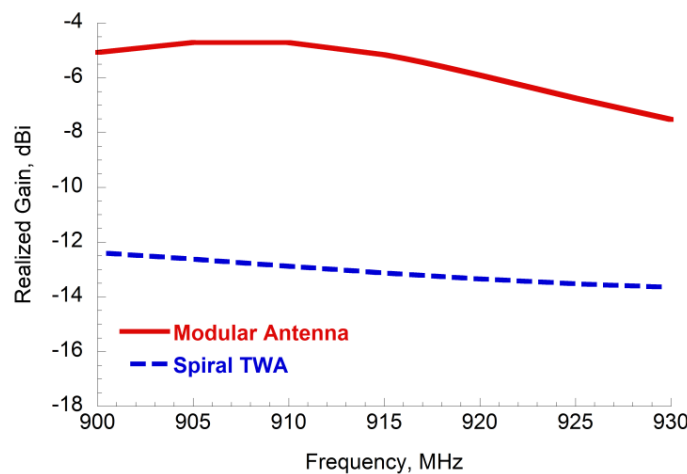
Fig. 2.4. - Simulated broadside far-field gain versus frequency for the *Modular Antenna Configuration* (solid line) and the *Spiral TWA Configuration* (dashed line), in the UHF RFID FCC band.

2.3.1 Electric and magnetic field distributions

Since both dipole-like tags and loop-like tags can be employed in NF UHF RFID systems, it is important to analyze both the electric and the magnetic near-field distributions.

In Fig. 2.5-8 the simulated electric and magnetic field distributions of both antenna configurations are shown, in the *xy*-plane and the *xz*-plane, at 915 MHz.

(a)

(b)
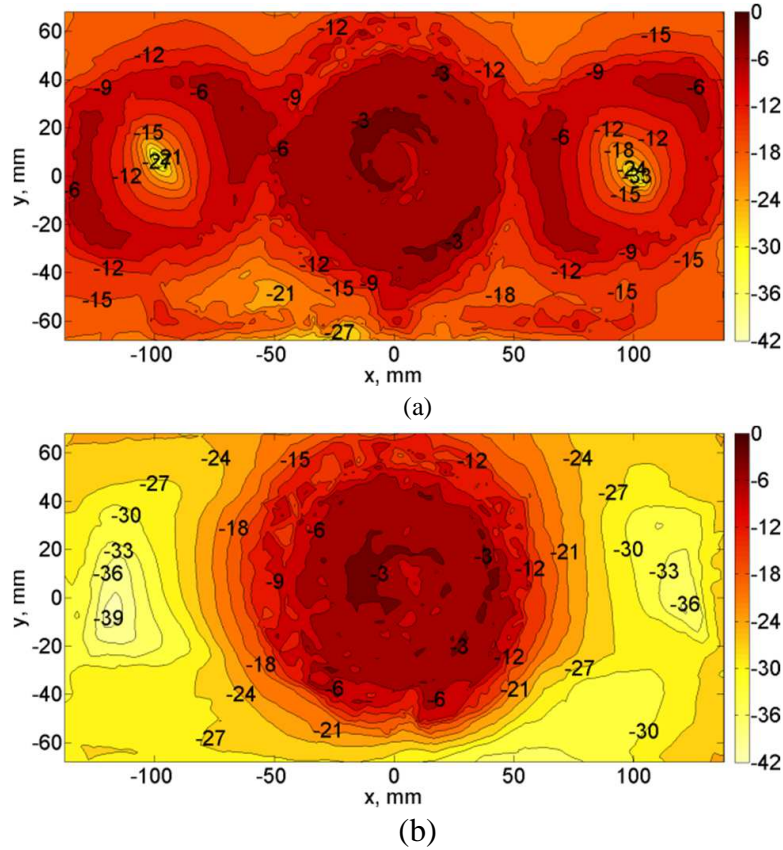
Fig. 2.5. - Normalized electric field distribution (dB) on a plane parallel to the antenna surface (*xy*-plane) at a distance of *z*=1 cm and f_0=915 MHz: (a) *Modular Antenna Configuration* and (b) *Spiral TWA Configuration*.

(a)

(b)
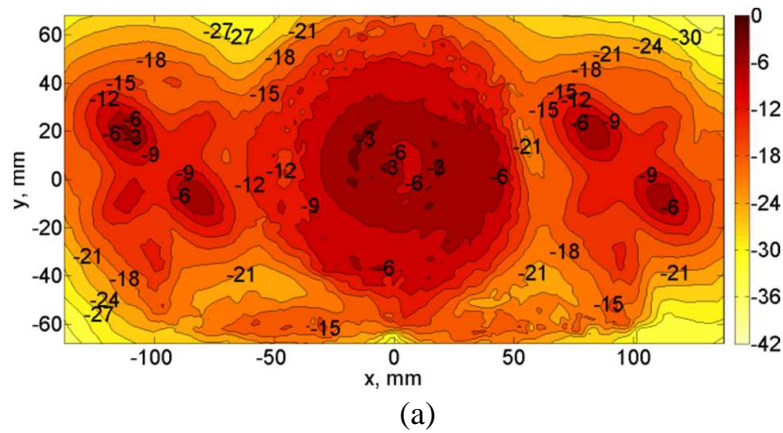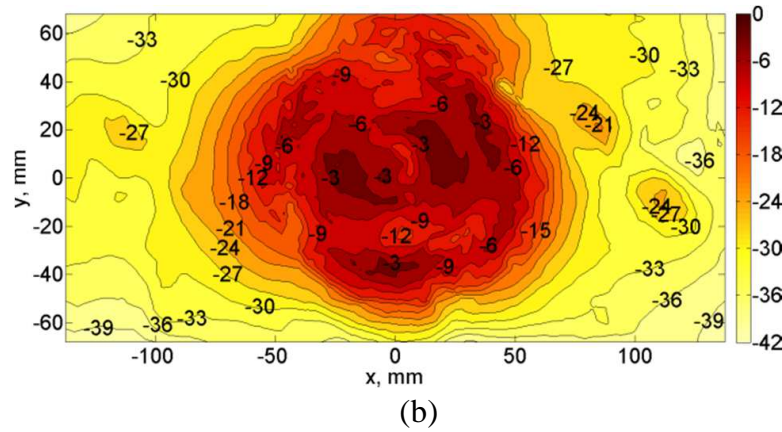
Fig. 2.6. - Normalized magnetic field distribution(dB) on a plane parallel the antenna surface (*xy*-plane) at a distance of z=1 cm and f_0=915 MHz: (a) *Modular Antenna Configuration* and (b) *Spiral TWA Configuration*.

(a)   (b)
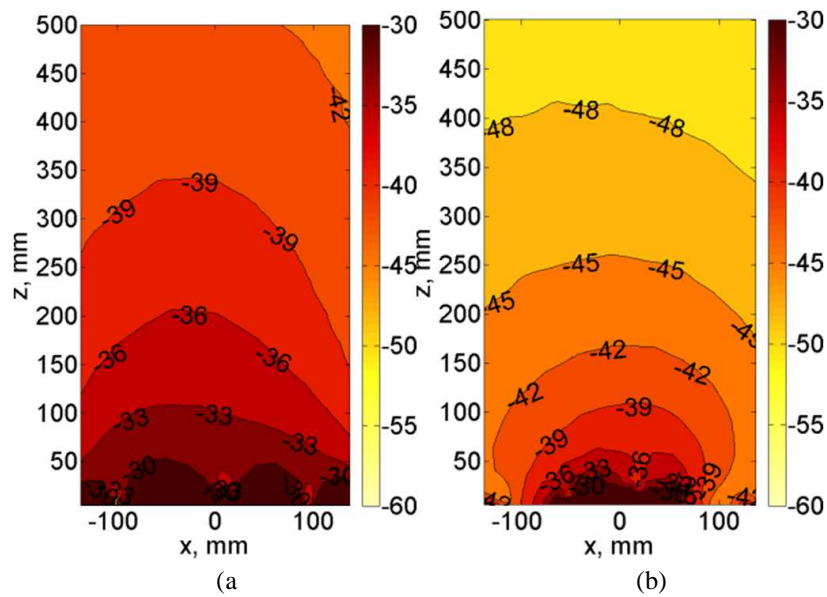
Fig. 2.7. - Normalized electric field (dB) distribution on an orthogonal plane (y=0) and f_0=915 MHz: (a) *Modular Antenna Configuration* and (b) *Spiral TWA Configuration*.

(a)   (b)
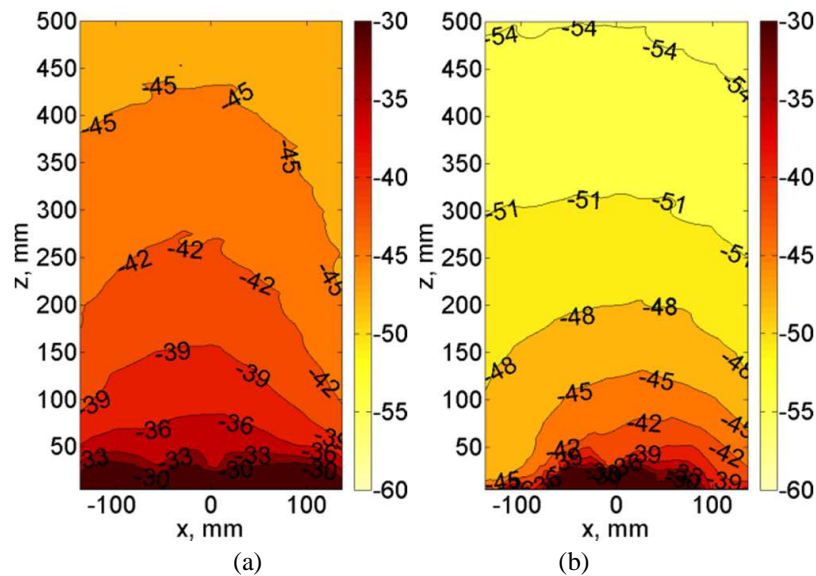
Fig. 2.8. - Normalized magnetic field (dB) distribution on an orthogonal plane (y=0) and f_0=915 MHz: (a) *Modular Antenna Configuration* and (b) *Spiral TWA Configuration*.

The *xy*-plane parallel to the antenna surface has been chosen at a distance of z=1 cm (Fig. 2.5-Fig. 2.6), and the *xz*-plane is chosen at y=0 cm (Fig. 2.7-Fig. 8), where (x,y)=(0 cm, 0 cm) is the overall antenna center. For each plane, the field distributions are normalized to the maximum field value among the two antenna configurations.
The *Spiral TWA Configuration* exhibits an almost uniform field distributions (Fig. 2.5b-Fig. 2.6b) on the antenna central area. Moreover, filed amplitude reduces significantly close to the reader borders and away from the surface, so confirming the expected rapid amplitude spatial decay.

On the other hand, the *Modular Antenna* radiates a field whose amplitude decreases more slowly (Fig. 2.7a-Fig. 8a), as it is required when multiple tagged items are stacked on the reader surface. It is worth noting that the slits in the metallic patches are effective to give a satisfactory field uniformity even in the surface section surrounding the TWA, except for the expected deep nulls of the electric field at the patch center (Fig. 5a).

2.4   Antenna Reading/Writing Performance

To simplify the antenna construction, two different prototypes have been fabricated, one for the *Modular Antenna Configuration* (see a photo in Fig. 9a) and one for the *Spiral TWA Configuration* (see a photo in Fig. 9b).

(a)   (b)
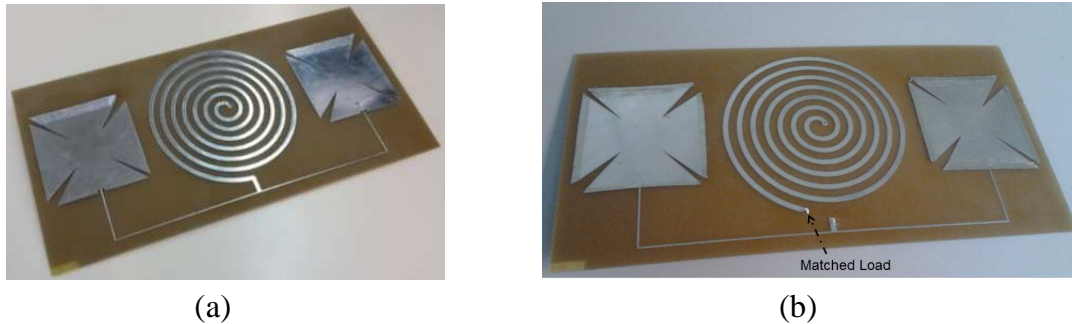
Fig. 2.9. - Prototype of the modular antenna for the UHF RFID FCC band: (a) *Modular Antenna Configuration* and (b) *Spiral TWA Configuration.*

By doing this, we avoided to add the switch into the prototypes. It is worth noting that the patch array is present in both prototypes (even if the array is disconnected in the *Spiral TWA Configuration*), to account for the effect of the mutual coupling between the spiral TWA and the patches.

The antenna prototypes have been integrated into a desktop reader case (30 cm $\times$ 18 cm) and connected to the CAEN reader module A528[40] Tests have been performed by using compact-dipole LABID UH414 tags [41]. The reader output power has been set at 23 dBm.

2.4.1   Reading/Writing tests for single tag

The detection tests have been repeated in each of the 33×33 cells in which a 99 cm×99 cm plane coplanar to the antenna surface has been subdivided into (cells sizes are $\Delta x=\Delta y=3$ cm). In Fig. 2.10, the RSSI and read rate distributions are shown, for the tag orientation parallel to *x*-axis and *y*-axis, on the entire square plane.

For each cell, the RSSI value has been obtained by averaging the RSSI samples collected in a 10 s interval.

When the *Modular Antenna Configuration* is employed, the tag can be read at any tag position and orientation on the reader surface (Fig. 2.10a and Fig. 2.10b). Also, there are no false positives if tagged items in the case surrounding are located at more than 10-15 cm from the case edge. The average read rate on the antenna area is around 8 tag/s. Reading performance is worse at the lower edge of the desktop reader, where the reader electronic circuit is accommodated.

By using the *Spiral TWA Configuration*, the tag is read when it lies directly above the antenna central area (Fig. 2.10c and Fig. 2.10d). By approaching the antenna borders, the tag detection fails, so successfully avoiding false positives. For both tag orientations, an average read rate of 8 tag/s has been measured in a detection area of about 4×5 cells (12 cm × 15 cm).

To measure the reader antenna read range, further tests have been carried out by moving the tag away from the antenna surface, with a step of 5 cm. At each distance, the RSSI value has been averaged in an interval of 10 s, for two orthogonal tag orientations. The read ranges (Fig. 2.11) are around 10 cm and 60 cm for the *Modular Antenna Configuration* and the *Spiral TWA Configuration*, respectively, regardless of the tag orientation. This result is in agreement with the difference between the simulated gain values of the two configurations (Fig. 2.4).

(a)

(b)

(c)

(d)
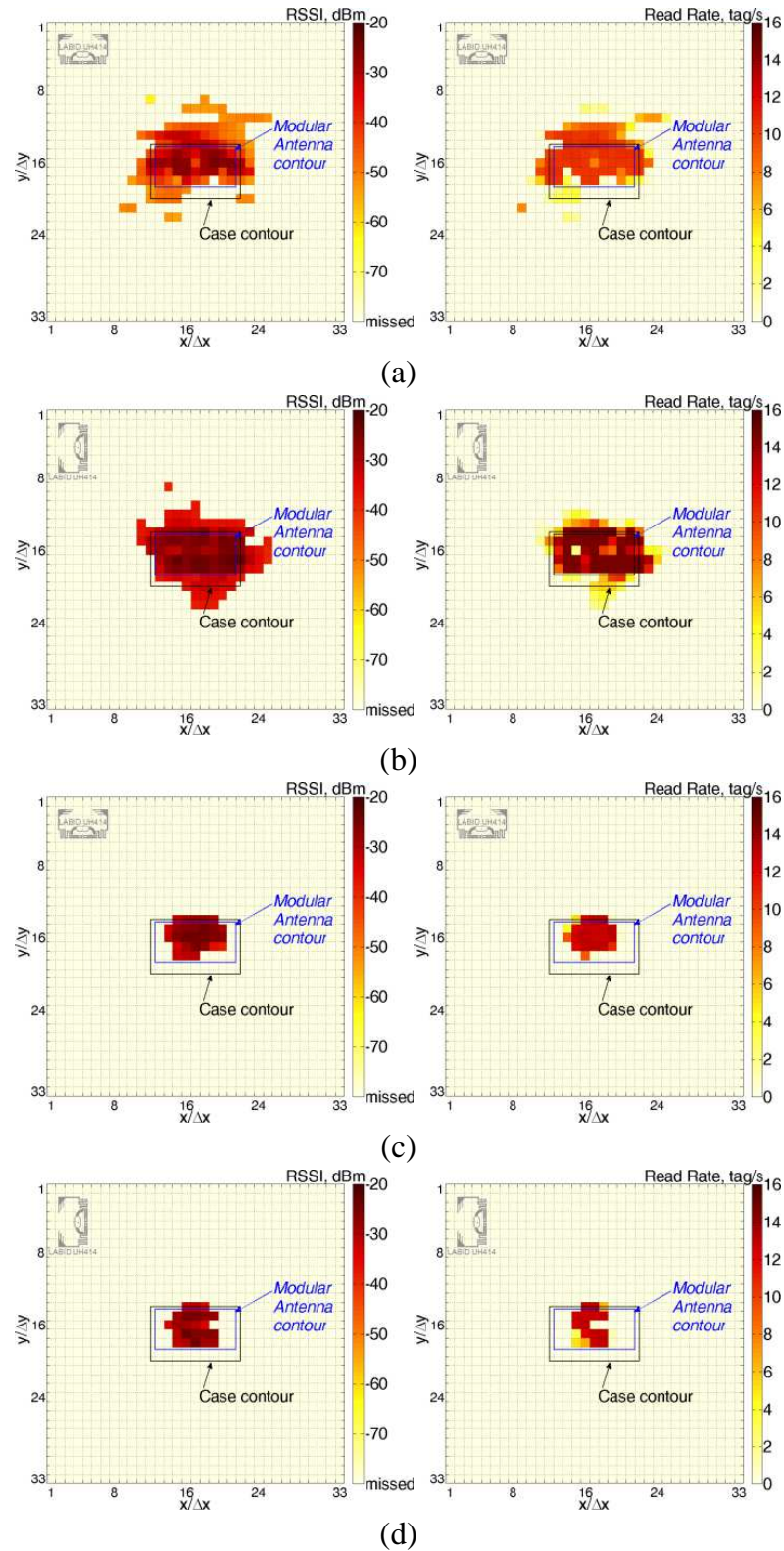
Fig. 2.10. - RSSI (left column) and Read Rate (rigth column) distributions on a 99 cm×99 cm (33×33 square cells with Δx=Δy=3 cm) plane parallel to the desktop reader surface, by using a LABID UH414 tag and a reader otuput power of 23 dBm. The following reader antenna-tag configurations have been considered: (a) *Modular Antenna @ x*-oriented UH414, (b) *Modular Antenna @ y*-oriented UH414, (c) *Spiral TWA @ x*-oriented UH414, (d) *Spiral TWA @ y*-oriented UH414.
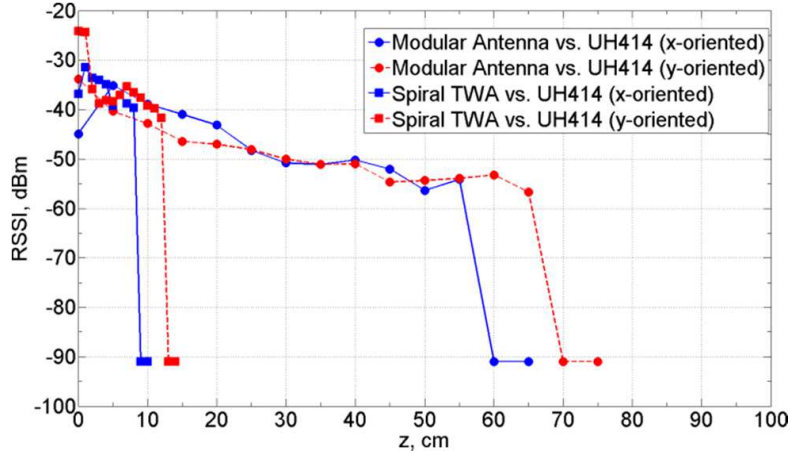
Fig. 2.11. - RSSI distribution by varying the tag (LABID UH414) distance from the antenna center (along a direction perpendicular to the reader surface), with an input power of 23 dBm, for two orthogonal tag orientations and for both antenna configurations.

Writing tests have also been performed, as such operation requires higher field amplitudes with respect to the tag reading operation, and then they represent more demanding tests. Results in terms of writing attempts are shown in Fig. 2.14.

When the *Spiral TWA Configuration* is employed, the area of successful writing is concentrated at the antenna center, and only one attempt is required to initialize the tag for any considered tag position and orientation (Fig. 2.14c and Fig. 2.14d). If the *Modular Antenna Configuration* is used, the area on which the writing operation enlarges and also includes sectors beyond the case border (Fig. 2.14a and Fig. 2.14b). Then, the latter configuration is not suitable if the only tag to be encoded is that one on the reader surface.
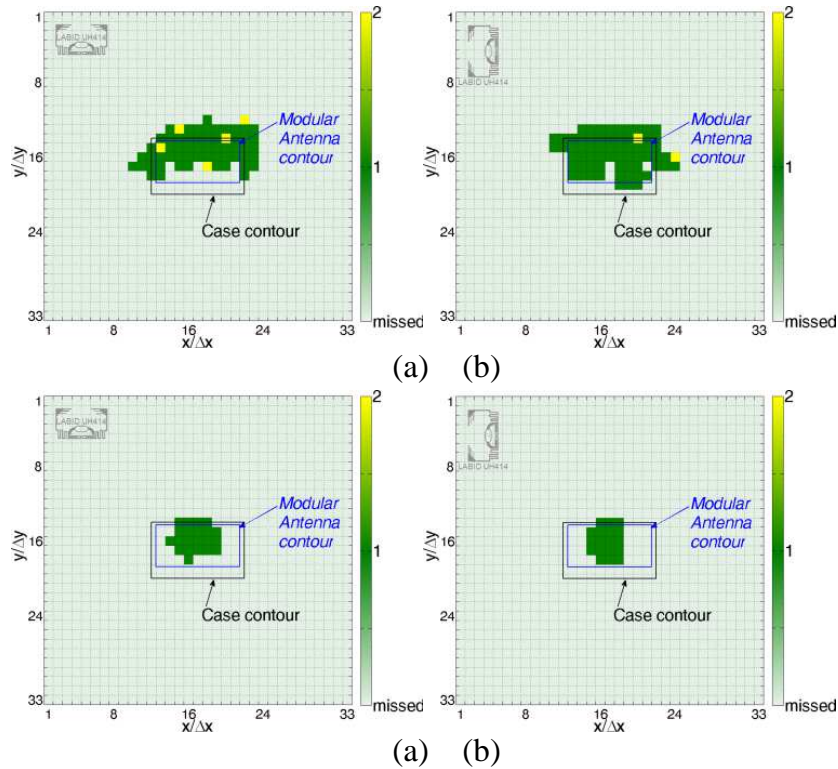
Fig. 2.12. - Number of attempts of writing operations on a 99 cm×99 cm (33×33 square cells with Δx=Δy=3 cm) plane parallel to the desktop reader surface, by using a LABID UH414 tag and a reader otuput power of 23 dBm. The following reader antenna-tag configurations have been considered: (a) *Modular Antenna @ x*-oriented UH414, (b) *Modular Antenna @ y*-oriented UH414, (c) *Spiral TWA @ x*-oriented UH414, (d) *Spiral TWA @ y*-oriented UH414.

2.4.2   Multiple tags detection

Finally, 11 LABID UH414 tags have been placed in a stacked configuration at a distance of 2 cm from each other, up to an overall height of 20 cm (tags are separated by a foam layer). The lower tag has been placed directly on the case surface. The stacked tags readability has been tested on a surface subdivided into 9×5 cells (cells sizes are Δx=Δy=3 cm). The total number of tags that are detected in a 10 s time interval has been recorded, when varying the tag orientation and the stack position on the antenna surface. Results are shown in Fig. 2.13. When using the *Modular Antenna* (Fig. 2.13a-Fig. 2.13b), almost all the 11 stacked tags are read in each cell of the antenna surface, for both orthogonal tag orientations. As for single-tag tests, performance get worse at the desktop reader lower border, where the reader electronic circuit is accommodated. Besides, the *Spiral TWA Configuration* is able to detect just an average number of 5 tags, with a maximum number of 7 at the antenna center, regardless of tag orientation (Fig. 2.13c-Fig. 2.13d). This was expected due to its characteristic rapid field spatial decay. Similar considerations apply to the read rate, which is shown in Fig. 2.14. Indeed, a high read rate is observed for the *Modular Antenna*: 111 tag/s (Fig. 2.14a) and 100 tag/s (Fig. 2.14b) for the *x*-oriented tag and *y*-oriented tag, respectively. For the *Spiral TWA Configuration*, the average read rate on the whole antenna surface is 32.6 tag/s (Fig. 2.14c) and 27.5 tag/s ((a)   (b)

Fig. 2.14d) for the *x*-oriented tag and *y*-oriented tag, respectively. These results

confirm that the proposed multifunctional modular antenna represents a low-cost solution that allow to select the best shape and size of the near-field reader detection volume, as a function of both the operation required (reading or writing) and the number (and material properties too) of the tagged items that the operator is going to put on the reader surface.
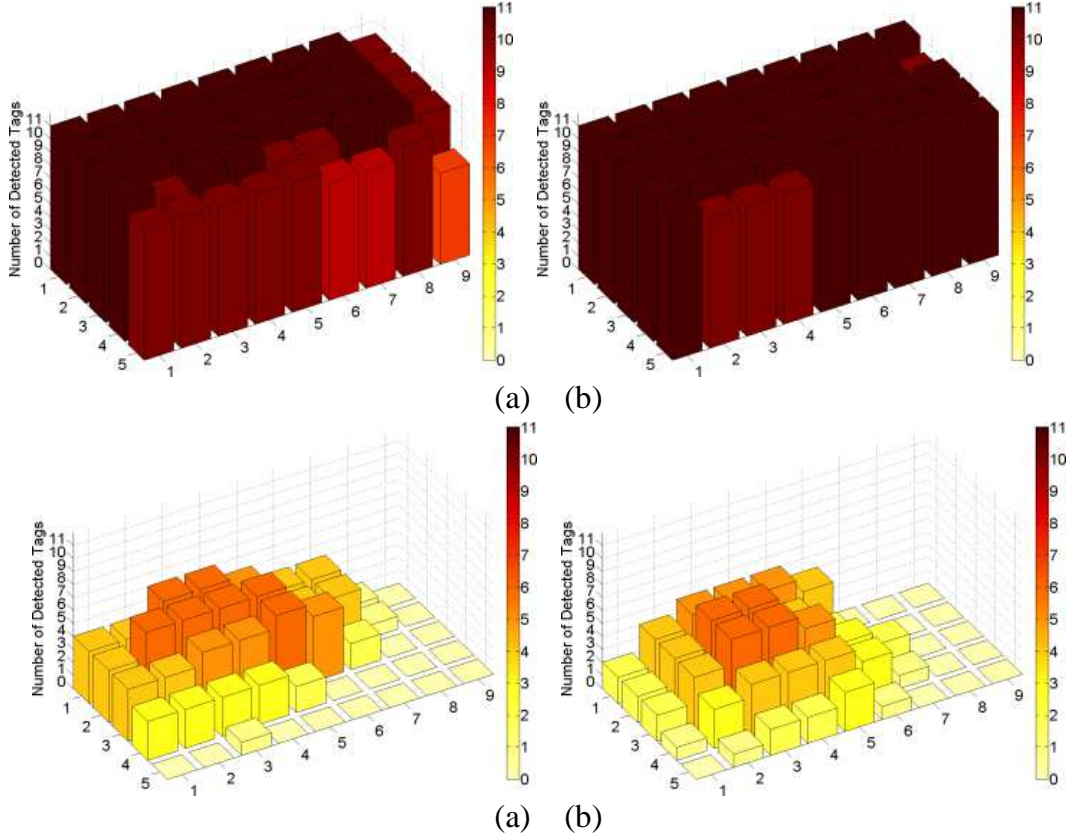
Fig. 2.13. - Number of detected tags on the antenna surface by employing 11 LABID UH414 stacked tags at a distance of 2 cm each other, up to a height of 20 cm (the first tag has been placed directly in contact with the surface of the antenna): (a) *Modular Antenna @ x*-oriented UH414, (b) *Modular Antenna @ y*-oriented UH414, (c) *Spiral TWA @ x*-oriented UH414, (d) *Spiral TWA @ y*-oriented UH414.

(a)   (b)

(a)   (b)
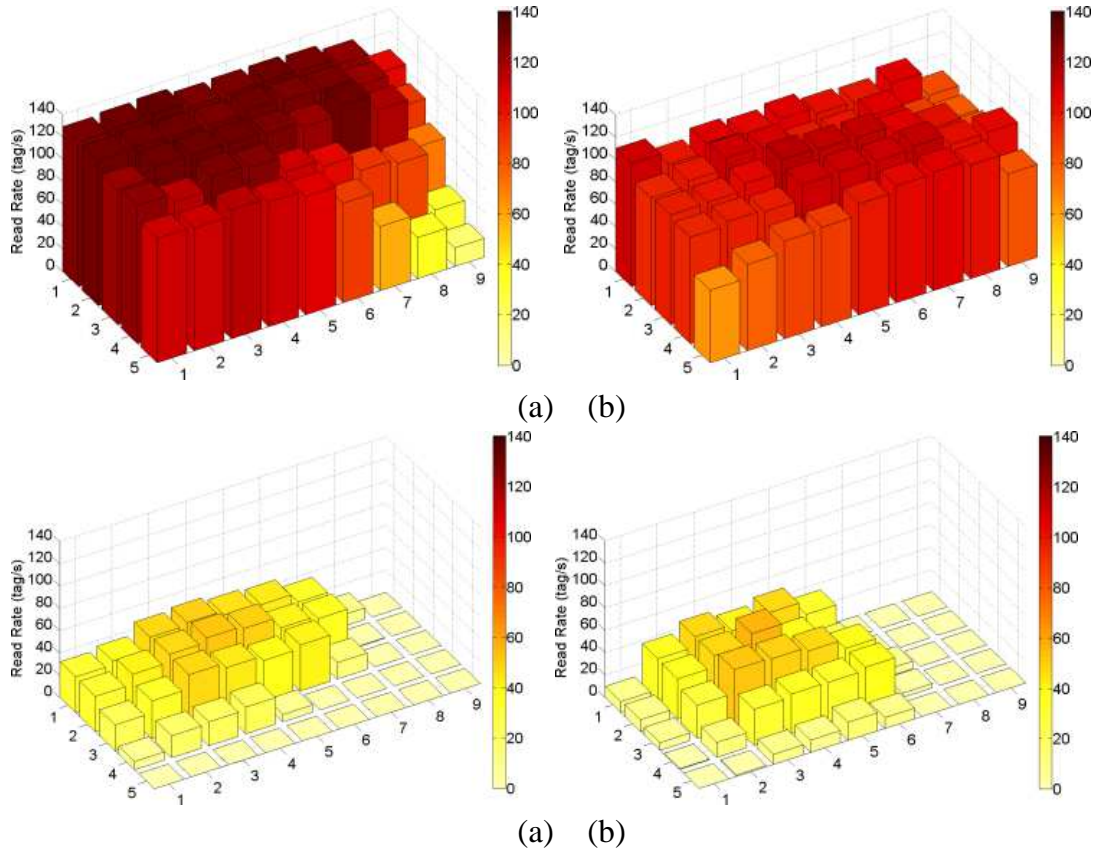
Fig. 2.14. - Read Rate on the antenna surface by employing 11 LABID UH414 stacked tags at a distance of 2 cm each other, up to a height of 20 cm (the first tag has been placed directly on the antenna surface): (a) *Modular Antenna @ x*-oriented UH414, (b) *Modular Antenna @ y*-oriented UH414, (c) *Spiral TWA @ x*-oriented UH414, (d) *Spiral TWA @ y*-oriented UH414.

2.5   Conclusion

A multifunctional modular antenna for near-field UHF RFID desktop readers has been designed and tested. It operates at the FCC band and fits into a reader case whose size is around 30 cm ×18 cm × 1.5 cm. In the proposed layout a spiral-shaped travelling wave antenna is positioned at the center of the reader surface. By using a common switch, the spiral can be connected to either an array of two miniaturized circularly-polarized patches or a matched load. When the spiral microstrip is ended on the matched load, the reader detection volume is limited to a small area at the center of the reader surface. The latter configuration being preferred during writing operations, namely when the only tag to be encoded is most likely placed at the antenna center, or when tagged items are read one at a time. Conversely, if the power at the output of the spiral microstrip is used to feed the array (instead of being absorbed by the matched load), the two-module antenna exhibits a lower rate of the field spatial decay when moving away from the center of the reader surface. The latter feature is of interest when reading of stacked tags is required.

It has to be underlined that by simply adjusting the length of the microstrip spiral (the latter being a non-resonant antenna) the proposed modular antenna can fit in reader cases with shape and size that are different from those here considered by the authors. Full scalability of the proposed antenna is only limited by the topology selected for the

low-gain resonant antenna used to cover the radiative near-field region. Work is in progress to find a class of antennas that can allow the design of modular antennas suitable to meet almost arbitrary shape and size requirements. The latter is an important feature when designing low-profile near-field antennas for RFID-based smart storage spaces (such as drawers and shelves).

Finally, it is worth noting that replacement of the switch with a variable power divider would allow for a further degree of freedom to dynamically size and shape the reader detection volume, in addition to the power control that is already available in any commercial reader.

3 Accuracy of a Conformal Sensor for Estimating Deep Tissues Dielectric Constants

3.1   Introduction

$\mathbf{M}$AGNETIC resonance Imaging (MRI), X-ray and Computerized Tomography (CT) are the most used surgery-free technologies to detect tumors and produce deep tissues images. Nonetheless, they are not able to provide real time human tissue characterization, as they are not body-worn systems. Also, they are expensive and not portable for use in rural areas or in the field for emergency diagnostics.

There is of course a strong need to develop low cost health monitoring devices. Devices such as those in [42]-[43] pursue monitoring of breathing, heart rate, temperature or blood pressure monitoring. But these devices are not suitable for imaging as they penetrate only few cm within the skin.

Toward this goal, a new on-body health-monitoring sensor was proposed in [44]-[46]. This is a multi-probe sensor operating at 40MHz, providing penetration depth of 10-15 cm within the human body. Therefore, it can be used to sense deep tissue dielectric properties. Specifically, the dielectric constant of the medium of interest is calculated using a linear combination of the S-parameters measured at the sensor's passive probes. In this way, the classic inverse-scattering approach is avoided. That is, we avoid the solution of ill-posed matrices [47]-[50]. As claimed in [45], experimental results have demonstrated that the proposed method can provide dielectric constant estimation with accuracy better than 11%. However, this level of accuracy is not sufficient. Therefore, there is a need to improve the imaging accuracy (dielectric constant prediction) down to 2-3% by optimizing the sensor in [45].

In this Chapter, a numerical study is performed to better assess the algorithm's prediction capability and determine critical parameters that affect its accuracy. Specifically, a stratified dielectric medium is used to model the human torso. The probe

sensor is a linear arrangement of transmitting and receiving ideal dipoles sources or probes (see Fig. 3.1). For a specific excitation, spectral domain Green's function is used to calculate the received fields at the probe locations. The dielectric constant at a specific depth inside the torso is then expressed as a weighted sum of the computed electric field samples. General guidelines for sensor design optimization are extracted and employed to achieve dielectric constant estimation with accuracy better than 3%.

Chapter III is organized as follows. In Paragraph 3.2 the overall imaging sensor concept is briefly described. The proposed model and numerical approach used to estimate the deep tissues dielectric constant is then presented in Paragraph 3.3. In Paragraph 0, we discuss the results and give guidelines for further improvement of the sensor design.

3.2 Sensor Overview

The sensor concept to estimate the dielectric constant has been presented in [44]-[46], and is briefly summarized below. The proposed sensor consists of a finite set of electrodes, as in Fig. 3.1. Only one port (a port is the gap between two electrodes) is fed by a 40MHz input signal, while the rest are used for receiving the radiated fringing field after propagation and attenuation into the tissues.
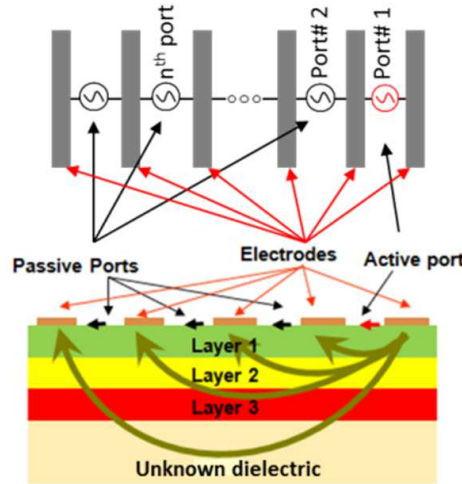
Fig. 3.1. - Top and lateral view of the multi-probe sensor. The electric field force lines inside the medium are also shown.

Specifically, the S-parameters are collected from the passive ports, denoted as $S_{i,1}$, where i=2, 3,….16. Port #1 is always active and the others terminated with a matched load. Using the collected $S_{i,1}$ parameters, the dielectric constant (ε_r) is then represented by a weighted sum of the measured scattering parameters via the relation

$$\varepsilon_r = \sum_{i=2}^{N} w_{i-1} S_{i,1} \tag{1}$$

The coefficients w_i in (1) are computed to minimize the error in approximating ε_r for a set of known configurations. That is, they are determined by enforcing (1) for several combinations of assigned outer tissue layers and known values of the inner layer dielectric constant [46]. This process generates a system of equations solved via a least squares method to extract the coefficients w_i in (1). Measurements given in [46]

confirmed the effectiveness of the representation (1). However, for the selected sensor, the estimation error was up to 11%. Below, we examine the needed sensor length and required number of probes to obtain accuracies down to 2-3%.

3.3   Layered Model

To optimize the sensor length and number of probes for minimal error, we consider an ideal dipole excitation depicted in Fig. 3.2(b). The excited infinitesimal dipole is oriented along the *x*-direction. Also, instead of measuring the fields as the voltage between two electrodes, for the computational model we will simply use the *x*-directed electric fields along the *y*-axis (see Fig. 2(b)). These fields are, of course, proportional to the voltage between the electrodes and will be used to represent the $S_{i,1}$ values in (1). We specifically chose to examine the surface fields up to 30cm away from the dipole excitation. That is, we examined sensor lengths up to 30cm.
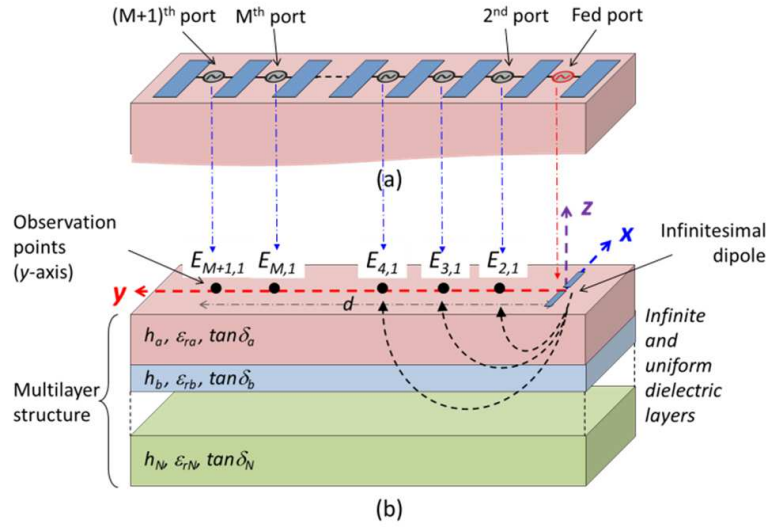
Fig. 3.2. - (a) Actual multi-probe sensor with ports, and (b) multi-layer model for dipole excitation simulation.

Spectral field representations are used to formulate the problem since simpler calculations are involved (algebraic instead of convolution integrals). Let us consider the radiation of an infinitesimal dipole located on the surface of a stratified medium (along the x axis) as shown in Figure 1. The Fourier transform of the x component of the electric field can be expressed as in [51]:

$$\tilde{E}_x(k_x, k_y, z) = \frac{-jZ_1}{k_1}\tilde{J}_x(k_x, k_y)(k_1^2 - k_x^2)\left(\frac{-j}{2}\right)\frac{e^{-jk_{1z}|z|}}{k_{1z}} \quad (1)$$

in which $k_1 = \omega\sqrt{\mu_1\varepsilon_1}$ is the wavenumber in region 1 and $Z_1 = \sqrt{\mu_1/\varepsilon_1}$ is the intrinsic impedance in the same region. This represents a plane wave traveling along the z direction with a propagation constant of $k_{1z} = \sqrt{k_1^2 - k_\rho^2}$. To consider the reflection of this wave from the dielectric interface it is instructive to decompose it into TE and

TM components and calculate the generalized reflection coefficients of the multi-layer structure for the two components, R_{TE} and R_{TM} [55].

$$\tilde{R}_{i,i+1} = \frac{R_{i,i+1} + \tilde{R}_{i+1,i+2}\, e^{-2jk_{i+1,z}h_{i+1}}}{1 - R_{i,i+1}\tilde{R}_{i+1,i+2}\, e^{-2jk_{i+1,z}h_{i+1}}} \tag{2}$$

where

- k_i is the wavenumber of the *i-th* layer
- h_i is the *i-th* layer thickness
- $R_{i,i+1}$ is the reflection coefficient between the *i-th* and *i+1-th* layer

Specifically, the reflection coefficient for the TE mode is

$$R_{ij}^{TE} = \frac{\mu_j k_{iz} - \mu_i k_{jz}}{\mu_j k_{iz} + \mu_i k_{jz}} \tag{3}$$

and for the TM mode is

$$R_{ij}^{TM} = \frac{\varepsilon_j k_{iz} - \varepsilon_i k_{jz}}{\varepsilon_j k_{iz} + \varepsilon_i k_{jz}} \tag{4}$$

For the TE field, $E_z = 0$, and for the TM field $H_z = 0$, and to accomplish such a decomposition the fields must be expressed in terms of their E_z and H_z components. Since $\frac{\partial}{\partial z} \rightarrow \pm jk_z$ from Maxwell's equations we obtain [51]:

$$\tilde{E}_t(k_x, k_y, k_z) = \frac{1}{k_1^2 - k_{1z}^2}\left[\tilde{\nabla}_t\left(\frac{\partial \tilde{E}_z}{\partial z} + jk_1 Z_1 \hat{z} \times \nabla_t \tilde{H}_z\right)\right] \tag{5}$$

The transforms of the z-components generated by the source alone are found to be:

$$\tilde{E}_z(k_x, k_y, z) = \frac{-jZ_1}{k_1}\tilde{J}_x(k_x, k_y)k_x k_z\left(\frac{-j}{2}\right)\frac{e^{-jk_{1z}|z|}}{k_{1z}} \tag{6}$$

$$\tilde{H}_z(k_x, k_y, z) = -j\tilde{J}_x(k_x, k_y)k_y\left(\frac{-j}{2}\right)\frac{e^{-jk_{1z}|z|}}{k_{1z}} \tag{7}$$

Each of these components gives rise to a reflected field which is given by

$$E_z^r(k_x, k_y, z > 0) = R_{TM}\tilde{E}_z(k_x, k_y, z = 0)e^{-jk_{1z}|z|} \tag{8}$$

$$H_z^r(k_x, k_y, z > 0) = R_{TE}\tilde{H}_z(k_x, k_y, z = 0)e^{-jk_{1z}|z|} \tag{9}$$

where z=0 is the interface between region 1 and the multi-layer medium. By combining (6) to (9) the z-components of the total TM and TE fields above the interface can be expressed as:

$$\tilde{E}_z(k_x, k_y, z > 0) = \frac{-jZ_1}{k_1}\tilde{J}_x(k_x, k_y)k_xk_z(1 - R_{TM})\left(\frac{-j}{2}\right)\frac{e^{-jk_{1z}|z|}}{k_{1z}} \tag{10}$$

$$\tilde{H}_z(k_x, k_y, z) = -j\tilde{J}_x(k_x, k_y)k_y(1 + R_{TE})\left(\frac{-j}{2}\right)\frac{e^{-jk_{1z}|z|}}{k_{1z}} \tag{11}$$

Upon calculating the expressions for the TM and TE spectral components, the fields in terms of spatial variables x, y, z can be derived by evaluating the following inverse Fourier integrals:

$$\boldsymbol{E}_{TM} = -\frac{Z_1}{2k_1}\left(\frac{1}{2\pi}\right)^2 \iint\limits_{-\infty}^{\infty} \left(\left[\frac{\hat{x}k_xk_{1z} + \hat{y}k_yk_{1z}}{k_1^2 - k_{1z}^2}\right] + \hat{z}\right)k_x(1$$
$$- R_{TM})\tilde{J}_x(k_x, k_y)e^{-jk_{1z}z}e^{j(k_xx+k_yy)}\,dk_xdk_y \tag{12}$$

$$\boldsymbol{E}_{TE} = -\frac{k_1Z_1}{2}\left(\frac{1}{2\pi}\right)^2 \iint\limits_{-\infty}^{\infty} \left(\frac{\hat{x}k_y - \hat{y}k_x}{k_1^2 - k_{1z}^2}\right)k_y(1$$
$$+ R_{TE})\tilde{J}_x(k_x, k_y)\frac{e^{-jk_{1z}z}}{k_z}e^{j(k_xx+k_yy)}\,dk_xdk_y \tag{13}$$

The evaluation of the above integrals must take into account any possible integrand poles and branch cuts when the observation point is near or on the surface. The steps followed to obtain E_x^{TE}, which is the dominant component, are indicatively presented below. Similar procedure can be followed for all other components.

$$E_x^{TE}(x, y, z) = -\frac{k_1Z_1}{2}\left(\frac{1}{2\pi}\right)^2 \iint\limits_{-\infty}^{\infty} \frac{k_y^2}{k_1^2 - k_{1z}^2}(1$$
$$+ R_{TE})\tilde{J}_x(k_x, k_y)\frac{e^{-jk_{1z}z}}{k_z}e^{j(k_xx+k_yy)}\,dk_xdk_y \tag{14}$$

$$E_x^{TE}(x,y,z) = \frac{k_1 Z_1}{2}\left(\frac{1}{2\pi}\right)^2 \iint\limits_{-\infty}^{\infty} (jk_y)(jk_y)\frac{1}{k_\rho^2}(1 \\ + R_{TE})\, I_o \frac{e^{-jk_{1z}z}}{k_z} e^{j(k_x x + k_y y)}\, dk_x dk_y \tag{15}$$

where $k_\rho^2 = k_1^2 - k_{1z}^2$. Since both R_{TE} and R_{TM} are functions of k_ρ, the double integral can be reduced to a single integral by invoking the well-known Sommerfeld's and Weyl's identities [51].

$$E_x^{TE}(x,y,z) = k_1 Z_1 \frac{I_0}{8\pi}\frac{\partial^2}{\partial y^2}\int\limits_{-\infty}^{\infty}\frac{1}{k_\rho}(1 + R_{TE})H_0^{(2)}(k_\rho\rho)\frac{e^{-jk_{1z}z}}{k_z}\,dk_\rho \tag{16}$$

where we made the replacement $(jk_y)^2 \to \frac{\partial^2}{\partial y^2}$. Taking into account that:

$$\frac{\partial^2}{\partial y^2}H_0^{(2)}(k_\rho\rho) = -k_\rho\sin\varphi\,\frac{\partial}{\partial y}H_1^{(2)}(k_\rho\rho) \\ = -k_\rho^2\sin^2\varphi\left[H_0^{(2)}(k_\rho\rho) - \frac{1}{k_\rho\rho}H_1^{(2)}(k_\rho\rho)\right] \tag{17}$$

equation (13) can be written as:

$$E_x^{TE}(x,y,z) = -k_1 Z_1 \frac{I_0}{8\pi}\sin^2\varphi\int\limits_{-\infty}^{\infty}k_\rho\left[H_0^{(2)}(k_\rho\rho) \\ -\frac{1}{k_\rho\rho}H_1^{(2)}(k_\rho\rho)\right](1 + R_{TE})\frac{e^{-jk_{1z}z}}{k_z}\,dk_\rho \tag{18}$$

$$E_x^{TE}(x,y,z) = jk_1 Z_1 \frac{I_0}{8\pi}\sin^2\varphi\int\limits_{-\infty}^{\infty}(jk_\rho)\left[H_0^{(2)}(k_\rho\rho) \\ -\frac{1}{k_\rho\rho}H_1^{(2)}(k_\rho\rho)\right](1 + R_{TE})\frac{e^{-jk_{1z}z}}{k_z}\,dk_\rho \tag{19}$$

$$E_x^{TE}(x,y,z) = jk_1 Z_1 \frac{I_0}{8\pi}\sin^2\varphi\frac{\partial}{\partial\rho}\int\limits_{-\infty}^{\infty}\left[H_0^{(2)}(k_\rho\rho) \\ -\frac{1}{k_\rho\rho}H_1^{(2)}(k_\rho\rho)\right](1 + R_{TE})\frac{e^{-jk_{1z}z}}{k_z}\,dk_\rho \tag{20}$$

Also, considering that:

$$\frac{\partial}{\partial\rho}\left[H_0^{(2)}(k_\rho\rho) - \frac{1}{k_\rho\rho}H_1^{(2)}(k_\rho\rho)\right]$$
$$= -\frac{1}{\rho}H_0^{(2)}(k_\rho\rho) + \left(\frac{2}{k_\rho\rho^2} - k_\rho\right)H_1^{(2)}(k_\rho\rho) \tag{21}$$

(17) can be written as:

$$E_x^{TE}(x,y,z) = jk_1 Z_1 \frac{I_0}{8\pi}\sin^2\varphi \int_{-\infty}^{\infty}\left[-\frac{1}{\rho}H_0^{(2)}(k_\rho\rho)\right.$$
$$\left. + \left(\frac{2}{k_\rho\rho^2} - k_\rho\right)H_1^{(2)}(k_\rho\rho)\right](1 + R_{TE})\frac{e^{-jk_{1z}z}}{k_z}dk_\rho \tag{22}$$

which is the only the field component parallel to the used dipole orientation.

As is well known, direct numerical computation of the Sommerfeld's integral is time-consuming and computationally expensive. This is due to the oscillatory and slowly decaying nature of the integrands, especially whenever the source and observation points are on the same interface [52]-[53]. Indeed, several techniques have been proposed in the literature to numerically evaluate Sommerfeld's integral.

Similarly to [51]-[55], we invoke Cauchy's theorem to deform the original path of integration off the real axis (Fig. 3.3) and avoid difficulties associated with integrand singularities along the real axis of integration [51]-[54]. Specifically, we decided to split the integration path γ in to three paths, $\gamma_1 = (-\infty - ja, a - ja)$, $\gamma_2 = (a - ja, a + ja)$ and $\gamma_3 = (a + ja, \infty + ja)$, where a is chosen equal to $0.8k_0$.
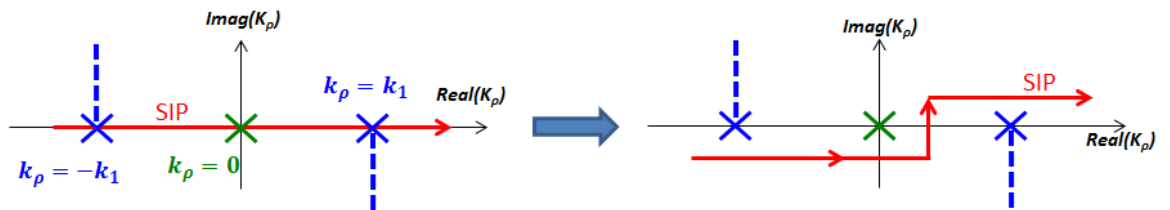
Fig. 3.3. - Initial Sommerfeld Integration Path (SIP) on the real axis of the complex k_ρ plane (a) and deformed SIP to avoid singularities and branch cuts (b)

A MATLAB code was developed to obtain the total electric field on the interface of the stratified medium with the ambient region. To verify the calculations, the code was used to compute the total electric field radiated from an infinitesimal dipole in free space and the results were compared with the theoretical equations as described in [56]. As depicted in Figure 3, good agreement is observed between the two curves. The calculated generalized reflection coefficients for TM and TE fields were also verified using examples included in [56].
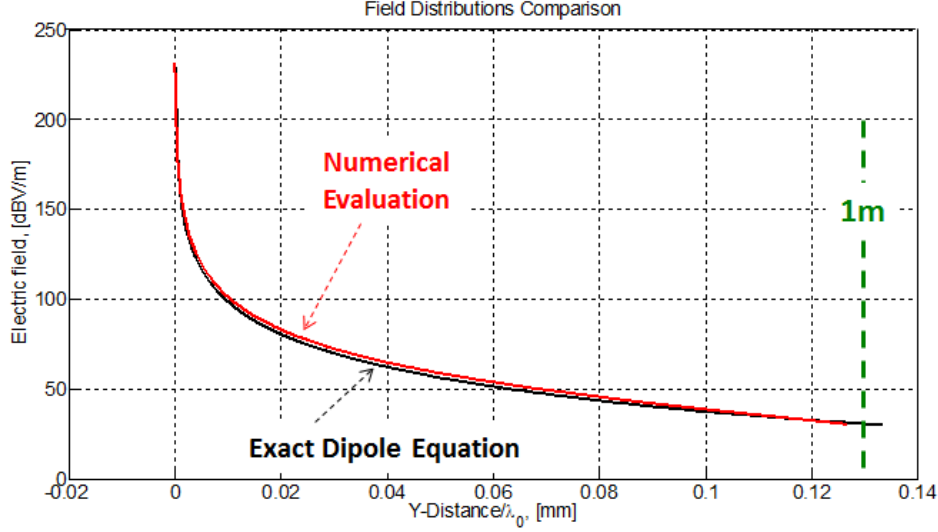
Fig. 3.4. - Radiated fields from an infinitesimal dipole in free space calculated with implemented numerical evaluation (red curve) and from [56] (black curve).

3.4   Dielectric permittivity estimation method

Doing so, the fields can be computed on the interface and used to estimate the inner layer dielectric constant. Having the fields at the original probe locations, and given that $S_{i,1}$ is proportional to the computed *x*-directed electric field denoted as $E_{i,1}$, we proceed to express ε_r as

$$\varepsilon_r = \sum_{i=2}^{M} w_i E_{i+1,1} \tag{23}$$

Specifically,

$$[\varepsilon_r]_{1 \times N} = [w]_{1 \times M} [E]_{M \times N} \tag{24}$$

Here, $[\varepsilon_r]$ is the vector representing the "known" dielectric constant at the chosen depth for each of the N simulated combinations of other layers parameters, $[w]$ is the matrix containing the coefficients to be determined, M is the number of points where the electric field is computed or probed, and $[E]$ contains the calculated surface electric field values. As in [46], since N>>M, (23) is solved via the least squares method to obtain $[w]$.

The accuracy of (23) will likely depend on the:

1. Number, N, of random simulated combinations used to populate the $[E]_{M \times N}$ matrix in (24), and

2. sensor length, and

3. distance between sampling points.

As in [46], we chose to generate the system (24) using the parameter variations in Table I for each layer. Below we discuss the accuracy of (24) for predicting the dielectric constant of deep layers representing the lung.

TABLE I
NOMINAL VALUES AND VARIATION RANGE OF THE TISSUE ELECTRICAL PROPERTIES AND THICKNESSES [57]

Tissue	Dielectric Constant (ε_r)	Loss tangent ($tan\delta$)	Thickness (h) [cm]
Skin	$93.73 \pm 10\%$	$2.17 \pm 10\%$	$0.3 \pm 10\%$
Fat	$7.33 \pm 10\%$	$2.09 \pm 10\%$	$1.5 \pm 10\%$
Muscle	$82.57 \pm 10\%$	$3.64 \pm 10\%$	$1.5 \pm 10\%$
Bone	$26 \pm 10\%$	$1.55 \pm 10\%$	$2.0 \pm 10\%$
Lung	$65 \pm 40\%$	$2.65 \pm 20\%$	$15 \pm 20\%$

3.5   Numerical Results

The accuracy of the proposed deep tissue dielectric constant extraction method was evaluated as a function of: (a) the sensor length, (b) the number of points where the electric field was probed, viz. number of field measurements points, and (c) the number of equations, N, used to populate the matrix {E} in (24). Two scenarios were considered, shown in Fig. 3.5. In one case, the torso model included 3 outer layers (skin, fat, and muscle) (see Fig. 3.5(a)). Of course, the proposed deep tissue monitoring method must be able to provide accurate results for any arbitrary number of tissue layers and sensing depths. Therefore, to demonstrate the versatility of this method, we also considered a torso model with 4 outer layers (skin, fat, muscle, and bone). The latter scenario is depicted in Fig. 3.5(b).

(a)   (b)
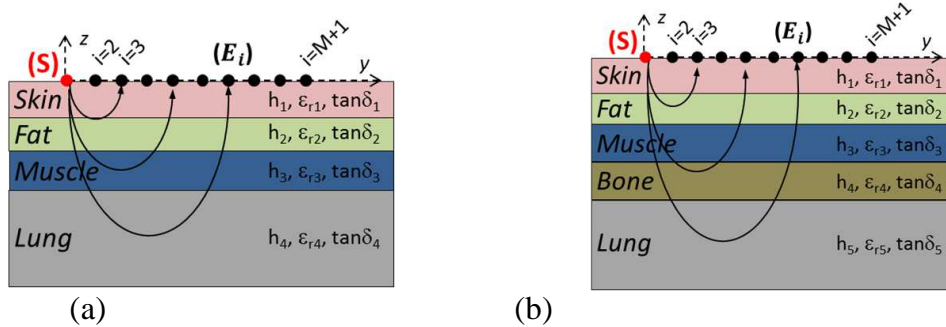
Fig. 3.5. - Human torso equivalent model taking into account (a) three and (b) four outer layers. Electric field propagation inside the medium is also sketched.

To calculate the weight coefficients (w_i), we considered the parameter variations shown in Table I for each layer, leading to N=2000 equations. After obtaining w_i, the average error of the approximation (24) was then obtained using different and random combinations of the top 3-4 layers. Specifically, we averaged the errors computed over 1000 random combinations of tissue electrical properties and thicknesses.

Fig. 3.6 and Fig. 3.7 show the average error in estimating the lung's dielectric constant for the scenarios depicted in Fig. 3.5 (a) and Fig. 3.5 (b), respectively.

(a)

(b)

(c)
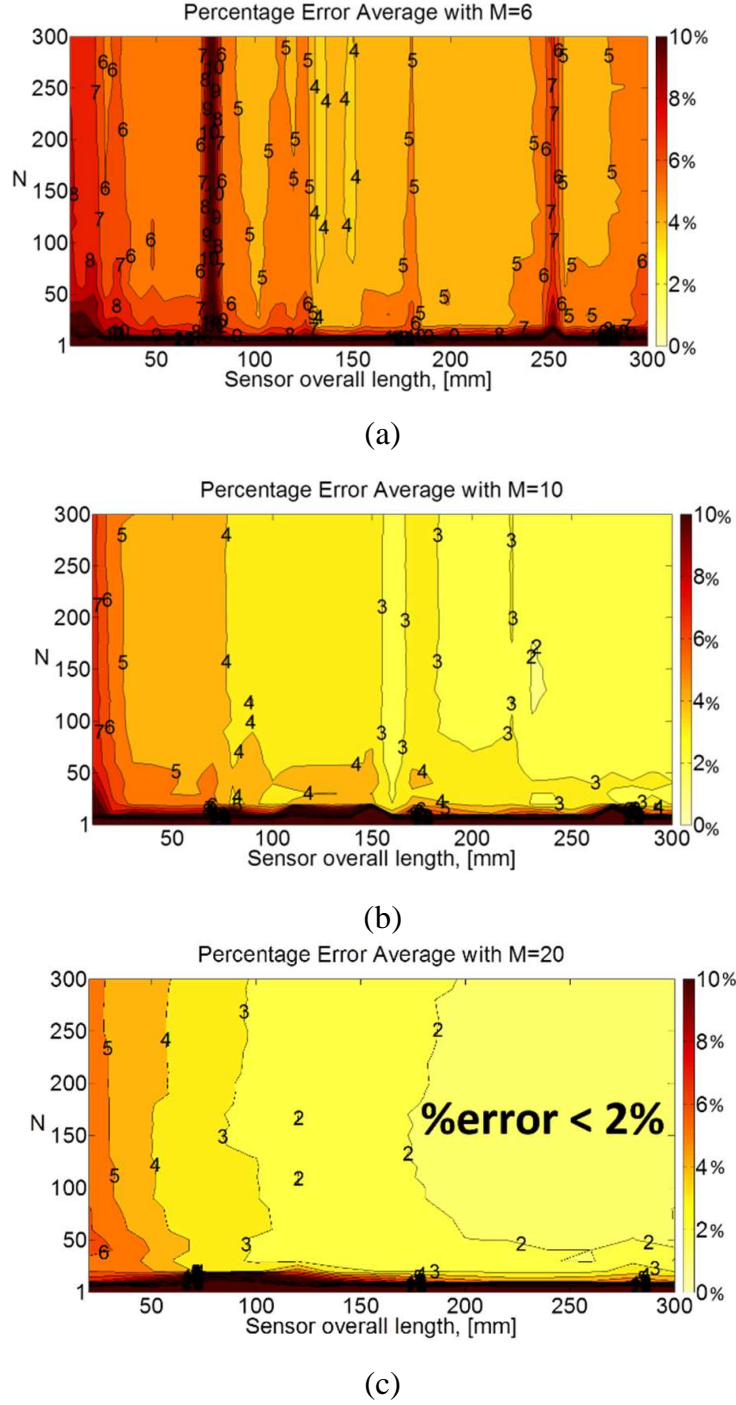
Fig. 3.6. - Average percentage error in estimating ε_{r4} (see Fig. 3(a)) when the sensor includes: (a) M=6 probes, (b) M=10 probes, and (c) M=20 probes.

A different set of weight coefficients (w_i) was computed and used for these two scenarios for several sampling points or probe number, M. Three different values of M were considered, M=6, 10, and 20. The error for each of these M values was plotted in Fig. 3.6-Fig. 3.7 for different number of equations, N. Specifically, the vertical axis of Fig. 3.6and Fig. 3.7 refers to the number (N) of equations used to determine the w_i coefficients and the horizontal axis is the overall sensor length for M=6, 10 and 20. As indicated to the right of the plots, deep red colors imply large errors (8-10%), whereas

light yellow refers to low errors (<2%).

From the results in Fig. 3.6 and Fig. 3.7, we can extract the following guidelines for sensor design optimization:

- the electric field must be recorded across a sensing area that spans at least 20cm from the source point;
- for a given sensor length, a larger number of probing points leads to greater accuracy;
- increased accuracy is achieved as the number of equations used to solve for w_i is higher .

Remarkably, for the scenario of Fig. 3.5(a), an average error of less than 2% may be achieved by: (a) using at least 10 probes or field sampling points, (b) distribution of the probes should be over a length at least 18-20cm, and (c) at least N=100 equations are needed to compute the coefficients w_i. For the scenario in Fig. 3.5 (b), an average error less than 3% is achieved by: (a) using at least 20 probes, (b) distributing the probes across a length of at least 20cm, and (c) considering at least 100 equations to compute the coefficients w_i. The two scenarios provide consistent results for achieving an accuracy of 2-3% in extracting the lung's ε_r. As would be expected, the accuracy of our expression (6) is lower for the case in Fig. 3.5 (b), compared to that of Fig. 3.5 (a).

(a)

(b)

(c)
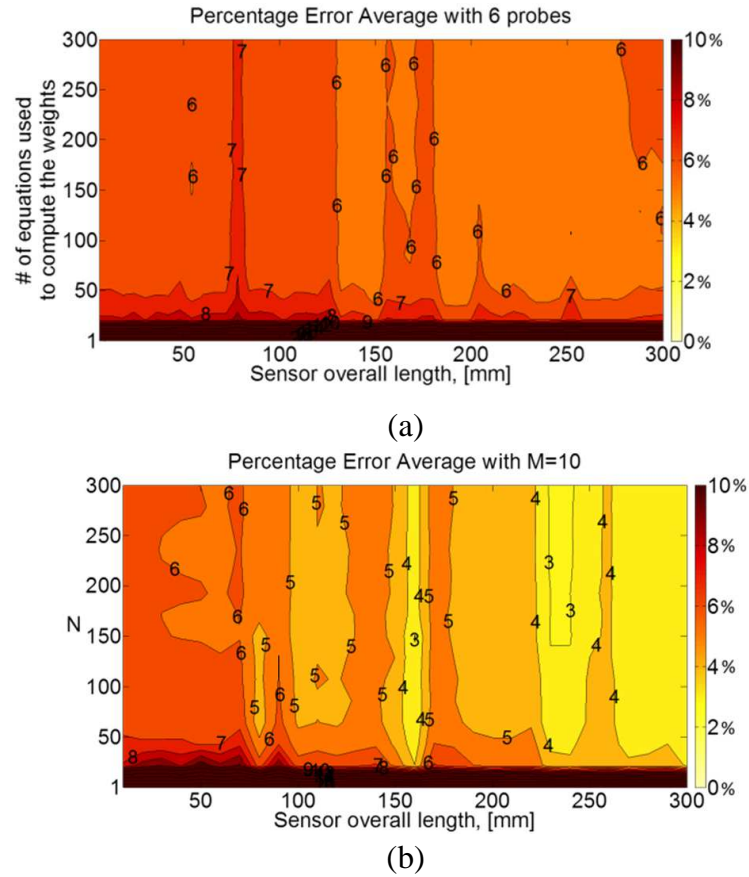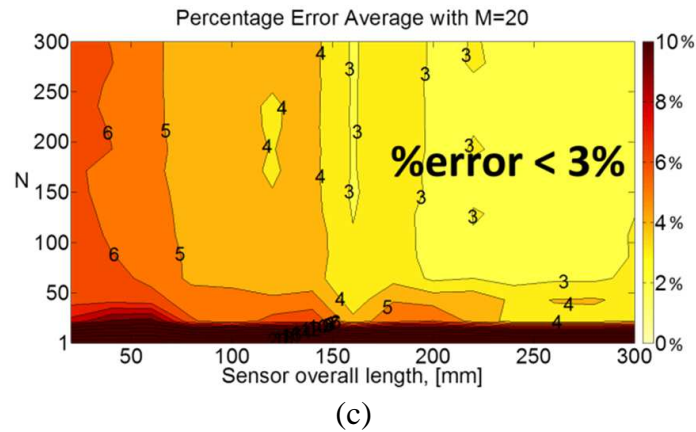
Fig. 3.7. - Average percentage error in estimating ε_{r5} (see Fig. 3(b)) when the sensor includes: (a) M=6 probes, (b) M=10 probes, and (c) M=20 probes.

3.6 Conclusion

A theoretical analysis was presented to assess the accuracy of a novel method for extracting the dielectric constant, ε_r, of deep human tissue. To do so, the human torso was modeled as a stratified dielectric medium and the electric field distribution on its surface was computed using a custom numerical code. A key aspect of the extraction method was the representation of ε_r as a linear combination of the surface electric field samples. The Chapter presented guidelines for sensor design optimization. It was concluded that the deep tissue's dielectric constant can be estimated with errors lower than 3%, at almost any arbitrary depth.

4   Integration of Slot Antennas in Commercial Photovoltaic Panels for Stand-Alone Communication

4.1   Introduction

AUTONOMOUS communication systems often use photovoltaic (PV) panels that are physically separated from the antenna, and this demands for a compromise in the utilization of the available space. Moreover, in several applications, as for example monitoring, vehicular communication and satellite systems, distinct PV panel and antenna may be anti-aesthetic, expensive and causes engineering issues. For above reasons, antenna integration in large PV panels is desirable and it has become a research topic. Designing the antennas such that they can be easily integrated in a commercial PV panel without modifying the panel geometry (after-market integration) can result in a low-cost implementation of additional functions in a solar PV field. For example, a low-data rate wireless communication system could be implemented for the remote control and monitoring of PV panels in large solar fields. In this context, low cost antennas with proper polarization and pattern characteristics are needed to improve panel-to-panel radio links or maximize a tunnel-propagation effect (Fig. 4.1). Most recent solutions for antennas integrated in PV panels are those based on the innovative transparent antennas [58]-[60], or patch [61]-[71] and slot [71]-[70] antennas.
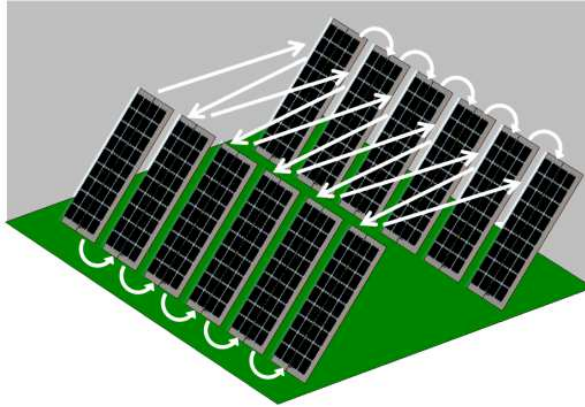
Fig. 4.1. - A simplified scheme of a solar PV field where a wireless communication link can be used for remote control and monitoring functions.

Transparent materials have been proposed to implement innovative transparent antennas, as they can be easily mounted on solar cells. Transparent antennas have been optimized for different applications, at 3.4-3.8GHz [58] and 2.5GHz [59] frequency bands. Nevertheless these materials are still relatively expensive. Besides, meshed patch antennas printed on the top of PV cells are considered a cost-friendly solution. An example of such antennas, optimized for a 2.52GHz small satellite application, is described in [60]. However, a 90% sunlight transparency needed for the proper functioning of the solar cell [60] cannot be easily achieved.

Solar cells have been employed themselves as a radiating patch [61] or as a coupled patch [62]-[64], for GPS vehicular applications, GSM bands or 3.76 GHz satellite communications. In such cases the cell dimensions are strictly related to the operating frequency, and this limits the possible applications for PV panels made of cells with standardized cells. Solar cells may also be used as a ground plane for an upper patch element [65]-[67], but with a reduction of the PV solar efficiency.

Slot antennas placed between solar cells have been optimized for high frequency applications [68], or by requiring modifications of the DC bus wires [69]. Alternatively, slots have been realized by properly etching of them [70]-[71] into the solar cell, but reducing the cell solar efficiency.

In this Chapter, two configurations of low-cost slot antennas suitable for their integration in a class of commercial large PV panels are described. As test cases, two antennas operating at the GSM/UMTS and WiMAX frequency bands have been designed to show the achievable performance in terms of compactness and percentage impedance bandwidth. A considerable reduction of the antenna physical size was obtained exploiting the presence of the cover glass layer that is always present in commercial PV panels. Measurements on antenna prototypes attached to real PV panels have been used for a fine tuning of the antennas, so avoiding detailed numerical models that would result in complex models but not able to account for the several propagation phenomena involved in the periodic/multilayer structure of a PV panel. Indeed, the effects on antenna performance of the cells close to the slot, as well as of the DC bus wires and panel aluminum frame cannot effectively accounted for by numerical models (dielectric permittivity values of the PV cell material at the UHF and microwave frequencies are also difficult to find).

4.2   Slot antenna design

The antenna integration concept here proposed is based on the exploitation of the room available between adjacent solar cells of some large PV panels, so without decreasing the panel solar efficiency. In particular, two cell arrangements often used in large PV panels are considered, and they are shown in Fig. 4.2.
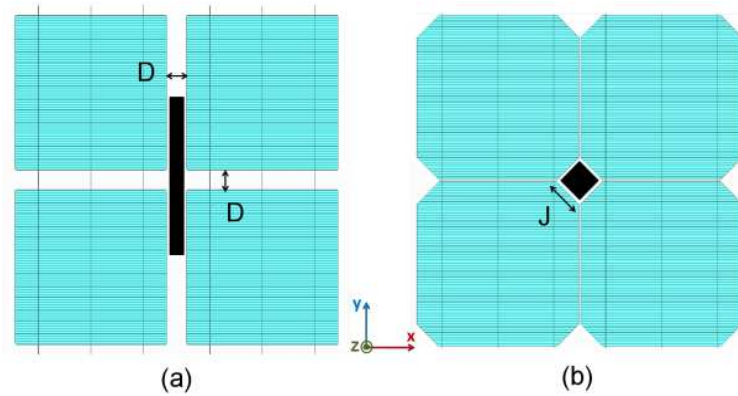
Fig. 4.2. - Two typical arrangements for PV cells in large panels: (a) square cells separated by a distance D; (b) octagonal cells close to each other, with an uncovered square-shape space whose side length is denoted by J. Possible locations for slot antennas are also shown (with dark color), which are such that the slot aperture is not crossed by the DC voltage bus wires.

For such configurations, a linear or square slot antenna etched on a low-cost substrate can be attached just on the back side of the panel and located in such a way that the slot aperture is not obstructed by the cells (which basically behave like shielding conductive surfaces). Also, the DC voltage bus wires have not to cross the slot aperture, as it would result in an antenna shorting effect. For example, this means that in the cell arrangement shown in Fig. 4.2a, gaps parallel to the x-axis are not functional because of the presence of the DC voltage bus wires; on the other hand, more room is available along the y-axis (it being only limited by the panel frame size), so allowing either the allocation of some long linear slots (resonating at low frequencies) or the allocation of linear arrays made of shorter linear slots (higher resonance frequencies) to implement high-directivity arrays or a number of low-directivity arrays operating at different frequency bands (electronic beam scanning can also be implemented through a proper feeding network).

To better understand how to make use of the above linear or square gaps, the stack-up of two typical PV panels are shown in Fig. 4.3. Silicon or GaAs (Gallium Arsenide) solar cells are usually incorporated between two ethylene vinyl acetate (EVA) layers. Also, two cover glass layers are placed at the top and bottom sides of the PV panel. In some commercial panels, the bottom cover glass layer can be replaced by a plastic backsheet, as a Tedlar® film (Fig. 4.3b).
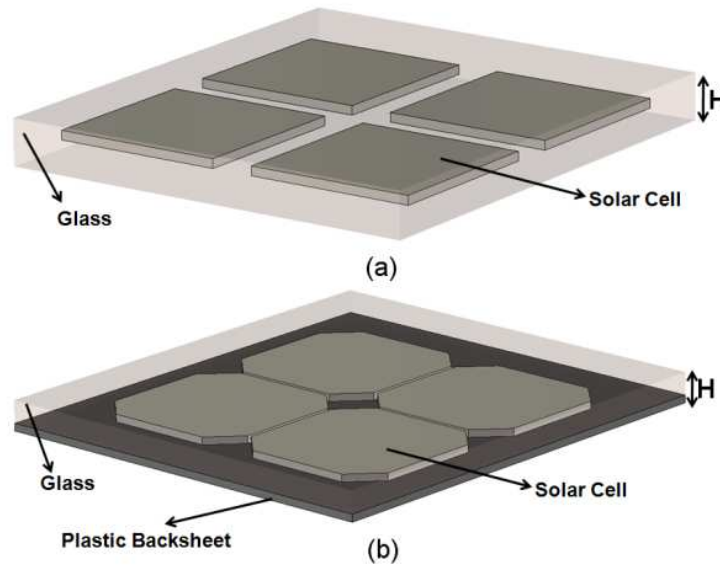
Fig. 4.3. - Stack-up of two typical commercial photovoltaic panels: (a) a glass- cells-glass PV panel, with square solar cells and (b) a glass-cells-Tedlar® PV panel with octagonal solar cells. In both PV panel configurations, the solar cells matrices are encapsulated between two EVA layers.

Therefore, a slot antenna positioned according to the two above mentioned criteria, could be enclosed by cover glass and EVA layers. Both layers are low-loss dielectrics and their effect can be accounted for during the design process. EVA layer is relatively thin (usually less than 0.1mm) and its effect can be neglected up to some Gigahertz. The glass layer is thicker, going from a few mm up to 10 mm when both a top and a bottom cover glass layer are present (see Fig. 4.3a). Notably, the glass layer of the PV panel that will appear to be positioned on the top of the slot helps in reducing slot resonance frequency [72], so giving rise to an extremely advantageous antenna miniaturization effect (without requiring any antenna meandering or distributed reactive loading, or any other complex configuration).

As test cases for the proposed design approach, a linear slot antenna and a square slot antenna have been designed and prototyped, to fit in commercial PV panel topologies like those in Fig. 4.3a and Fig. 4.3b, respectively. Fig. 4.4 shows the top view of the two proposed antennas: a three-stepped slot antenna (*TSSA*) [73] and a square slot antenna (*SSA*) [74]. Both slots are realized on a 1.6mm thick FR4 substrate (ε_r=4.4, tgδ=0.02); a CPW and a microstrip are used to feed the TSSA and SSA, respectively (both with a 50-Ω characteristic impedance). The three-stepped slot configuration has been chosen to check the best performance that can be achieved in term of percentage impedance bandwidth, in the framework of slot antennas whose maximum width is limited by the presence of nearby PV cells separated by a given distance D. Specifically, it is shown that the antenna can operate in frequency bands that allocate both GSM (1710 – 1910 MHz) and UMTS (1920 –2170MHz) applications (around 24% percentage bandwidth). The three-stepped slot is etched on the same side of the CPW feeding line. The main parameters related to the resonant frequency and to the bandwidth of *TSSA* are the slot

length (*L*) and width (*W*), respectively. An antenna impedance fine tuning on a wide frequency bandwidth can be achieved by varying the lengths *A*, *B* and *C*.
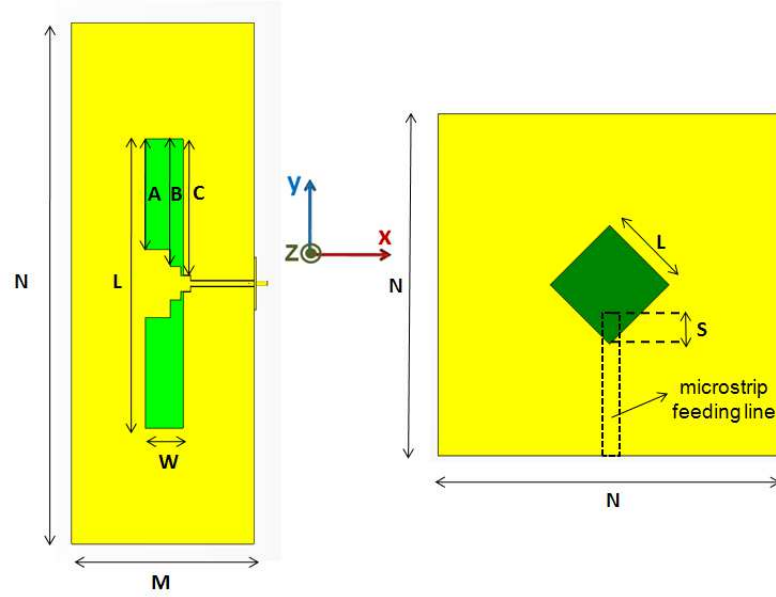
Fig. 4.4. - Layout of the proposed slot antennas suitable to be integrated in a typical PV panel: (a) three-stepped slot antenna, TSSA; (b) square slot antenna, SSA.

In the *SSA*, the microstrip feeding line is in the opposite side with respect to the square slot. As in other square slot configurations, the length of the open-circuit stub (*S*) behind the slot is optimized for input impedance tuning. The S*SA* has been designed to operate at higher frequencies, in the WiMAX 3300–3800MHz frequency band, as it represents the lower frequency band that can be covered when the side of the square space available at the corner of octagonal cells is less than 30mm (and a cover glass layer of less than 4mm is considered).

The numerical simulations were performed using the commercial software CST MWS®. Simulation results on the miniaturization effect due to the PV panel cover glass layer are discussed in Paragraph 4.2.1. The effects of the solar PV cells close to the antenna have been numerically checked by adding square or octagonal metallic patches positioned nearby the slots, between the slot plane and the glass layer (Paragraph 4.2.2). Finally, the influence of a reflector behind the whole structure (needed if an unidirectional beam is required) is analyzed in Paragraph 4.2.3.

4.2.1   Miniaturization effect due to the cover glass layer

A simplified model of the PV cell multilayer structure has been adopted during the numerical design process (Fig. 4.5). Indeed, only a glass layer (εr =4.82, tgδ=0.0054) has been considered.

The TSSA and SSA have been optimized by considering for the cover glass layer a thickness *G* equal to 8mm and 4mm, respectively. These values come from the

corresponding value of the cover glass layer of the two commercial photovoltaic panels that have been used for the measurements. The geometrical parameters of the two optimized slot antennas are listed in Table I.
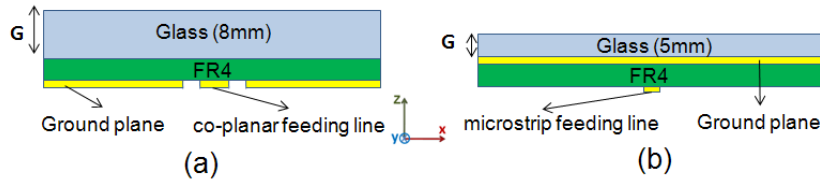
Fig. 4.5. - Stack-up of the proposed slot antennas suitable to be integrated in two typical PV panels: (a) TSSA and (b) SSA. The cover glass layer on the top is the only layer of the PV cell that has been considered in the numerical model used for the slot antenna design.

TABLE I
ANTENNA DIMENSIONS OPTIMIZED WITH COVER GLASS LAYER (MM)

TSSA				SSA	
N	200	A	35.2	L	19.5
M	70	B	40.7	N	140
L	92.4	C	43.5	S	11.4
W	13				

The *TSSA* and *SSA* fit an overall volume of $200{\times}70{\times}1.6$ mm^3 and $140{\times}140{\times}1.6$ mm^3, respectively. The *TSSA* slot is 92.4mm long (*L*) and 13mm wide (*W*). The square slot exhibits an area of about 19.5×19.5 mm^2, with a *S* =12.3mm stub. Fig. 4.6 shows the reflection coefficient of the two antennas.
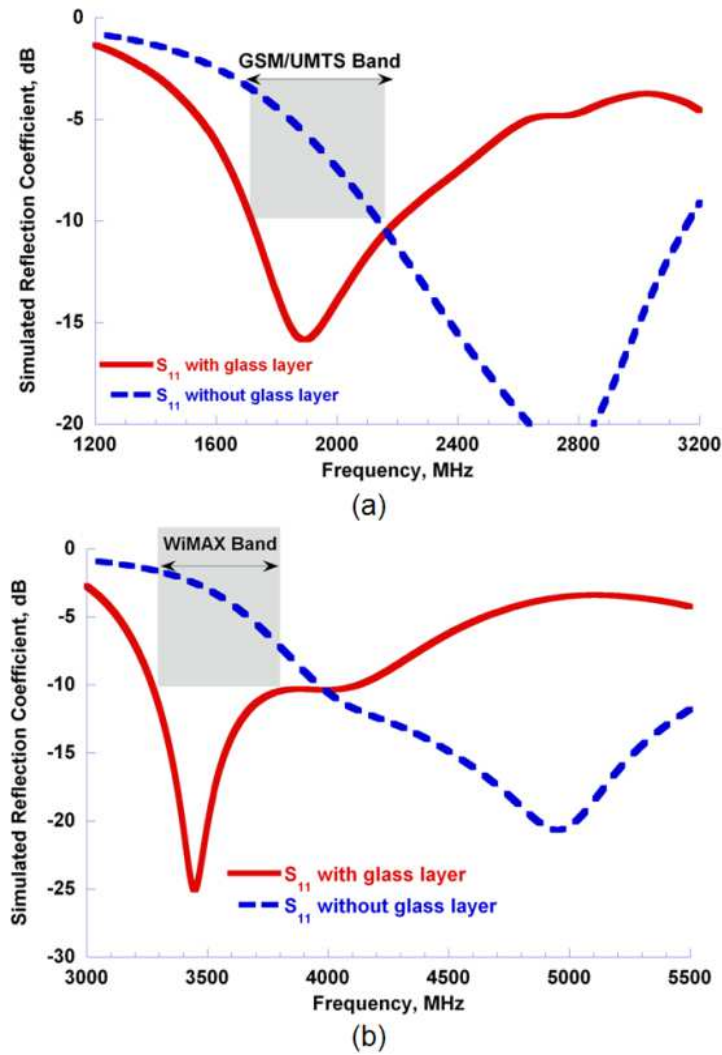
Fig. 4.6. - Simulated reflection coefficient for the slot antennas: (a) TSSA and (b) SSA. A reference curve showing the reflection coefficient when the cover glass layer is removed.

To give evidence to the miniaturization effect, in the same figure the reflection coefficient for an identical slot antenna without the glass layer is shown. It has been numerically estimated that the presence of the cover layer leads to a quite important miniaturization level: 36% for the *TSSA* and 25% for the *SSA*. It has been also verified that *TSSA* and *RSA* antenna gain are stable in the frequency band of interest, as shown in Fig. 4.7.
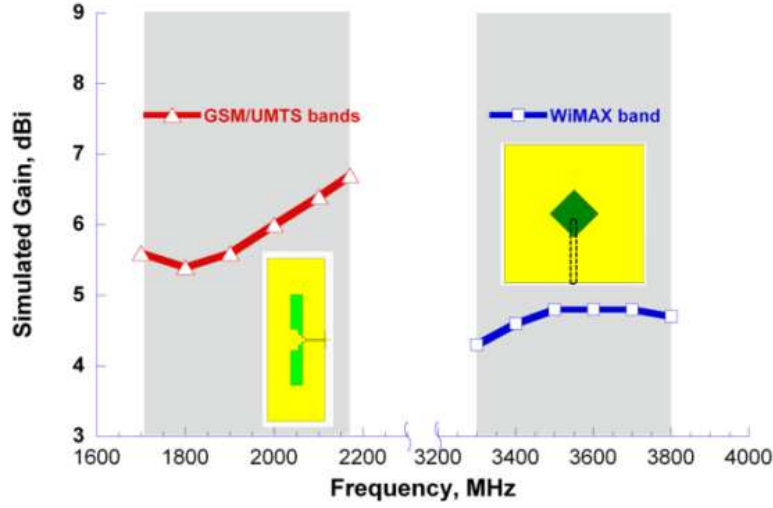
Fig. 4.7. - Simulated gain for the proposed TSSA and SSA in the GSM/UMTS and WiMAX bands, respectively.

4.2.2   Numerical analysis of the effect of the PV cells located nearby the slot

The effects of the solar PV cells close to the antenna have been numerically checked by adding square or octagonal metallic patches positioned nearby the slots, in the middle of the glass layers (Fig. 4.8). The 1-mm-thick plastic backsheet effect in the PV panel of Fig. 4.8b can be neglected in the numerical simulation.
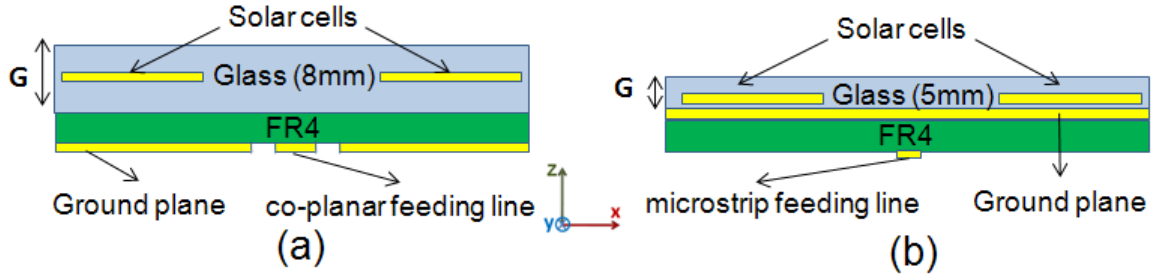
Fig. 4.8. - Stack-up of the proposed slot antennas suitable to be integrated in two typical PV panels, for (a) the TSSA and (b) the SSA. The cover glass layer on the top is the only layer of the PV cell that has been considered in the numerical model used for the slot design, while simple metallic patches have been used to model the PV cells.

Fig. 4.9a shows the reflection coefficient behavior of the TSSA, by varying the distance D between the PV cells from 10mm up to 50mm. It is noted that when the distance between two solar cells is smaller than the *TSSA* slot width (*W*=13mm), there is a significant impedance mismatching, as expected since the slot is partially covered by the PV cell.

Numerical results for the SSA are shown in Fig. 4.9b. It results that for a slot side of 19.5mm, the distance between nearby octagonal PV cells (Fig. 4.2b) should be enough large to allow that the side of the square space in Fig. 2b, *J*, is at least greater than

26mm. The presence of the solar cells determines a slight mismatching and a 100MHz shift toward lower frequencies (this shift can be compensated through a small reduction of the square slot side, *L*).
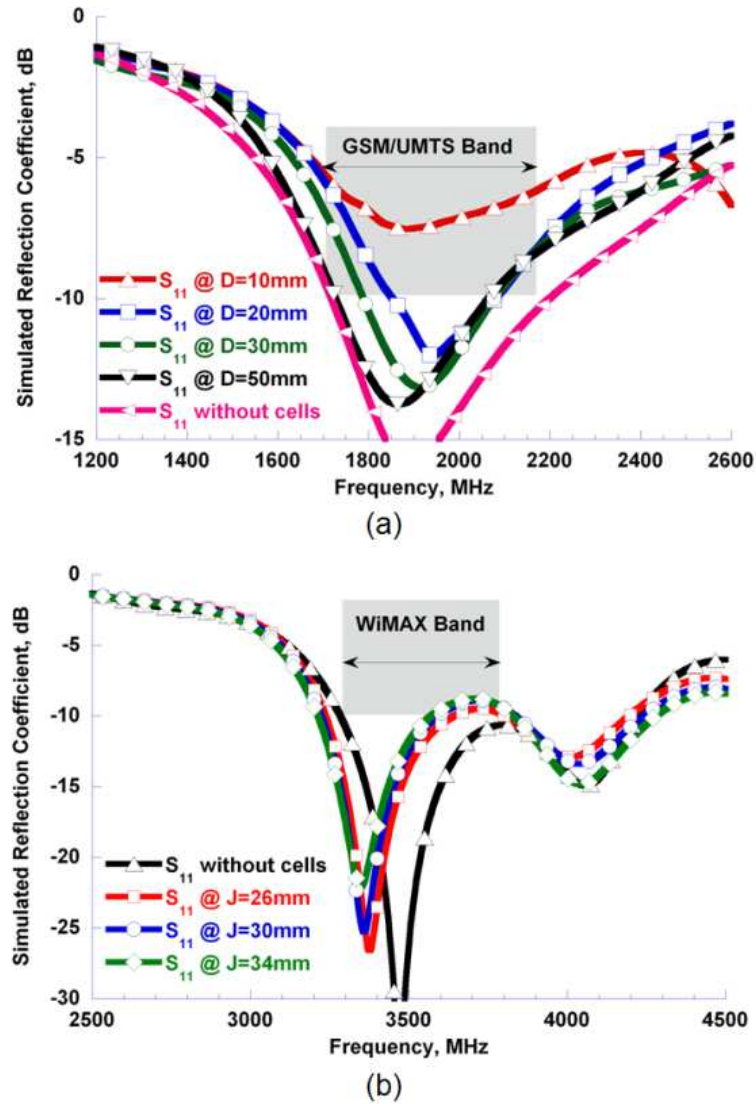
Fig. 4.9. - Simulated reflection coefficient for the slot antennas, as a function of the size of the room available between adjacent cells (parameters D and J in Fig. 4.2). PV cells have been modeled trough simple metallic patches: (a) TSSA and (b) SSA. As a reference, a curve has been added for the simpler cell model where only the glass layer is present.

4.2.3   A metallic reflector to get an unidirectional radiation pattern: its effect on the antenna input impedance

An aluminum reflector placed at a distance *R* from the bottom side of the FR4 substrate (Fig. 4.10) can be used to achieve unidirectional radiation at broadside and increase the antenna gain.
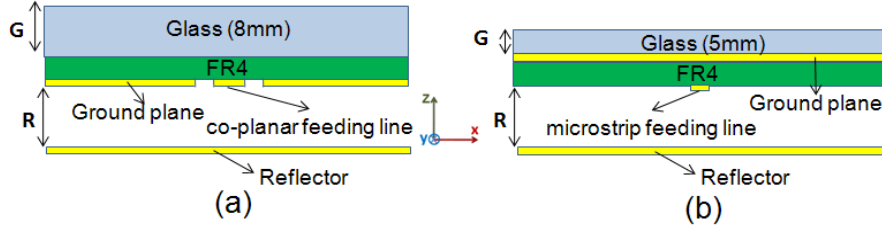
Fig. 4.10. - Stack-up of the (a) TSSA and (b) SSA with a 250mm-side square reflector plane. Its presence ensures a low back radiation and an improvement of the antenna gain.

The effect on the reflection coefficient of a 250mm-side aluminum square reflector is shown in Fig. 4.11 for different distances *R*. The presence of the reflector results in a slight impedance mismatching that can be compensated by varying the main parameters of the two antenna configurations. For *R*=30mm, antenna gain increases up to about 8dBi and 7dBi for the TSSA and SSA, respectively. The radiation patterns in the principal planes (E$_\theta$ and E$_\varphi$ components), evaluated at the center frequencies of the bands of interest, are shown in Fig. 4.12. A back lobe amplitude less than -13dB is achieved for both antennas. The two slots antennas (both they are linearly polarized antennas) exhibit a cross-polar component levels below -18dB.
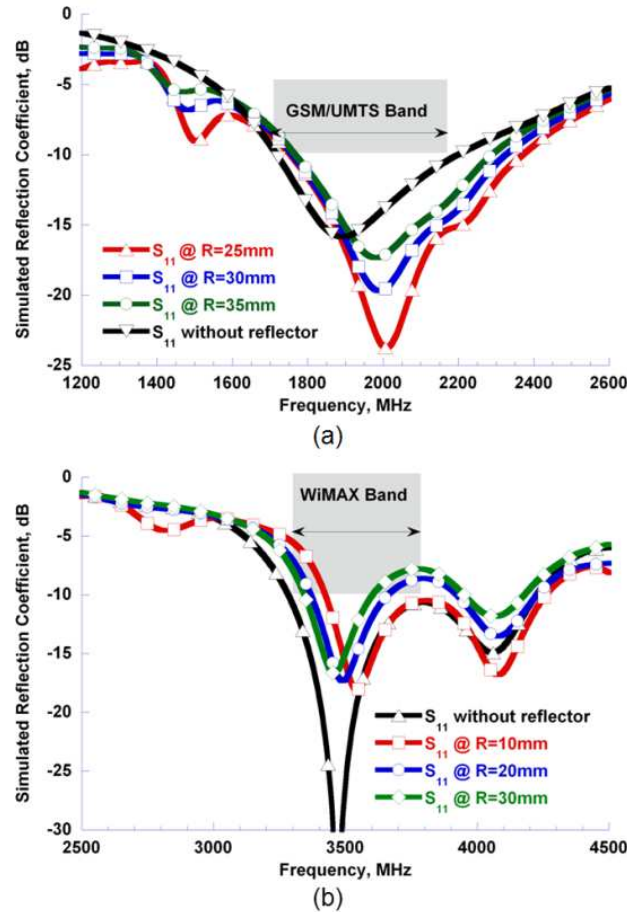
Fig. 4.11. - Simulated reflection coefficient of the slot antennas versus the distance R between the FR4 bottom and a metallic reflector: (a) TSSA and (b) SSA. The reference curve shows the antenna reflection coefficient when the reflector is absent.
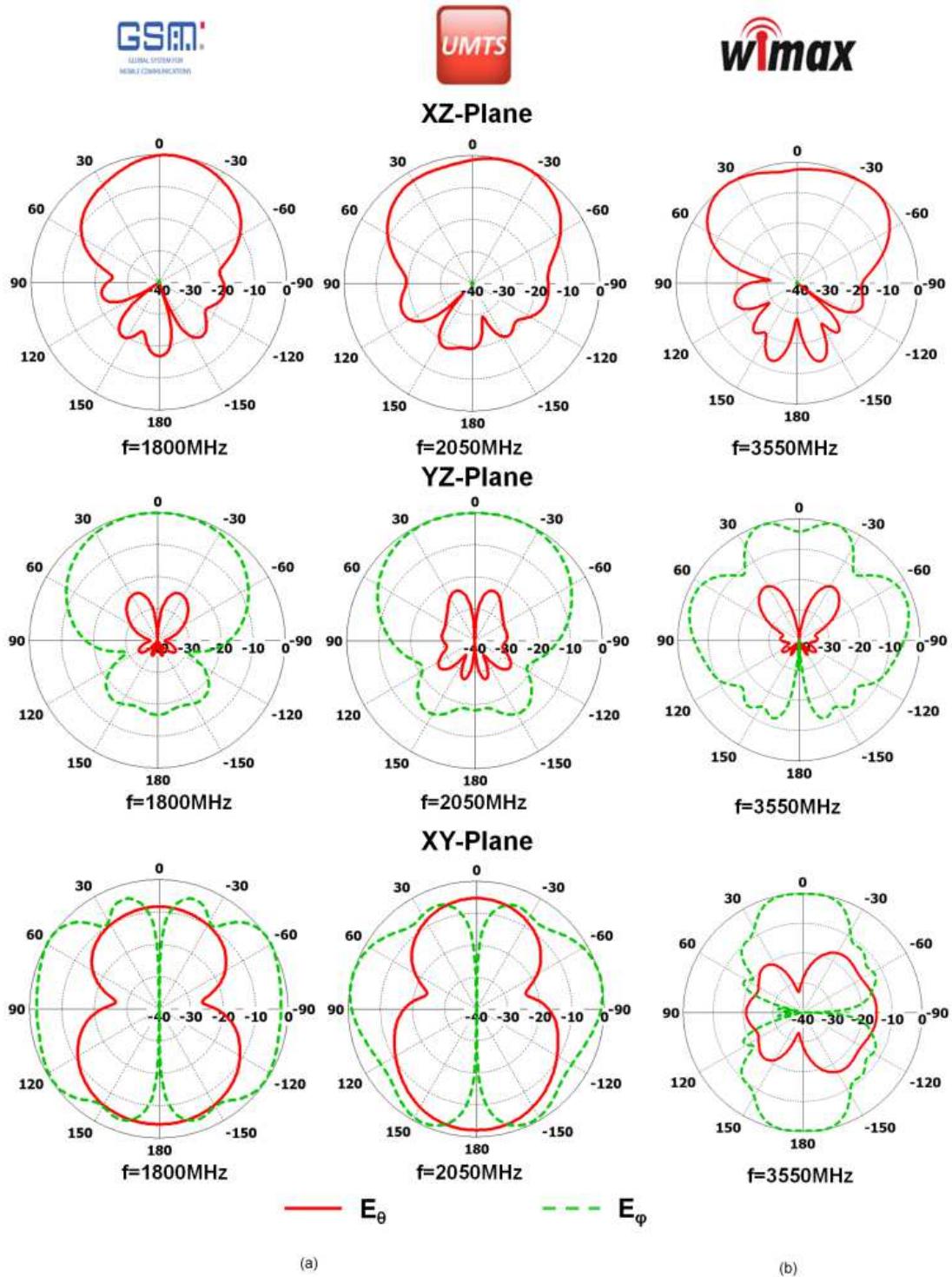
Fig. 4.12. - Normalized radiation patterns in the principal planes at GSM and UMTS centre frequencies for the TSSA, and at WiMAX centre frequency for the SSA. A metallic reflector is placed at a distance R from the FR4 bottom: R=30mm for the TSSA, and R=20mm for the SSA.

4.3   Experimental results

Fig. 4.13 shows the *TSSA* and *SSA* prototypes. Two different commercial PV panels, corresponding to the cell arrangements in Fig. 2, have been used to estimate antenna performance when it is attached on a real PV panel.

(a)   (b)
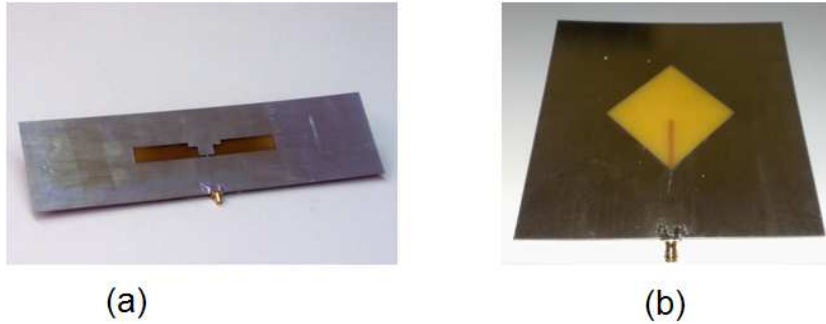
Fig. 4.13. - TSSA (a) and SSA (b) prototypes realized on a 1.6mm-thick FR4 substrate.

4.3.1   Measurements results for the TSSA prototype

A 140-W-BRP6336064-140 PV panel [75] was employed to check the TSSA input impedance for different locations of the antenna with respect to the panel surface. The panel consists of 36 high-quality polycrystalline silicon square solar cells (156×156 mm^2); the aluminum panel frame is 1655x991mm^2 and its thickness is 40mm. The total thickness of the top and bottom cover glass layers is 8mm, that guarantees a good light permeability and protects solar cells from atmospheric agents. In the standard BRP6336064-140 panel the distance D between the PV cells is set to 25mm. A panel with four columns at different distances (D=20, 30 and 50mm) was specifically manufactured, to measure the effect of the cell proximity on the antenna reflection coefficient. The distance between cells along the vertical direction is set to 25mm.
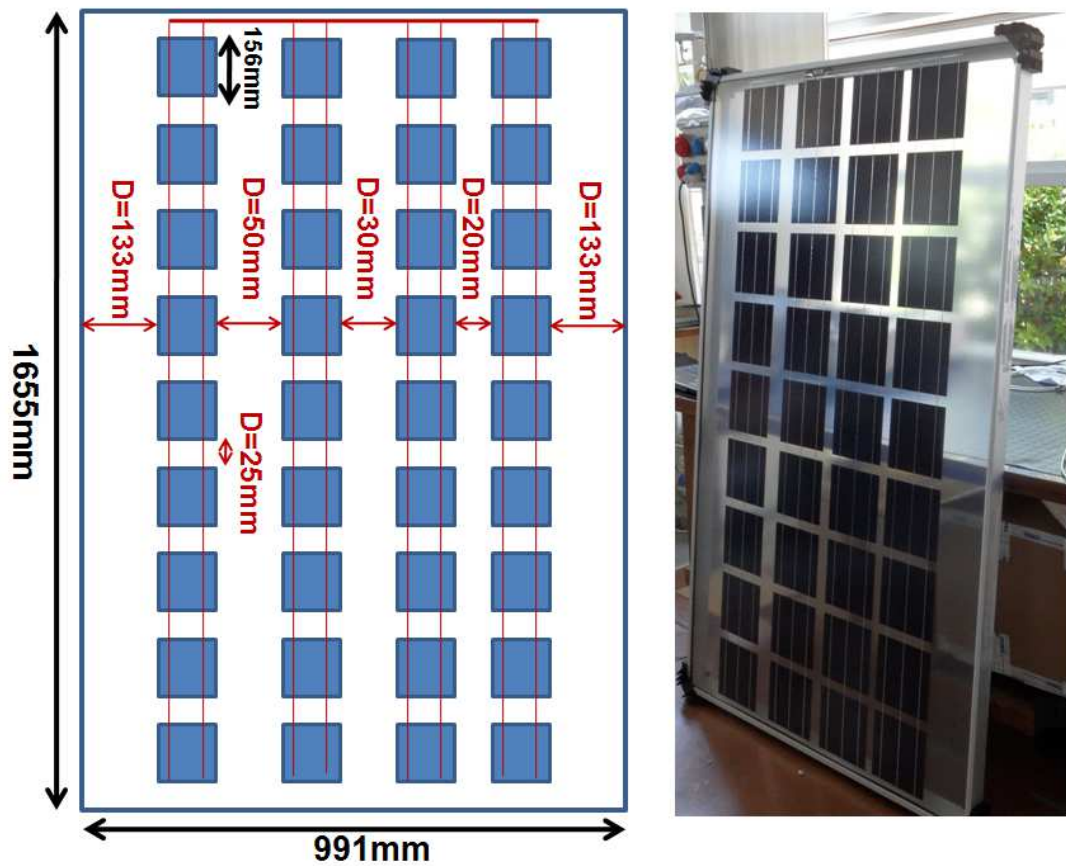
Fig. 4.14. - The BRP6336064-140 PV panel used for testing the TSSA. The panel is made of four columns at different distance: D=20, 30 and 50mm. The distance between cells along the vertical direction is set to 25mm.

Measured values of *TSSA* reflection coefficient are plotted in Fig. 4.15, for the isolated antenna (without the glass layer) and when the antenna is attached on the back of the PV panel, at the 133mm-wide space at the border of the panel (Fig. 4.14), in order to maximize the distance from the cells and so minimize their effect.
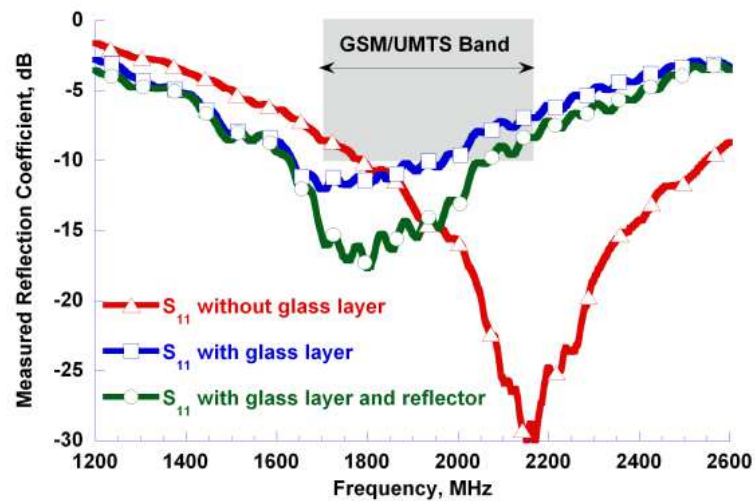
Fig. 4.15. - Measured reflection coefficients of the proposed TSSA, with and without the cover glass, and in presence of a reflector at a distance of R=30mm.

The miniaturization effect of the 8mm-thick glass layer is evident, while the variations introduced by a reflector at a distance R=30mm are much smaller. The cover glass layer determines a frequency shift of about 350MHz. Subsequent to the above preliminary measurements, a fine tuning of some geometrical parameters was used to get a return loss greater than 10dB in the whole band of interest, in presence of a reflector at a distance R=30mm form the panel bottom. Final geometrical values are shown in Table II. Reflection coefficient measurements are shown in Fig. 4.16, when the slot is attached on the back side of the PV panel, in presence of the metallic reflector at a distance of R=30mm, and at different distances from the nearby PV cells; indeed, the slot antenna has been measured when positioned at the center of the room available between the four columns that are separated by a distance D=20cm, D=30mm and D=50mm.
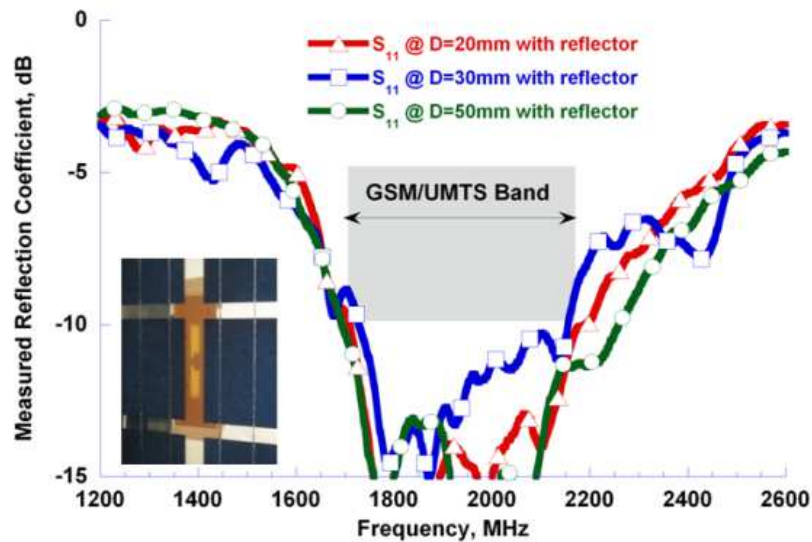
Fig. 4.16. - Measured reflection coefficient of the TSSA by varying the distance between the slot and the nearby PV cells (the slot is positioned at the center of the room available between adjacent columns of PV cells, Fig. 4.14). The metallic reflector is placed at a distance of R=30mm from the panel bottom.

TABLE II
PV PANEL INTEGRATED PROTOTYPES

TSSA DIMENSIONS (MM)			
N	200	A	42.5
M	70	B	49
L	105	C	54.3
W	14.5	R	30

If the specific application requires a bidirectional radiation pattern (as that about solar fields and mentioned in the Introduction) the reflector can be removed. The absence of the metallic reflector results in a slight impedance mismatching (Fig. 4.17), which can be recovered by varying some of the antenna geometrical parameters, as for example the length C (see Fig. 4.4).
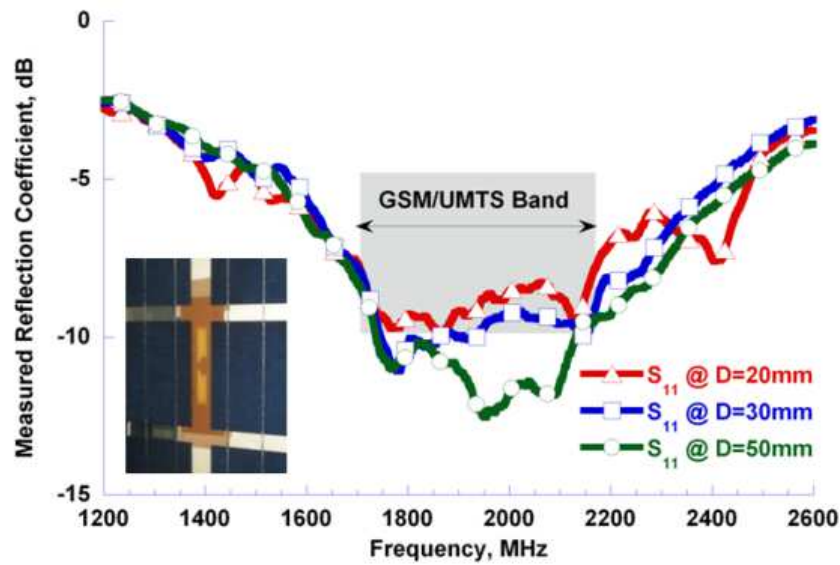
Fig. 4.17. - Measured reflection coefficient of the TSSA by varying the distance between the slot and the nearby PV cells (the slot is positioned at the center of the room available between adjacent columns of PV cells, Fig. 4.14). The metallic reflector has been removed.

A possible approach to improve impedance tuning without changing slot geometrical parameters consists in moving the slots with respect to the nearby cells, for example by shifting the slot along the direction of its longer axis (y-axis) In Fig. 4.18, the reflection coefficient of the antenna placed in three different positions (A, B, and C) is shown, when the distance between two solar cells columns is D=20mm, which corresponds to the worst case in terms of impedance detuning (Fig. 4.17). In *Position A*, the centers of the slot antenna and solar cells are aligned along the x-direction (Fig. 4.18a). Instead, in *Position B* the slot center point corresponds to the symmetric center of a group of 4 cells (Fig. 4.18b). The *Position C* is a intermediate position between A and B.
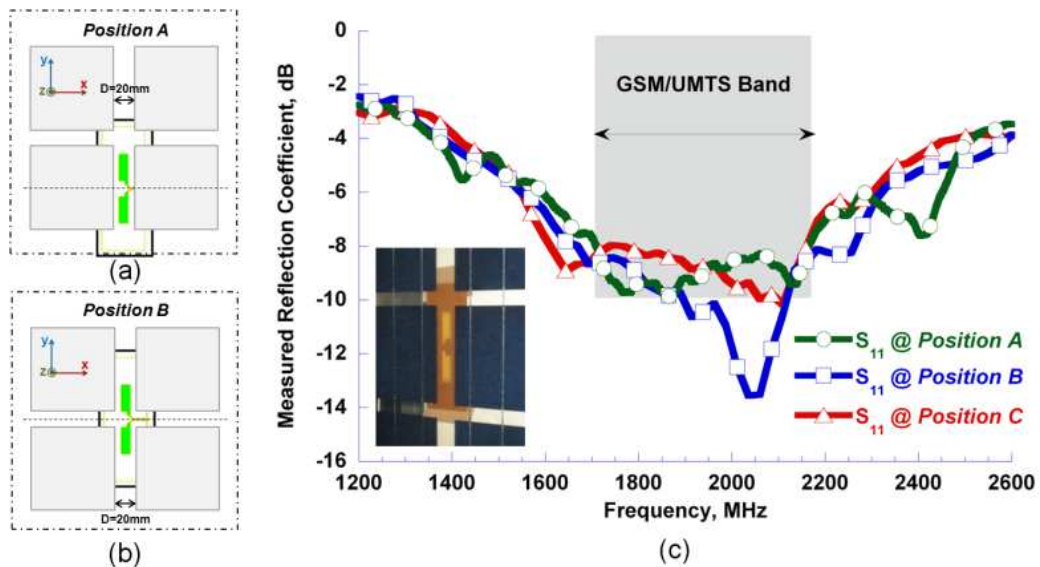
Fig. 4.18. - Measured reflection coefficient of the TSSA by varying the relative position of the slot antenna with respect to the nearby solar cells, along the y-axis. Different position were considered. The Position C is a intermediate position, between Position A and B.

Measured results in Fig. 4.18 show that a small shift with respect to the *y*-axis represents an effective parameter to match the antenna without changing its geometry. Moreover, this effect must be considered when an arrangement of slots is used to implement a linear array along the *y*-axis, since the input impedance of each array element will be a function of its relative location with respect to nearby cells.

4.3.2   Measurements results for the SSA prototype

A 180-W-RSP180S-50M PV panel [76] was employed to check the SSA input impedance for different locations of the antenna with respect to the panel surface (Fig. 4.19). The 1580x808 mm^2 panel consists of 72 monocrystalline silicon octagonal solar cells (125$\times$125 mm^2); a 25mm-thick aluminum panel frame can be employed to fix the panel on a supporting structure. In the top and bottom side of the solar cell matrix, a 4mm-thick cover glass and a 1mm-thick Tedlar® film are present, respectively. The available space between each 4 octagonal solar cells group is a *J* =30mm-side square.
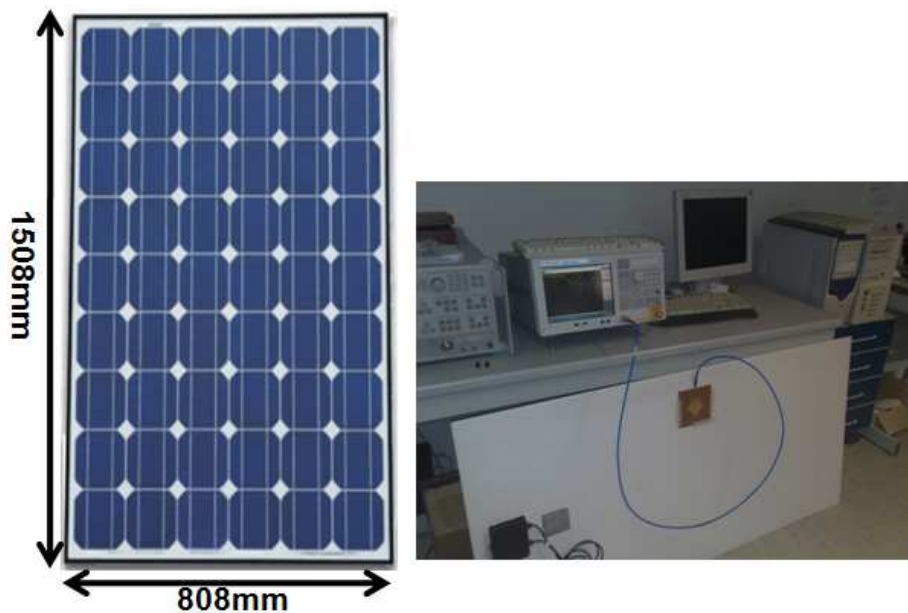
Fig. 4.19. - The RSP180S-50M PV panel used for testing the SSA. The J-side square space (Fig. 4.2b) between cells is 30x30mm2.
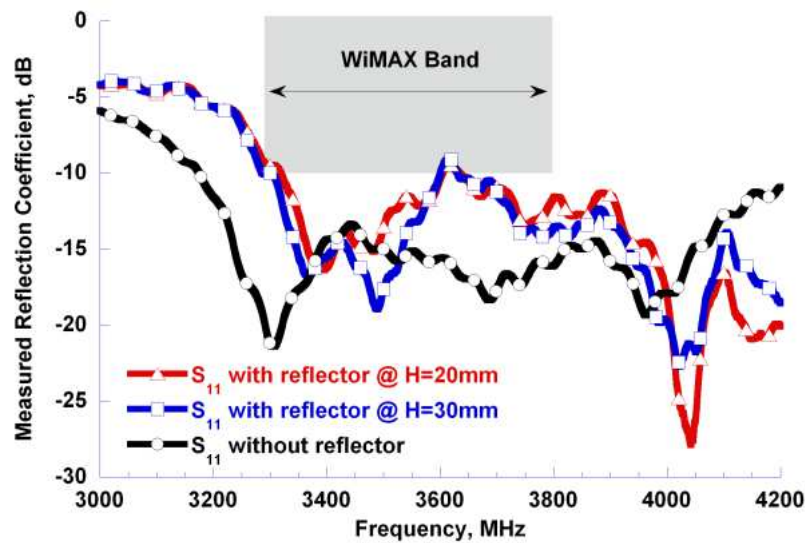
Fig. 4.20. - Measured reflection coefficient of the proposed SSA attached to the back side of a PV panel, with and without the reflector (the reflector was at a distance H=20mm or H=30mm from the FR4 bottom).

Fig. 4.20 shows the measured reflection coefficient of the SSA when it is attached on the PV panel backside, with and without a reflector. An aluminum reflector can be easily fixed to the metallic frame, at a distance of about 20mm from the FR4 bottom side. In the prototyping stage a decreasing of the stub length (*S*) was necessary, by setting this parameter equal to 12.3mm. The measured reflection coefficient (Fig. 4.20) of the integrated antenna without the reflector was below -14dB in the band of interest. The presence of a reflector resulted in a slight mismatching and in a frequency shift. Anyway, the antenna reflection coefficient was still below -10dB in the whole WiMAX band.

4.4   Conclusions

Two slot antenna configurations have been optimized to fit the room between adjacent PV cells of a class of commercial PV panels. A linear slot (three-stepped slot antenna) with width of 13 mm and length of 94.2 mm can achieve a return loss greater than 10dB in a 24% percentage frequency bandwidth, like that required for GSM/UMTS applications. Moreover, a square slot with a side smaller than 20mm can be used to implement an antenna operating in the 3300–3800MHz WiMAX bands. The cover glass layer of the PV panel has been employed to achieve an effective and valuable antenna miniaturization. Experimental investigations on antenna prototypes attached to real PV panels have been used to evaluate the effect of cells nearby the slots. Moreover, the presence of a reflector has been considered to get an unidirectional radiation pattern and increase antenna gain. The proposed slot antennas represent low-cost and compact solutions, which can be integrated into existing PV panels with a relatively easy mechanical process.

5 Dual-Band UHF-RFID/WLAN Circularly Polarized Antenna for Portable RFID Readers

5.1 Introduction

In recent years, RFID (Radio Frequency Identification) rapidly attracted a considerable attention as an effective and low-cost labeling technology, in supply chain management, logistics and access control. A number of frequency bands have been assigned to the RFID technology: 125 KHz (Low-frequency band, LF), 13.56 MHz (High frequency band, HF), 866-928 MHz (European and FCC Ultra-high frequency bands, UHF), 2400-2485 MHz and 5725-5875 MHz (Microwaves, MW). In this context, dual-band antennas have been investigated for different frequency bands and/or applications: HF/UHF [77], UHF/GPS [78], UHF/MW [3]-[84] and MW-2.4GHz/MW-5.8GHz [85]-[89]. Among them, those dual-band antennas that are suitable to operate at both the UHF-RFID and 2.4GHz bands are of specific interest for portable readers, as they enable the RFID reader to transmit collected data toward a management data center through a wireless local area network (WLAN). The dual-band (FCC UHF and MW bands) antennas that have been presented in [3]-[82] are linearly polarized antennas. In [3], the dual-band functionality was obtained by combining a single patch with an aperture in the antenna ground plane; in [4], an annular plate with curved rectangular slots has been designed; finally, an aperture-coupled patch and a marquise-brilliant-diamond-shaped patch have been proposed in [81] and [82], respectively. On the other hand, in order to make the RFID tag detection and WLAN link performance independent from the handheld reader orientation, a circularly polarization is preferred, at both frequency bands. This feature was achieved in [7] by resorting to two circularly polarized stacked patches, while two concentric ring radiators excited through coupling apertures have been suggested in [84]. The antennas in [7]-[84] exhibit an extent of about $\lambda/2 \times \lambda/2 \times \lambda/40$, where λ is the free-space wavelength at

the UHF-RFID central frequency. A more compact ($\lambda/5 \times \lambda/5 \times \lambda/50$) and low-cost dual-band antenna solution for handheld readers was presented in [78], where two circularly polarized printed quadrifilar antennas at UHF RFID (902-928MHz) and GPS (1575 MHz) frequency bands, concentrically arranged, have been designed. This compact solution presents four orthogonally arranged TLX-9 substrates for the lower band (UHF RFID) and an FR4 substrate placed parallel to the ground plane for the higher frequency band.

In this Chapter, a compact, low-cost, dual-port dual-band circularly polarized antenna is presented for UHF-RFID (FCC UHF band, 902-928 MHz) and WLAN (2400-2480 MHz) applications. Two radiators (a series of four inverted-F meandered monopoles and a miniaturized patch, for the UHF-RFID and WLAN frequency bands, respectively) are printed on the same side of an FR4 substrate. A proper layout optimization was needed to mitigate the mutual coupling between the nearby radiating elements. Reflection coefficient and isolation parameter have been investigated. The achieved antenna compactness (60mm×60mm×7mm, corresponding to about $\lambda/5 \times \lambda/5 \times \lambda/50$ at the UHF RFID central frequency of 900MHz) allows for an easy integration in handheld UHF-RFID readers. Furthermore, the measured radiation patterns and axial ratio (in both the operating frequency bands) are shown and compared with the simulated results. Simulated results have been obtained by CST Microwave Studio.

5.2   Antenna Design and Performance

The antenna is composed of two FR-4 substrates (*Layer 1* and *Layer 2* in Fig. 1) separated by a distance *H* through a set of 4-pin headers. The distance *H* can be used to effectively control antenna gain performance. In *Layer 1* top surface (Fig. 2a), four identical inverted-F meandered monopoles operating at the UHF-RFID band are realized. Each monopole is 65.4mm long, but 7 meanders have been introduced to fit the available space; thus, their actual length *L* reduces to 48.2mm (73.7% reduction). Each monopole input (*Layer 1*) is close to an antenna corner, at a distance of 4mm from the edge, and is fed by a microstrip line (*Layer 2*) that implements the sequential rotation technique [90]-[91]. The sequential rotation technique consists in sequentially rotating each element together with imposing a 90° offset in the feed excitation phase. Sequential rotation feeding is effective to improve cross polarization (circular polarization purity) and radiation pattern symmetry. The feeding network is realized on the *Layer 2* top surface and has been designed with a single port (*Port 1*) in the middle of the substrate; 4-pin headers have been used to connect the two layers. The antenna ground plane is in the *Layer 2* bottom surface. A detailed representation of the connection between the feeding line (*Layer 2*) and the feeding pin is shown in Fig. 3. In each of the 4-pin headers, one pin connects the feeding network to the monopole, meanwhile another pin connects the monopole stub (*Layer 1*) to the *Layer 2* ground plane, thus working as a shorting pin. Two other pins are not connected to the radiating structure, but they give mechanical robustness to the antenna and set the distance *H* between the two substrates. Since the feeding line and the ground plane have been realized onto two opposite surfaces of *Layer 2*, the feeding pin would result shorter than

the other pins of a length equal to 1.53mm, which corresponds to the FR-4 substrate thickness. To simplify antenna realization process, a via has been realized in the *Layer 2*, and the electrical connection (soldering) between the feeding line and the pin header occurs in the *Layer 2* bottom surface.

A WLAN miniaturized patch antenna has been realized by exploiting the available space between the four meandered monopoles, without increasing the overall antenna volume. A *W*-wide circularly polarized square patch has been designed on the same surface as for the meandered monopoles (*Layer 1*). Since the available space (among the four meandered monopoles) was not enough for a conventional patch operating at 2.4GHz, four cuts at the patch corners have been introduced in order to decrease patch resonance frequency [92] (so reducing the patch surface area of about 30%). The patch cuts are asymmetric (C=2.3mm, D=1mm), in order to radiate a CP field. Thanks to the patch miniaturization, the design of the meandered monopole layout is only slightly influenced by the presence of the patch. The patch antenna ground plane, 30mm×30mm in size, is printed on the bottom surface of *Layer 1*. A narrow frequency band of the axial ratio is expected for the WLAN antenna, as for conventional miniaturized patch [92]. It is known that the adopted miniaturization techniques (the meanders in the monopoles and the cuts in the patch) reduce the antenna gain. Thus, a trade-off between the antenna miniaturization and the achievable maximum gain has been considered in order to guarantee satisfactory WLAN connectivity and tag reading range. Antenna cost and complexity have also been considered.
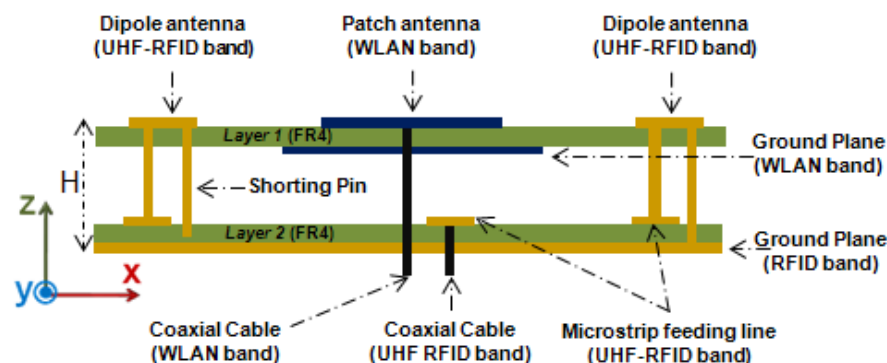
Fig. 5.1. - Stack-up of the proposed dual-port dual-band circularly polarized antenna.

(a)   (b)
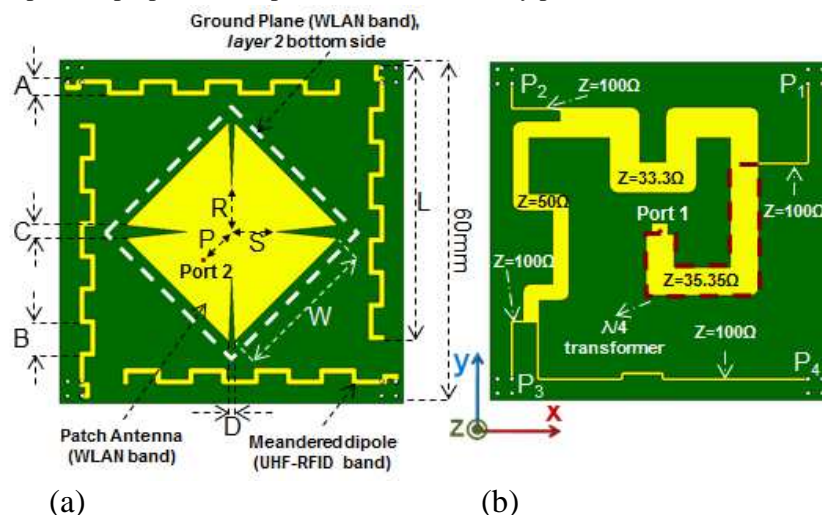
Fig. 5.2 - Antenna top view: (a) Layer 1 and (b) Layer 2
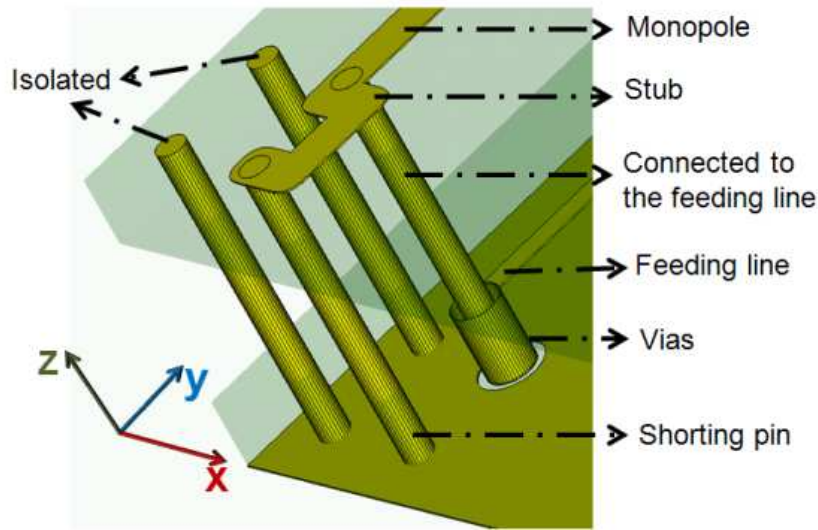
Fig. 5.3. - Header pins connection between the meandered monopoles, feeding network and ground plane, for the proposed dual band circularly polarized antenna.

In Table I, the final values of the antenna geometrical parameters are shown.

TABLE I
ANTENNA SIZE (mm)

DUAL BAND ANTENNA FOR PORTABLE RFID READER									
A	*B*	*C*	*D*	*L*	*P*	*R*	*S*	*W*	*H*
2	5.7	2.3	1	48	7	7.8	7.8	27.7	7

The antenna has been optimized for the FCC UHF RFID band (2.8% percentage bandwidth). Anyway, by properly increasing the effective length of both the meanders (*A* and *B* parameters) and the $\lambda/4$ transformer in the feeding line (Fig. 5.2), it is possible to obtain an antenna design operating in the narrower UHF RFID ETSI band (865-868 MHz, 0.34% percentage bandwidth). The patch ground plane size and shape have been optimized in order to reduce the mutual coupling between the patch and the monopoles. For the same reason, the patch sides are 45° rotated with respect to the four meandered monopoles (Fig. 2).

In Fig. 5.4, the surface current peak on the patch and the meandered monopoles is shown, at 915MHz and 2440MHz when *Port1* and *Port2* are fed, respectively (the input port that is not fed is connected to a matched load); a low coupling level between the patch and the meandered dipoles can be noted.
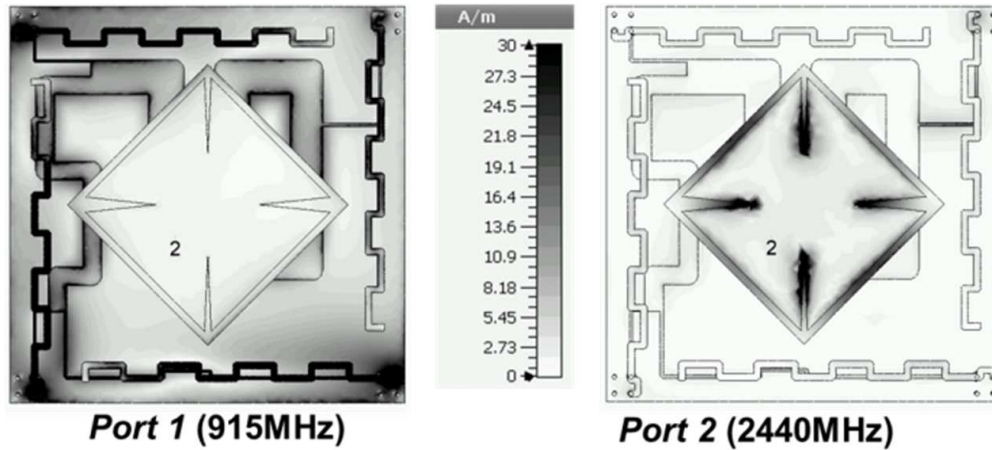
Fig. 5.4. - Surface current peak for the proposed dual-band circularly polarized antenna, at 915MHz (Port1 fed) and 2440MHz (Port2 fed).
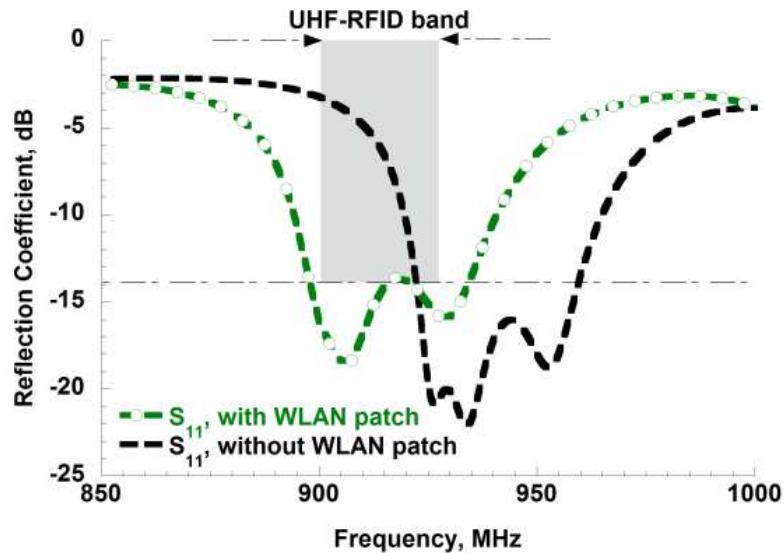
Fig. 5.5. - Reflection Coefficient of the proposed circularly polarized dual band antenna for the UHF-RFID band, when the WLAN patch is either present or removed.

In Fig. 5.5, the reflection coefficient at *Port1* is shown, with and without the presence of the WLAN patch. A 15 MHz frequency shift of the antenna resonance occurs when the patch is removed. In the design process, above patch effect has been easily compensated by a fine tuning of the length of the meandered monopoles. In Table II, the simulated gain in the broadside direction and the radiation efficiency for the UHF RFID and WLAN band are shown. The simulated 3dB axial ratio percentage bandwidth in the two bands of interest results to be 3.1% and 0.9%.

TABLE II
SIMULATED ANTENNA PERFORMANCE

f [MHz]	Gain [dBic]	Radiation Efficency	f [MHz]	Gain [dBic]	Radiation Efficency
905	-1.6	38%	2400	1.5	33%
910	-1.2	35%	2420	1.6	34%
915	-0.5	45%	2440	1.7	34%
920	0	48%	2460	1.7	34%
925	-0.1	50%	2480	1.8	34%

5.3   Experimental results

A prototype of the dual-band UHF-RFID/WLAN antenna for portable readers has been fabricated; photos of the RFID feeding line and the two radiating elements are shown in Fig. 6. Both measured and simulated results for the reflection coefficient and port isolation are shown in Figs. 7-8, exhibiting a reasonable agreement. The measured reflection coefficient (below -14dB in both the UHF-RFID and WLAN bands) results to be lower than the simulated one, and it is probably due to the losses in the FR4 laminate.

The measured port isolation is greater than 25 dB in both the UHF-RFID and WLAN frequency bands. Radiation pattern measurements have been performed in the anechoic chamber of the Department of Electrical Engineering of the University of Oviedo. In Fig. 5.9-Fig. 5.10 the measured radiation patterns (for both antennas a right hand circular polarization has been considered) at the XZ and YZ planes, at 915MHz and 2440 MHz when the *Port 1* and *Port 2* are fed, respectively, are compared with numerical simulations. The maximum gain in the broadside direction (*z*-axis) is -0.6dBic in the UHF FCC RFID band and 1.2 dBic in the WLAN band. The measured HPBW is about 80° and 85° in the XZ plane and YZ plane, respectively, for both the operating frequency bands.
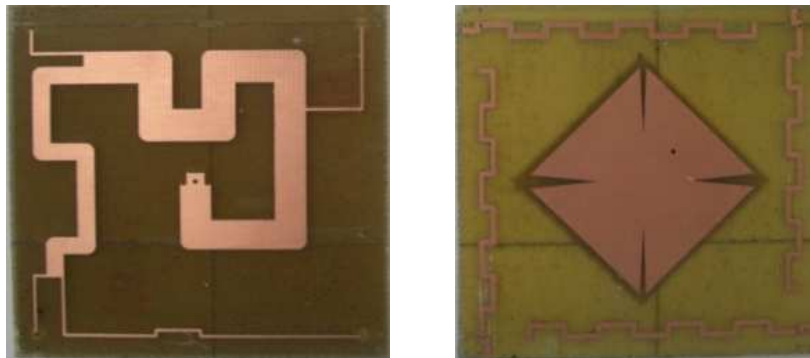
Fig. 5.6. - Prototype of the proposed circularly polarized dual-band antenna: (a) the feeding line on the top side of Layer 2 and (b) the two radiating elements on the top side of the Layer 1.
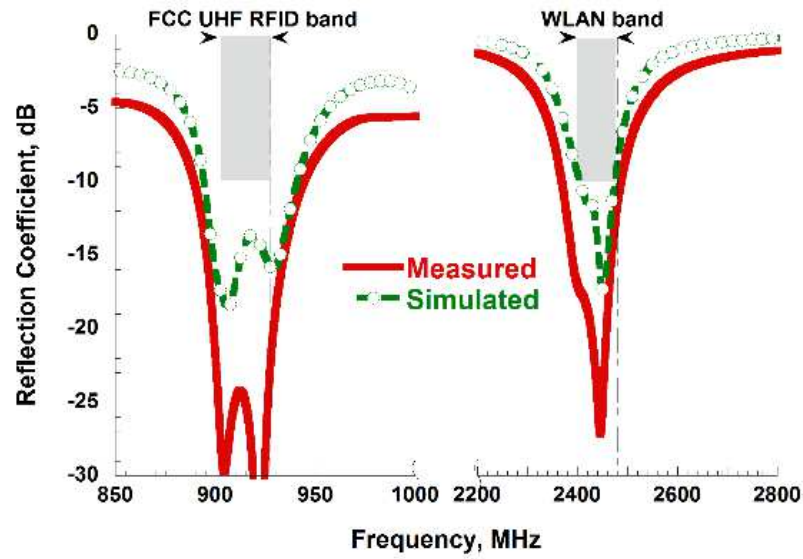
Fig. 5.7. - Simulated and measured reflection coefficient in the UHF-RFID and WLAN bands.
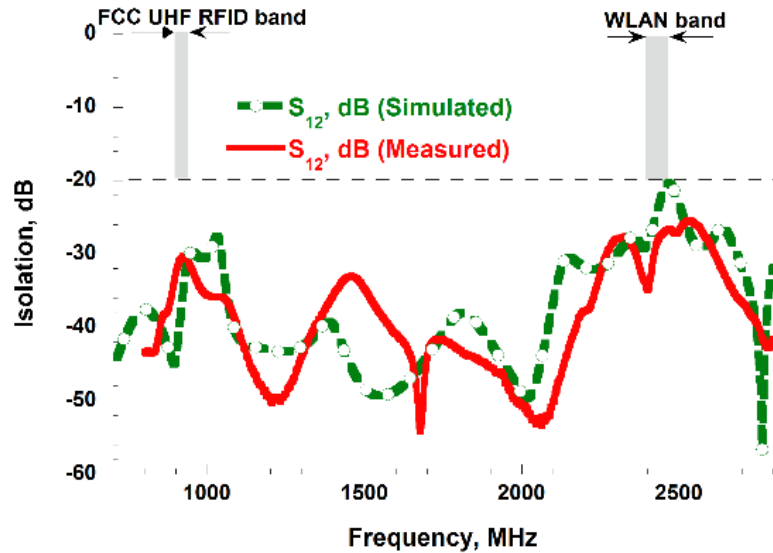
Fig. 5.8. - Simulated and measured isolation between *Port1* and *Port2*.

| (a) | (b) |
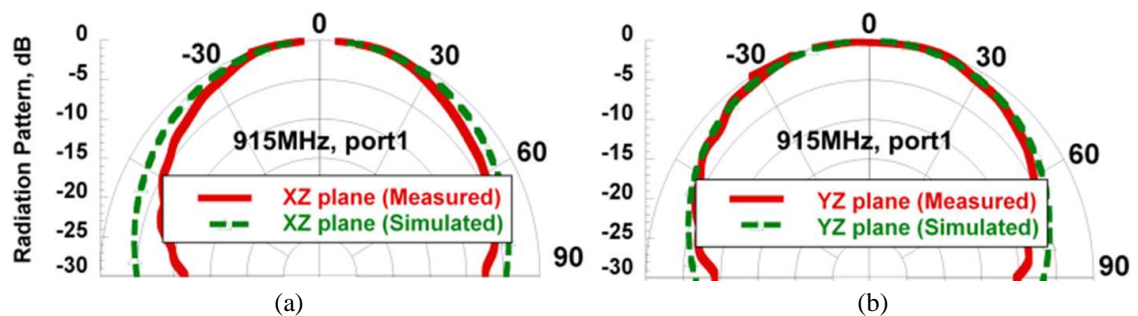
Fig. 5.9. - Simulated and measured radiation patterns (co-polar component) in the (a) XZ and (b) YZ planes, at 915 MHz (central frequency for the UHF RFID band), when Port 1 is fed and Port 2 is matched.

(a)   (b)
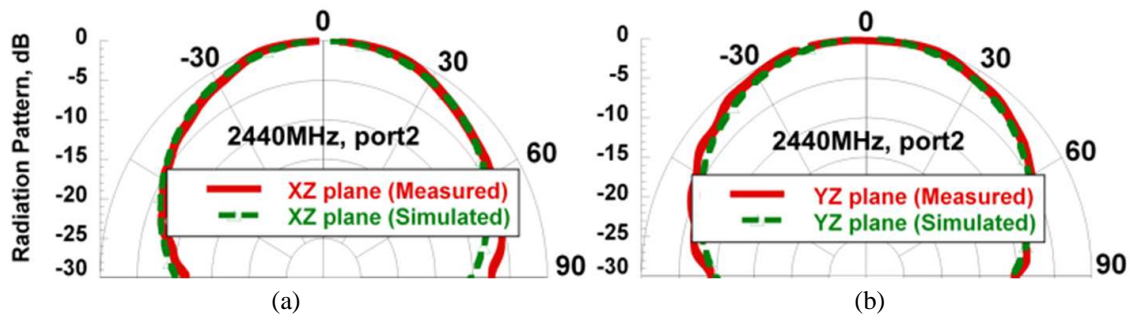
Fig. 5.10. - Simulated and measured radiation patterns (co-polar component) in the (a) XZ and (b) YZ plane, at 2440 MHz (central frequency of the WLAN band)), when Port 2 is fed and Port 1 is matched.

Measured and simulated antenna axial ratio in the broadside direction is shown in Fig. 5.11. Moreover, the axial ratio in the XZ and YZ planes (Fig. 5.12-Fig. 5.13) is below 3dB in a beam of at least 60° around the broadside direction, for both applications.
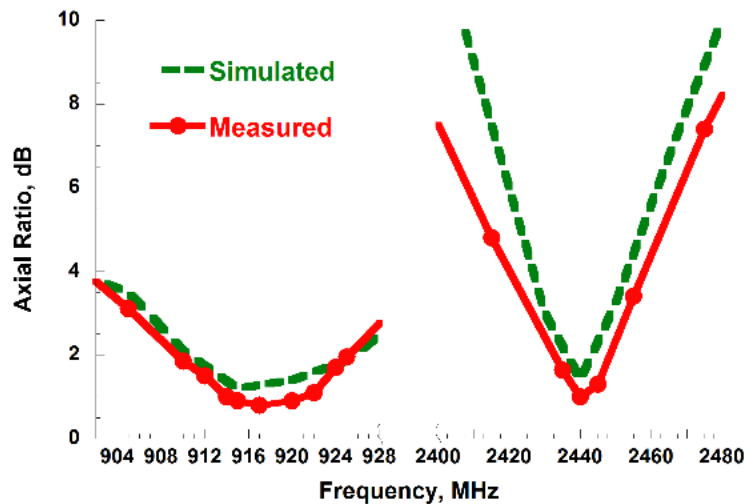
Fig. 5.11. - Simulated and measured Axial Ratio in the antenna broadside direction for the RFID UHF and WLAN frequency band, when Port1 and Port2 is fed, respectively.
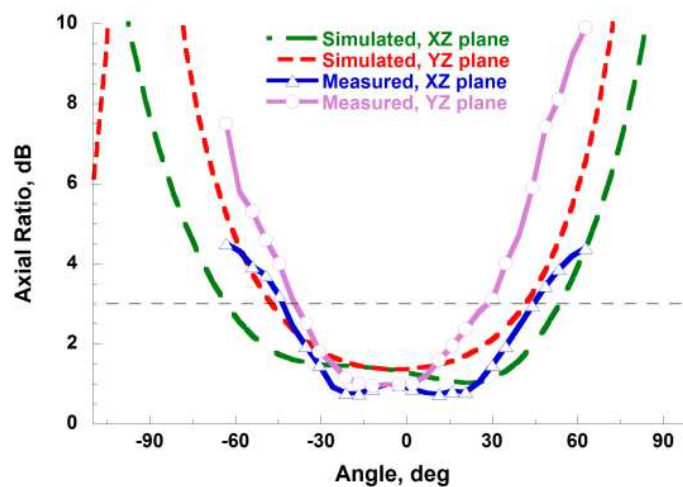
Fig. 5.12. - Simulated and measured Axial Ratio in both XZ and YZ planes, at 915 MHz (central frequency of the UHF RFID FCC band).
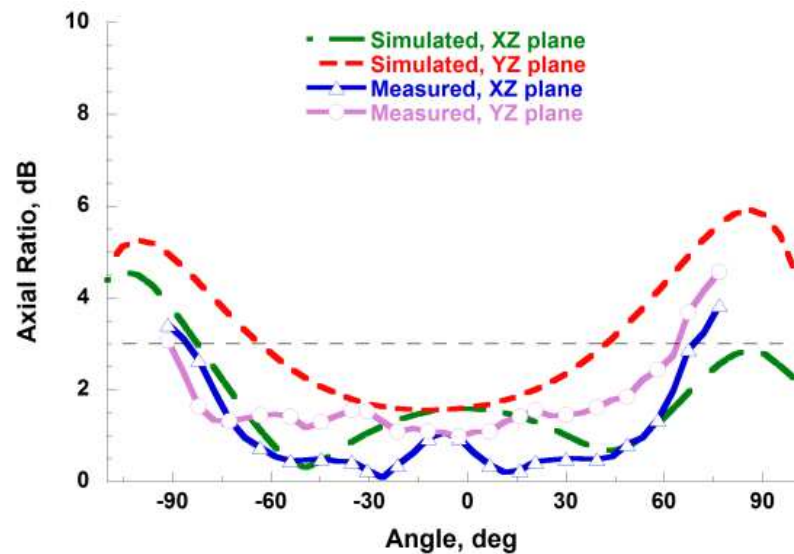
Fig. 5.13. - Simulated and measured Axial Ratio in both XZ and YZ planes, at 2440 MHz (central frequency of the WLAN band).

5.4   Conclusions

A compact, low-profile, low-cost, two-port dual-band circularly polarized antenna for UHF-RFID and WLAN applications has been designed, which is suitable to be integrated in the PCB of a portable reader. The radiating element for the UHF-RFID band (902-928 MHz) has been realized through a circular array of four inverted-F meandered monopoles, where the array elements are excited with a 90° phase offset (sequential rotation feeding technique) through a microstrip feeding network. In order to also provide the portable reader with a wireless web access, a miniaturized CP patch has been added for the WLAN IEEE 802.11b,g radio link, by exploiting the available space between the four array elements, without increasing the overall antenna volume (60mm×60mm×7mm). The patch loading effect on the monopoles can be compensated by adjusting the meandered monopole length (measured isolation is greater than 25dB). Reflection coefficient, port isolation, axial ratio and radiation patterns are evaluated by numerical simulations and compared with measurements on an antenna prototype. Reflection coefficient, port isolation, axial ratio and radiation patterns have been evaluated by numerical simulations and compared with measurements on an antenna prototype. Despite of the limited antenna volume, good performances have been measured.

Conclusions

In this dissertation, the mutual coupling effect is analyzed and studied in a number of wireless systems for identification, sensing and communication.

In Chapter I and Chapter II low-cost and low-profile antennas for Near-Field UHF RFID desktop readers have been presented. These antenna solutions have been designed and optimized to maximize the field generated on the antenna surface and up to few tens of centimeters from the antenna. This allows for limiting the far-field radiation and then avoiding the undesired detection of farther tags (false-positive).

Furthermore, in biomedical engineering applications, several devices used to monitor the real-time human health conditions make use of the electromagnetic near-field coupling. Specifically, several systems and numerical methods have been designed to estimate the internal human status. In Chapter III, a novel method suitable to estimate the internal human tissues condition (i.e. estimate tissue permittivity variations due to the presence of lung water content or tumor masses) is described, and the mathematical approach used in the accuracy analysis is reported. In addition, numerical results are shown and commented.

In Chapter IV, antennas for GSM, UMTS, WiFi and WiMAX applications are presented. Specifically, they are optimized to be integrated in a commercial photovoltaic panel, exploiting the available space between solar cells and taking into account the near-field interaction with other elements (e.g. other radiating elements, glass layer or close solar cells).

Finally, in Chapter V a dual band antenna integrated in an UHF RFID handheld reader is presented for UHF RFID and WiFI applications. In this case, the near-field coupling between the two radiating elements represents an undesired effect that limits the overall system performance. To face with this effect, a proper geometry optimization is chosen for the two radiating elements, resulting in a good compromise between antenna performance and occupied volume.

Bibliography

[1]   Y.-S. Chen, S.-Y. Chen, and H.-J. Li, "Analysis of Antenna Coupling in Near-Field Communication Systems", *IEEE Transactions on Antennas and Propagation*, vol. 58, no. 10, pp. 3327-3335, October 2010.

[2]   J. Lee and S. Nam, "Fundamental Aspects of Near-Field Coupling Small Antennas for Wireless Power Transfer", *IEEE Transactions on Antennas and Propagation*, vol. 58, no. 11, pp. 3442-3449, November 2010.

[3]   I.-J. Yoon and H. Ling, "Realizing Efficient Wireless Power Transfer Using Small Folded Cylindrical Helix Dipoles", *IEEE Antennas and Wireless Propagation Letters*, vol. 9, pp 846-849, August 2010.

[4]   K. Finkenzeller, *RFID Handbook*, 2nd Edition, Wiley, 2003.

[5]   F. Fuschini, C. Piersanti, L. Sydanheimo, L. Ukkonen, and G. Falciasecca, "Electromagnetic Analyses of Near Field UHF RFID Systems," *Antennas and Propagation, IEEE Transactions on* , vol.58, no.5, pp.1759-1770, May 2010.

[6]   P. V. Nikitin, K. V. S. Rao, and S. Lazar, "An Overview of Near Field UHF RFID," *RFID, 2007. IEEE International Conference on* , vol., no., pp.167-174, 26-28 March 2007.

[7]   A. Buffi, P. Nepa, and G. Manara, "Analysis of Near-Field Coupling in UHF-RFID Systems", *Proceedings of 2011 IEEE-APS Topical Conference on Antennas and Propagation in Wireless Communications* (APWC 2011), pp. 931-934, 2011.

[8]   D. M. Dobkin, S. M. Weigand, and N. Iye, "Segmented magnetic antennas for near-field UHF RFID", *Microwave Journal*, June 2007.

[9]   X. Li and Z. Yang, "Dual-printed-dipoles reader antenna for UHF near-field RFID applications", IEEE *Antennas and Wireless Propagation Letters*, vol. 10, 2011.

[10]   X. Li, J. Liao, Y. Yuan, and D. Yu, "Segmented coupling eye-shape UHF band near field antenna design", *Asia Pacific Microwave Conference* (*APMC*), 2009.

[11]   X. Qing, C. K. Goh, and Z. N. Chen, "Segmented loop antenna for UHF near-field RFID applications", *Electronics Letters*, vol. 45, no. 17, August 2009.

[12]   H. W. Liu, C. F. Yang, C. H. Weng, H. L. Kuo, K. H. Wu, and Y. S. Lin, "An UHF reader antenna design for near-field RFID applications", *Asia Pacific Microwave Conference* (*APMC*), 2009.

[13]   A. Buffi, A. A. Serra, P. Nepa, H.-T. Chou, and G. Manara, "A Focused Planar Microstrip Array for 2.4 GHz RFID Readers*", IEEE Transactions on Antennas and Propagation*, vol. 58, no. 5, pp. 1536-1544, May 2010.

[14]   W. Choi, J. S. Kim, J. H. Bae, G. Choi, and J. S. Chae, "Near-field antenna for a radio frequency identification shelf in the UHF band", *IET Microwaves, Antennas & Propagation*, vol. 4, no. 10, pp. 1538-1542, 2010.

[15]   C. Y. Wu, J. Du, A. K. Ren, and J. Y. Li, "Large-area RFID reader antenna for smart shelf at UHF", *Electronics Letters*, vol. 48, no. 15, July 2012.

[16]   C. R. Medeiros, J. R. Costa, and C. A. Fernandes, "RFID Reader Antennas for tag detection in self-confined volumes at UHF", *IEEE Antennas and Propagation Magazine*, vol. 53, no. 2, April 2011.

[17]   C. R. Medeiros, J. R. Costa, and C. A. Fernandes, "RFID smart shelf with confined detection volume at UHF", *IEEE Antennas and Wireless Propagation letters*, vol. 7, 2008.

[18]   J. Hong, J. Choo, J. Ryoo, and C. Choi, "A shelf antenna using near-field without dead zones in UHF RFID", *IEEE International Conference on Industrial Technology*, 2009.

[19]   W. S. Lee, K. S. Oh, and J. W. Yu, "Design of spiral-shaped UHF near-field reader antenna for RFID applications", *IEEE MTT-S International Microwave Workshop Series on Intelligent Radio for Future Personal Terminals* (*IMWS-IRFPT*), 2011.

[20]   A. Ren, C. Wu, Y. Gao, and Y. Yuan, "A Robust UHF Near-field RFID Reader Antenna", *IEEE Transactions on Antenna and Propagation*, vol 60, no. 4, April 2012.

[21]   A. Ren, C. Wu, T. Wang, and B. Yao, "A novel design for UHF near-field RFID reader antenna based on traveling wave", *12th IEEE International Conference on Communication Technology* (*ICCT*), 2010.

[22]   A. Michel, R. Caso, A. Buffi, P. Nepa, G. Isola, and H.-T. Chou, "Design and Performance Analysis of a Planar Antenna for Near-Field UHF RFID Desktop Readers", *Asia-Pacific Microwave Conference* (APMC), pp. 1019-1021, Kaohsiung, Taiwan, December 2012

[23]   I. Wolff, *Coplanar Microwave Integrated Circuits*, Ed. Wiley, 2006.

[24]   http://www.lab-id.com/inlay_uhf.html

[25]   http://www.alientechnology.com/docs/products/Alien-Technology-Higgs-3-ALN-9640-Squiggle.pdf

[26]   Bee, Y.S., Chen, Z.N., Lu, A.C.W., Sunappan, V., and Wai, L.L., "60-GHz LTCC antenna array with microstrip to CPW transition," Asia Pacific Microwave Conference , December 2009, pp.1938-1941.

[27]   R. Want, "Near field communication", *IEEE Pervasive Computing*, vol. 10, no. 3, pp. 4-7, 2011.

[28]   G. Franceschetti, G. Oliveri, P. Rocca, and A. Massa, "Advances on remote wireless power transmission at the ELEDIA research center", *2013 IEEE Wireless Power Transfer* (WPT), pp. 191-194, May 2013.

[29]   R. Krigslund, P. Popovski, G. F. Pedersen, K. Olesen, "Interference Helps to Equalize the Read Range and Reduce False Positives of Passive RFID Tags", *IEEE Trans. Industrial Electronics*, vol. 59, no. 12, pp. 4821-4830, December 2012.

[30]   J. Shi, X. Qing, and Z. N. Chen, "Electrically Large Zero-Phase-Shift Line Grid-Array UHF Near-Field RFID Reader Antenna", *IEEE Trans. Antennas and Propagation*", vol. 62, no. 4, April 2014.

[31]   J. Shi, X. Qing, Z. N. Chen, and C. K. Goh, "Electrically Large Dual-Loop Antenna for UHF Near-Field RFID Reader", *IEEE Trans. Antennas and Propagation*", vol. 61,no. 3, March 2013.

[32] X.-D. Wei, B.-J. Hu, and H.-L. Zhang, "Novel UHF Near-Field RFID Reader Antenna Based on Double-Sided Parallel-Strip Line", *IEEE Antennas and Wireless Propagation Letters*, vol. 13, 2014.

[33] J. K. Pakkathillam, M. Kanagasabai, C. Varadhan, and P. Sakthivel, "A Novel Fractal Antenna for UHF Near-Field RFID Readers", *IEEE Antennas and Wireless Propagation Letters*, vol. 12, 2013.

[34] A. S. Andrenko, and M. Kai, "Novel Design of UHF RFID Near-Field Antenna for Smart Shelf Applications", *Asia Pacific Microwave Conference* (*APMC*), 2013.

[35] H. W. Liu, C. F. Yang, C. H. Weng, H. L. Kuo, K. H. Wu, and Y. S. Lin, "An UHF reader antenna design for near-field RFID applications", *Asia Pacific Microwave Conference* (*APMC*), 2009.

[36] A. Michel, R. Caso, A. Buffi, P. Nepa, and G. Isola, "Meandered TWAS array for near-field UHF RFID applications", *Electronics Letters*, vol. 50, no. 1, pp. 17-18, January 2014.

[37] A. Michel, R. Caso, A. Buffi, P. Nepa, G. Isola, "Modular antenna for reactive and radiative near-field regions of UHF-RFID desktop readers", to be presented at *URSI-GASS*, Beijing, China, August 2014.

[38] Nasimuddin, X. Qing, and Z.N. Chen, "Compact circularly polarized symmetric-slit microstrip antennas", *IEEE Antennas and Propagation Magazine*, vol. 53, no. 4, pp. 63-75, 2011.

[39] R. Caso, A. Michel, M. Rodriguez-Pino, P. Nepa, "Dual-Band UHF-RFID/WLAN Circularly Polarized Antenna for Portable RFID Readers", *IEEE Trans. Antennas Propagation*, vol. 62, no. 5, pp. 2822-2826, May 2014.

[40] http://www.caenrfid.it/en/CaenProd.jsp?mypage=2&parent=98&idmod=818

[41] http://www.lab-id.com/datasheet/inlay_UHF/UH414.pdf

[42] R. Paradiso, G. Loriga, and N. Taccini, "A Wearable Health Care System Based on Knitted Integrated Sensors", IEEE Trans. on Information Technology in Biomedicine, Vol. 9, No. 3, Sep 2005

[43] T. Yilmaz, and Y. Hao, "Compact Resonators for Permittivity Reconstruction of Biological Tissues", XXXth URSI General Assembly and Scientific Symposium, 2011.

[44] S. Salman, L. Z. Lee, and J. L. Volakis, "A Wearable Wrap-Around Sensor for Monitoring Deep Tissue Electric Properties", IEEE Sensor Journal, Vol. 14, No. 8, Aug 2014

[45] S. Salman, Z. Wang, E. Colebeck, A. Kiourti, E. Topsakal, and J. L. Volakis, "Pulmonary Edema Monitoring Sensor With Integrated Body-Area Network for Remote Medical Sensing" IEEE Trans. on Antennas and Propagation, Vol. 62, No. 5, May 2014

[46] S. Salman, D. Psychoudakis, J. L. Volakis, "Determining the Relative Permittivity of Deep Embedded Biological Tissues", IEEE Antennas and Wireless Propagation Letters, Vol. 11, 2012

[47] J. D. Shea, P. Kosmas, S. C. Hagness, and B. D. Van Veen, "Three-dimensional microwave imaging of realistic numerical breast phantoms via a multiple-frequency inverse scattering technique", Medical Physics 37, 4210 (2010); doi: 10.1118/1.3443569

[48] C. P. Joachimowicz, and J.-P. Hugonin, "Inverse Scattering: An Iterative Numerical Method for Electromagnetic Imaging Nadine", IEEE Trans. on Antennas and Propagation, Vol. 39, No. 12, Dec 1991

[49] A. H. Golnabi, P. M.Meaney, and K. D. Paulsen, "Tomographic Microwave Imaging With Incorporated Prior Spatial Information", IEEE Trans. on Microwave Theory and Techniques, Vol. 61, No. 5, May 2013

[50] L. Lo Monte, D. Erricolo, F. Soldovieri, and M. C. Wicks, "Radio Frequency Tomography for Tunnel Detection", IEEE Trans. on Geoscience and Remote Sensing, Vol. 48, No. 3, Mar 2010

[51] J. L. Volakis, and K. Sertel, "Integral Equation Methods for Electromagnetics", Scitech Publishing Inc, 2012

[52] P B Katehi, and G Alexopoulos, "Real axis integration of Sommerfelt integrals with applications to printed circuit antennas", Journal of Mathematical Physics, Mar 1983

[53] A. Alparslan, M. I. Aksun, and K. A. Michalski, "Closed-Form Green's Functions in Planar Layered Media for All Ranges and Materials", IEEE Trans. on Microwave Theory and Techniques, Vol. 58, no. 3, Mar 2010

[54] Z. H. Firouzeh, G.A.E. Vandenbosch, R. Moini, S.H.H. Sadeghi, and R. Faraji-Dana, "Efficient evaluation of Green's functions for lossy half-space problems", Progress In Electromagnetics Research, Vol. 109, pp. 139-157, 2010.

[55] W. C. Chew , "Waves and fields in homogeneous media", Wiley IEEE-press

[56] Constantine Balanis, "Antenna Theory Analysis and Design 3rd Edition", John Wiley and Sons Inc, 2005

[57] D. Andreuccetti, R. Fossi and C. Petrucci: An Internet resource for the calculation of the dielectric properties of body tissues in the frequency range 10 Hz - 100 GHz, website at http://niremf.ifac.cnr.it/tissprop/. IFAC-CNR, Florence (Italy), 1997. Based on data published by C.Gabriel et al. in 1996.

[58] M.J. Roo Ons, S.V. Shynu, M.J. Ammann, S.J. McCormack, and B. Norton, "Transparent patch antenna on a-Si thin-film glass solar module," *Electronics Letters* , vol.47, no.2, pp.85-86, Jan 2011.

[59] T. Yasin, and R. Baktur, "Inkjet printed patch antennas on transparent substrates," *IEEE Antennas and Propagation Society International Symposium*, 2010.

[60] T.W. Turpin, and R. Baktur, "Meshed Patch Antennas Integrated on Solar Cells," *IEEE Antennas and Wireless Propagation Letters*, vol. 8, pp. 693-696, 2009.

[61] N. Henze, A. Giere, H. Friichting, and P. Hofmann, "GPS Patch Antenna with Photovoltaic Solar Cells for Vehicular Applications," *58th IEEE Vehicular Technology Conference Fall*, Orlando, US, Oct. 6-9, 2003.

[62] C. Bendel, J. Kirchhof, and N. Henze, "Application of photovoltaic solar cells in planar antenna structures," *Proceedings of 3rd World Conference on Photovoltaic Energy Conversion*, vol. 1, pp. 220 – 223, May 11-18, 2003.

[63] N. Henze, M. Weitz, P. Hofmann, C. Bendel, J. Kirchhof, and H. Fruchting, "Investigation of planar antennas with photovoltaic solar cells for mobile communications," *15th IEEE International Symposium on Personal, Indoor and Mobile Radio Communications*, vol. 1, pp. 622 – 626, Sep. 5-8, 2004.

[64] S. Vaccaro, P. Torres, J.R. Mosig, et al., "Integrated solar panel antennas," *Electronics Letters*, 36, (5), pp. 390–391, 2000.

[65] M.J. Roo Ons, S.-V. Shynu, M.J. Ammann, S. McCormack, and B. Norton, "Investigation on Proximity-Coupled Microstrip Integrated PV Antenna," *2nd European Conference on Antennas and Propagation*, Nov. 11-16, 2007.

[66] S.V. Shynu, M.J. Ammann, and B. Norton, "Quarter-wave metal plate solar antenna," *Electronics Letters*, vol. 44(9), pp. 570-571, Apr 2008

[67] S.-V. Shynu, M.J. Roo Ons, P. McEvoy, M.J. Ammann, S.J. McCormack, and B. Norton, "Integration of Microstrip Patch Antenna With Polycrystalline Silicon Solar Cell," *IEEE transactions on Antennas and Propagation*, vol. 57(12), pp. 3969-3972, Dec. 2009.

[68] M. Danesh, and J.R. Long, "Compact Solar cell Ultra-Wideband dipole antenna," *IEEE Antennas and Propagation Society International Symposium,* 2010.

[69] T. Wu, R.L. Li, and M.M. Tentzeris, "A mechanically stable, low profile, omni-directional solar cell integrated antenna for outdoor wireless sensor nodes," *IEEE Antennas and Propagation Society International Symposium*, 2009.

[70] S.V. Shynu, M.J. Roo Ons, M.J. Ammann, B. Norton, and S. McCormack, "Dual band a-Si:H solar-slot antenna for 2.4/5.2GHz WLAN applications," *3rd European Conference on Antennas and Propagation*, pp. 408-410, Mar. 23-27, 2009.

[71] N. Henze, C. Bendel, and J. Kirchhof, "Photovoltaic power supply and antennas in one device for wireless telecommunication equipment," INTELEC 2005, Berlin, Germany, Sep. 18-22, 2005.

[72] K.L Chung and A.S. Mohan, "Effect of superstrate thickness on the performance of broadband circularly polarised stacked patch antenna," *IEEE Antennas and Propagation Society International Symposium*, vol.1, pp. 687- 690, Jun. 20-25, 2004

[73] W. Kueathawikun, P. Thumwarin, N. Anantrasirichai, and T. Wakabayashi, "Wide-Band Slot Antenna for IEEE 802.11b/g," *SICE-ICASE International Joint Conference*, Bexco, Busan, Korea, Oct. 18-21, 2006.

[74] J.Y. Jan, and J.W. Su, "Bandwidth enhancement of a printed wide-slot antenna with a rotated slot," *IEEE Transactions on Antennas and Propagation*, vol.53, no.6, pp. 2111- 2114, Jun. 2005.

[75] http://www.brandonisolare.com/

[76] http://www.risenenergy.com

[77] W.I Son, K.S. Oh, W.S. Lee, H.S. Tae, and J.W. Yu, "Dual-frequency antenna for HF/UHF handheld RFID reader," *IEEE MTT-S International Microwave Workshop Series on Intelligent Radio for Future Personal Terminals (IMWS-IRFPT)*, pp. 1-2, 2011.

[78] K.S Oh, W.I. Son, S.Y. Cha, M.Q. Lee, and J.W. Yu, "Compact Dual-Band Printed Quadrifilar Antennas for UHF RFID/GPS Operations," *IEEE Antennas and Wireless Propagation Letters*, vol.10, pp. 804-807, 2011.

[79] X. Zhishu, and L. Xiuping, "Aperture coupling two-layered dual-band RFID reader antenna design," *International Conference on Microwave and Millimeter Wave Technology (ICMMT)*, vol.3, pp. 1218-1221, Apr. 2008.

[80] C. Phongcharoenpanich, and R. Suwalak, "Dual-band RFID-reader antenna using annular plate with curved and rectangular slots," *International Conference on Electromagnetics in Advanced Applications (ICEAA)*, 2010, pp. 633-636, 2010.

[81] F.Y. Kuo, P.H. Pan, C.-Y. Chiang, H.T. Hsu, and H.T. Chou, "Dual-band aperture-coupled patch antenna for RFID mobile terminal applications," *Asia-Pacific Microwave Conference Proceedings (APMC)*, pp. 2201-2204, Dec. 2010.

[82] M.I. Sabran, S.K.A Rahim, A.Y.A. Rahman, T.A Rahman, M. Nor, and Evizal, "A Dual-Band Diamond-Shaped Antenna for RFID Application," *IEEE Antennas and Wireless Propagation Letters*, vol.10, pp. 979-982, 2011.

[83] C. Jaehoon, K. Uisheon, U. Youngman, and S. Dongmin, "Design of Antennas for the UHF RFID System," *International Workshop on Antenna Technology: Small Antennas and Novel Metamaterials (iWAT)*, pp. 75-78, 2008.

[84] H.T. Hsu, and T.J. Huang, "Aperture-coupled dual-band circularly polarized antenna for RFID reader applications," *Cross Strait Quad-Regional Radio Science and Wireless Technology Conference (CSQRWC)*, pp. 52-55, 2012.

[85] J. Ghalibafan, F.H Kashani, "A circularly polarized fractal microstrip antenna for RFID applications," *IEEE International Symposium on Radio-Frequency Integration Technology,* pp. 319-322, 2009.

[86] A.T Mobashsher, N. Misran, and M.T Islam, "Design analysis of compact dual-band microstrip RFID reader antenna," *International Conference on Space Science and Communication,* pp. 83-88, 2009.

[87] A. Azarbar, M. Mashhadi, and J. Ghalibafan, "A novel circularly polarized dual-band slot antenna for RFID applications," *IEEE GCC Conference and Exhibition (GCC)*, pp. 202-204, 2011.

[88] X.L. Quan; R.L. Li, Y.H. Cui, and M.M. Tentzeris, "Analysis and Design of a Compact Dual-Band Directional Antenna," *IEEE Antennas and Wireless Propagation Letters*, vol.11, pp. 547-550, 2012.

[89] A.T. Mobashsher, M.T. Islam, and N. Misran, "A Novel High-Gain Dual-Band Antenna for RFID Reader Applications," *IEEE Antennas and Wireless Propagation Letters,* vol.9, pp. 653-656, 2010.

[90] J. Huang, "A Technique for an Array to Generate Circular Polarization with Linearly Polarized Elements," *IEEE Transactions on Antennas and Propagation*, vol. 34, pp. 1113-1124, Sep. 1986.

[91] R. Caso, A. Buffi, M.R. Pino, P. Nepa, and G. Manara, "A novel dual-feed slot-coupling feeding technique for circularly polarized patch arrays," *IEEE Antenna and Wireless Propagation Letters*, vol.9, pp. 183-186, 2010.

[92] Nasimuddin, X. Qing, and Z.N. Chen, "Compact circularly polarized symmetric-slit microstrip antennas", *IEEE Antennas and Propagation Magazine*, 53, (4), pp. 63-75, 2011.